

Index 35726 X
ISSN 0867-888X

POLISH
ACADEMY
OF SCIENCES
INSTITUTE
OF FUNDAMENTAL
TECHNOLOGICAL
RESEARCH

NATIONAL
ENGINEERING
SCHOOL
OF METZ

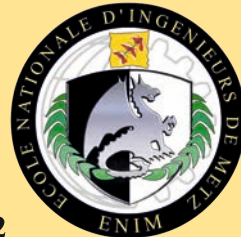
ENGINEERING TRANSACTIONS

ROZPRAWY INŻYNIERSKIE - TRAITE d'INGENIERIE



QUARTERLY
VOLUME 60
ISSUE 4

WARSZAWA - METZ 2012



Faster online
<http://et.ippt.pan.pl>

Contents of issue 4 vol. LX

- 287 P. G. KOSSAKOWSKI, W. TRAMPCZYŃSKI, *Microvoids evolution in S235JR steel subjected to multi-axial stress state*
- 315 C. HABERSOHN, F. BLEICHER, *Controller concept for a highly parallel machine tool*
- 333 J. JANISZEWSKI, *Selection of shaped charge liner material with the use of electromagnetic expanding ring technique*
- 345 M. RODRÍGUEZ-MILLÁN, Á. VAZ-ROMERO, J.A. RODRÍGUEZ-MARTINEZ, A. RUSINEK, Á. ARIAS, *Influence of failure strain of different aluminium alloys on dynamic problems*
- 355 A. S. BANYAL, *A characterization of the Rivlin-Ericksen viscoelastic fluid in the presence of a magnetic field and rotation*
- 371 FROM THE EDITORIAL BOARD, *Our Reviewers*

ENGINEERING TRANSACTIONS **Founded 1952** **Appears since 1953**

Copyright ©2012 by Institute of Fundamental Technological Research
Polish Academy of Sciences, Warsaw, Poland

Aims and Scope

ENGINEERING TRANSACTIONS promotes research and practise in engineering science and provides a forum for interdisciplinary publications combining mechanics with material science, electronics (mechanotronics), medical science and biotechnologies (biomechanics), environmental science, photonics, information technologies and other engineering applications. The Journal publishes original papers covering a broad area of research activities including experimental and hybrid techniques as well as analytical and numerical approaches. Engineering Transactions is a quarterly issued journal for researchers in academic and industrial communities.

INTERNATIONAL COMMITTEE

S. A. ASTAPCIK (<i>Byelorussia</i>)	P. PERZYNA (<i>Poland</i>)
A. CARPINTERI (<i>Italy</i>)	L. TOTH (<i>France</i>)
G. DOBMANN (<i>Germany</i>)	Z. WESOŁOWSKI (<i>Poland</i>)
T. IWAMOTO (<i>Japan</i>)	P. WOOD (<i>U.K.</i>)
A. N. KOUNADIS (<i>Greece</i>)	G. VOYIADJIS (<i>USA</i>)
J. LIN (<i>U.K.</i>)	R. ZAERA (<i>Spain</i>)
T. ŁODYGOWSKI (<i>Poland</i>)	

EDITORIAL COMMITTEE

R. PEÇERSKI – Editor	A. RUSINEK – Co Editor
Z. AZARI	K. KOWALCZYK-GAJEWSKA
P. CHEVRIER	Z. KOWALEWSKI
B. GAMBIN	P. LIPIŃSKI
J. HOLNICKI-SZULC	K. KRIEGEL – assistant of the Co Editor
	ENIM, 1 route d’Ars Laquenexy
	57078 Metz Cedex 03
	Phone: +33 3 87344266, E-mail: relinter@enim.fr

J. ŻYCHOWICZ-POKULNIEWICZ – secretary

Address of the Editorial Office:

Engineering Transactions
Institute of Fundamental Technological Research
Pawińskiego 5B, PL 02-106 Warsaw, Poland

Phone: (48-22) 826 12 81 ext. 206, Fax: (48-22) 826 98 15, E-mail: engtrans@ippt.pan.pl

Abstracted/indexed in:

Applied Mechanics Reviews, Current Mathematical Publications, Elsevier, EMBASE, Engineering Village, Inspec, Mathematical Reviews, MathSci, Reaxys, Scopus, Zentralblatt für Mathematik.

<http://et.ippt.pan.pl/>

Address of the Editorial Office:

Engineering Transactions
Institute of Fundamental Technological Research
Pawińskiego 5B
PL 02-106 Warsaw, Poland
Phone: (48-22) 826 12 81 ext. 206, Fax: (48-22) 826 98 15
E-mail: engtrans@ippt.pan.pl

SUBSCRIPTIONS

**Subscription orders for all journals edited by Institute of Fundamental Technological Research (IPPT) may be sent directly to the Publisher: Institute of Fundamental Technological Research
e-mail: subscribe@ippt.pan.pl**

Please transfer the subscription fee to our bank account:
Payee: IPPT PAN
Bank: Pekao S.A. IV O/Warszawa
Account number 05124010531111000004426875.

WARUNKI PRENUMERATY

Prenumeratę na wszystkie czasopisma wydawane przez Instytut Podstawowych Problemów Techniki PAN przyjmuje Dział Wydawnictw IPPT.

Bieżące numery Engineering Transactions można nabyć bezpośrednio w Redakcji:

**ul. Pawińskiego 5B, 02-106 Warszawa
Tel.: (48-22) 826 60 22; Fax: (48-22) 826 98 15
e-mail: subscribe@ippt.pan.pl**

Microvoids Evolution in S235JR Steel Subjected to Multi-Axial Stress State

Paweł Grzegorz KOSSAKOWSKI, Wiesław TRAMPCZYŃSKI

Kielce University of Technology
Faculty of Civil Engineering and Architecture
Chair of Strength of Materials and Concrete Structures
al. Tysiąclecia Państwa Polskiego 7, 25-314 Kielce, Poland
e-mail: {kossak, wtramp}@tu.kielce.pl

The article presents the results of the experimental and numerical analysis of microvoids evolution in elements made of S235JR steel under multi-axial stress state. The numerical simulations were based on the modified Gurson-Tvergaard-Needleman (GTN) material model, taking into account the impact of microstructural defects on the material strength. Two approaches were used, assuming a global and local damage of the structure of S235JR steel. In both cases, the evolution of microdamage (voids) and their impact on the strength and failure of the material were analysed. The results of numerical simulations were similar to the results obtained during microstructural examinations.

Key words: Gurson, Gurson-Tvergaard-Needleman (GTN) material model, multi-axial stress states, S235JR steel, microvoids, numerical simulations.

1. INTRODUCTION

The catastrophic failures of engineering structures occurring recently in Poland have led to more extensive research into pre-failure conditions and estimation of limit loads beyond the elastic range. The damage initiation is strongly connected with the different processes, such as overload and corrosion taking place during the operation of the structure. These phenomena reduce the suitability of the structural elements for use, which in an extreme situation may lead to a total destruction of whole structure. In Fig. 1 the corrosion hole is shown as an example of the material structure discontinuity, which strongly reduces the load-bearing capacity of the bridge structural element. Such discontinuity and the thinning of the element's web observed around the corrosion hole changes locally the prevailing strain and stress state, leading to the reduction of the material strength.



FIG. 1. Corrosion hole in bridge structural element.

In the situation analysed, the material is subjected to different (spatial, multi-axial) stress state in comparison to the design assumptions. The transition of the material above the yield strength in a non-linear range may be the most dangerous consequence of discussed damages. It leads to the increase of the stress components which were negligible in the uniaxial stress state. Finally, it may induce the destruction of the individual structural element and ultimately the collapse of the entire structure. Thus, the analysis of multi-axial stress states which may take place during the pre-failure states is especially important issue from a practical point of view and should be subjected to the detailed strength analyses.

For elements under the action of uniaxial stress the strength analysis is relatively easy to conduct. When the failure stress is a three-stress function, the elements are subjected to the multi-axial stress states and the analysis becomes more complicated. In such case, the safety of a steel structure can be assessed using the so called HUBER-MISES-HENCKY (HMH) strength hypotheses, but by assuming the continuum of the material, the HMH model is not suitable to analyse the plastic state of material.

The multi-axial stress state is often realized during experiments with using a tensile bar of circular cross-section with the circumferential annular notch (Fig. 2).

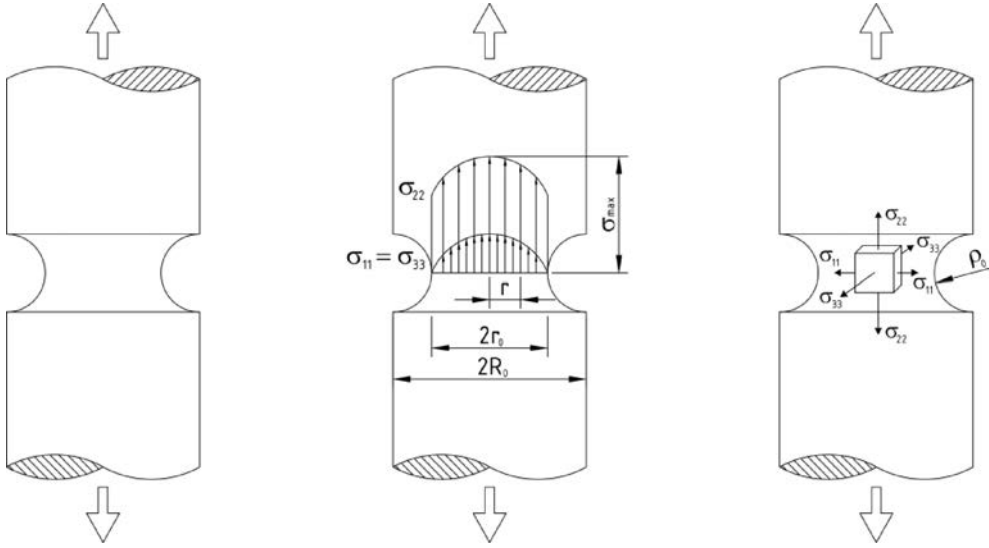


FIG. 2. Geometry and stress state components of a tensile bar of circular cross-section with the circumferential annular notch.

A notch simulates the so-called neck which is observed in the smooth specimens as a result of plasticity in the range of large local deformations. The initial state of stress may be determined by choosing a suitable geometry, in particular, the depth of a notch. Multi-axial state of stress is defined by the so-called stress triaxiality σ_m/σ_e , where σ_m and σ_e denotes the mean normal stress and the effective stress, respectively. For a smooth specimen stress triaxiality reaches limit, minimal value, i.e. $\sigma_m/\sigma_e = 1/3$. For a tensile bar of circular cross-section with a circumferential annular notch the initial stress triaxiality σ_m/σ_e often is determined by using the BRIDGMAN'S solution [1]. For the middle plane of the notch stress triaxiality σ_m/σ_e is defined as

$$(1.1) \quad \frac{\sigma_m}{\sigma_e} = \frac{1}{3} + \ln\left(\frac{r_0}{2\rho_0} + 1\right),$$

where $\sigma_m = (\sigma_{11} + \sigma_{22} + \sigma_{33})/3$ – mean normal stress, σ_e – effective stress, r_0 – initial minimal radius, ρ_0 – initial notch radius.

As can be seen in formula (1.1), when the failure stress is a three-stress function the strength analysis is complicated, especially for damaged elements which are plastically deformed. As mentioned above in such situation, the classical strength hypotheses such as HUBER-MISES-HENCKY (HMH) hypothesis cannot be used due to assuming the continuum of the material structure. The damage material models taking into account the impact of the microdefects of the material structure on the material strength should be applied.

The structural damage of metallic materials, i.e. the process of crack initiation and propagation of polycrystalline structure is closely related to the microstructure of the material. Several basic types of fracture mechanisms such as plastic, cleavage and brittle intergranular, shear or void-sheeting and ductile may be observed [2]. For ductile and shear fracture, the cracking is connected with the nucleation, growth and coalescence of microstructure defects, in the form of voids. Voids are formed on both the material matrix and the existing non-metallic inclusions and second-phase particles. The damage occurs through the growth and coalescence of voids resulting in the development of localised plastic deformations (Fig. 3).

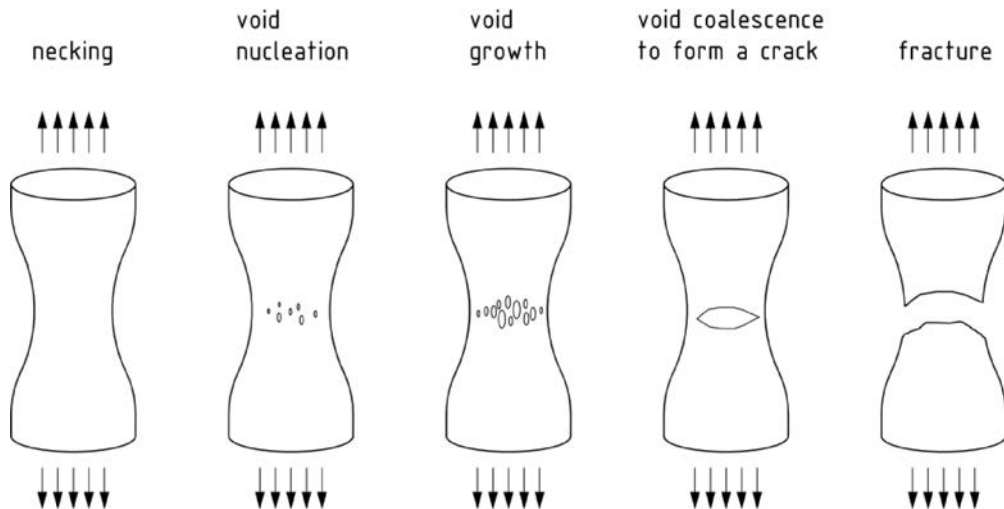


FIG. 3. Ductile fracture micro-mechanism and void evolution in multi-axial stress states.

The evolution of the micro-defects (voids) is one of the significant steps during ductile fracture process. It is a complex phenomenon, depending on many processes such as anisotropy of the voids distribution, spacing, and shape, void nucleation, changes and evolution in void shapes, void-to-void interactions and the nucleation and growth of secondary voids. Voids evolutions determines the localisation of the micro-crack initiation, leading to the process zone forming and finally to the material failure. In many cases, the local damage of the structural elements occurs due to the micro-defects evolution and growth, which in the extreme situation may lead to the total collapse of the structure.

Phenomena described above and connected to ductile fracture of metals can be analysed using damage models taking into account the influence of the microstructural defects on the material strength by defining the relationship between the particular failure stages and the strength of the material, which is shown schematically in Fig. 4.

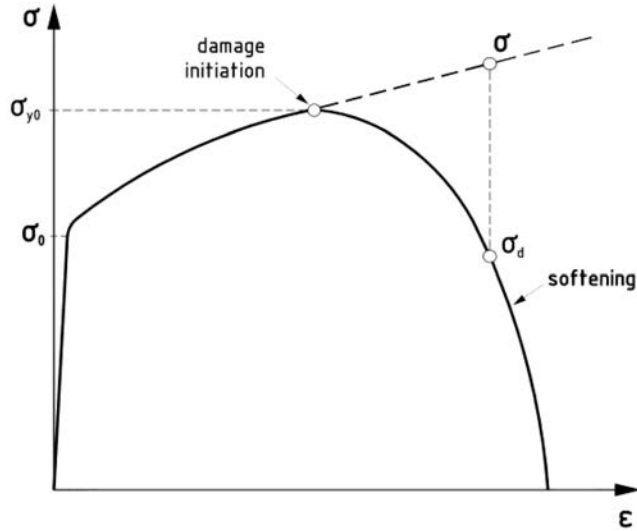


FIG. 4. Reduction of material strength according to general damage material model.

When damage is initiated, the decrease of the material strength is observed, resulting in the decrease of the stress σ_d , determined taking into consideration the damage impact. For the fully dense material, without structural damages, the stress σ increases in whole range of deformation. The decrease of the material strength and stress σ_d is called as softening phenomenon.

One of the first damage material models was GURSON model [3] for porous solids. It was the modification of HMH criterion, defining the influence of an increase in the void volume fraction on the strength of the material, according to the following formula

$$(1.2) \quad \Phi = \left(\frac{\sigma_e}{\sigma_0}\right)^2 + 2f \cosh\left(\frac{3\sigma_m}{2\sigma_0}\right) - 1 - f^2 = 0,$$

where Φ – non-dilatational strain energy, σ_e – effective stress according to the HMH hypothesis, σ_0 – yield stress of the material, σ_m – hydrostatic pressure (mean stress), f – void volume fraction.

The original GURSON failure criterion was further modified by TVEERGAARD [4] and then by TVERGAARD and NEEDLEMAN [5], as a method referred GTN for the estimation of failure loads resulting from ductile fracture taking into account the microstructural parameters and plastic properties of a material, which is presented in further part of this study.

The GTN method is widely used in various engineering issues. According to the current standards, for instance [6] and its commentary by SEDLACEK *et al.* [7], the GTN model is a basic damage model recommended to use in the analysis of emergency condition for building structures.

Analysing the current state of knowledge on the use of GTN model in the numerical simulation of ductile fracture of steel it can be concluded that there is no comprehensive approach, which allows to carry out numerical calculations for any elements. The numerical simulations are performed using the method of best fit the GTN material parameters for elements with predetermined geometries and strength properties. The GTN parameters are frequently determined basing on the curve fitting technique, without taking into account the typical or boundary parameters values specified in literature. Consequently, the lack of standardised microstructural parameters to develop a GTN model for steels used most commonly in civil engineering is a basic drawback.

Another problem encountered during numerical simulations of nonlinear ranges is proper way of modelling and perform engineering calculations. During simulations of ductile fracture using the finite element method and the GTN model, size effects are encountered, revealing the softening of the final part of the strength curve. Several methods have been tested to minimize the softening effect (e.g. [8–10]), but their applications is limited due to the lack of procedures in the available engineering software.

Taking into consideration the importance of practical issues related to the safety assessment of steel structures and components and described above problems, it is necessary to elaborate a computational procedure which allows the numerical estimation of the limit load capacity of the elements operating in the nonlinear ranges and simulation of the material failure.

Therefore, a wide research program was focused on elaboration of procedures allowing for the numerical analysis of load-bearing capacity of steel building construction elements operating in pre-failure states, taking into account the impact of microdamage using the modified GTN material model. S235JR steel was tested, which is the main steel grade used in construction, so the results will be helpful in analysis and expert opinions on the load-bearing capacity of steel components and structures.

Taking into account that micro-evolution is a fundamental process influencing the state of stress and strain, and directly affects the strength of the material, in the first stage, the research was focused on this issue [11–13] and to develop a methodology of numerical calculations [14]. The next stage of the study includes the determination of GTN model parameters and their sensitivity analysis for S235JR steel.

In contrast to the approach based on matching the material constants for the elements of a particular geometry and strength properties on the basis of curve fitting technique, it is proposed to determine GTN parameters based on actual microstructure and strength parameters determined experimentally. The researches already done were related to the experimental determination of the initial porosity of S235JR steel [11–14].

This article presents the results of experimental and numerical analysis of the evolution of the microstructure damage of S235JR steel. The studies concerned the elements under a multi-axial stress state described by the so-called stress triaxiality σ_m/σ_e , defined as the ratio of mean stress σ_m to effective normal stress σ_e . Taking into account that observed during the studies the effects were most intense for elements with a stress triaxiality above unity [11–13], detailed analysis were performed for elements with the highest value of stress triaxiality, i.e. $\sigma_m/\sigma_e = 1.345$.

In the studies the GTN model parameters such as initial void volume fraction f_0 and TVERGAARD'S parameters q_i were determined experimentally, basing on the actual properties of the microstructure and strength of S235JR steel, as well as the results of studies performed before [11–16].

During the numerical simulations two approaches were used, assuming global and local damage to the material structure. In both cases, the evolution of microdamage (voids) and their impact on the strength and the failure of the material were analysed.

2. MODIFIED GURSON-TVERGAARD-NEEDLEMAN (GTN) DAMAGE MATERIAL MODEL

According to the modified GURSON-TVERGAARD-NEEDLEMAN material model [4, 5] the failure criterion is defined as following

$$(2.1) \quad \Phi = \left(\frac{\sigma_e}{\sigma_0}\right)^2 + 2q_1 f^* \cosh\left(q_2 \frac{3\sigma_m}{2\sigma_0}\right) - (1 + q_3 f^{*2}) = 0,$$

where Φ – non-dilatational strain energy, σ_e – effective stress according to the HMH hypothesis, σ_0 – yield stress of the material, σ_m – hydrostatic pressure (mean stress), f^* – modified void volume fraction, q_i – TVERGAARD'S parameters describing the plastic properties of the material.

As can be seen, the modified GTN yield criterion (2.1) is described by many material constants, including microstructural properties such as modified void volume fraction f^* , and strength properties defined by TVERGAARD'S parameters q_i and yield stress σ_0 .

The modified void volume fraction f^* is defined as follows:

$$(2.2) \quad f^* = \begin{cases} f & \text{for } f \leq f_c, \\ f_c + \frac{\bar{f}_F - f_c}{f_F - f_c} (f - f_c) & \text{for } f_c < f < f_F, \\ \bar{f}_F & \text{for } f \geq f_F, \end{cases}$$

where f_c – critical void volume fraction at which the void coalescence starts, f_F – void volume fraction corresponding to the complete loss of the material strength, at final separation of the material, $\bar{f}_F = \left(q_1 + \sqrt{q_1^2 - q_3} \right) / q_3$.

As can be seen, at the beginning, when the material is not subjected to the deformation, modified void volume fraction f^* is equal to the initial void volume fraction f_0 , being a basic GTN material parameter connected to the material porosity.

TVERGAARD'S parameters q_i have influence on strength properties of the material. The modified void volume fraction f^* is changed by first TVERGAARD'S parameter q_1 in the yield domain (2.1). The strength of the material is decreased for higher values of q_1 parameter, revealing the softening phenomenon due to void growth dominating over hardening properties of the matrix material (Fig. 5a). Higher values of q_1 lead to stronger softening. The optimal value of $q_1 = 1.5$ was proposed by TVERGAARD [4] to model numerically the localisation of plastic deformations effect and fracture phenomena for many porous solids, including metals.

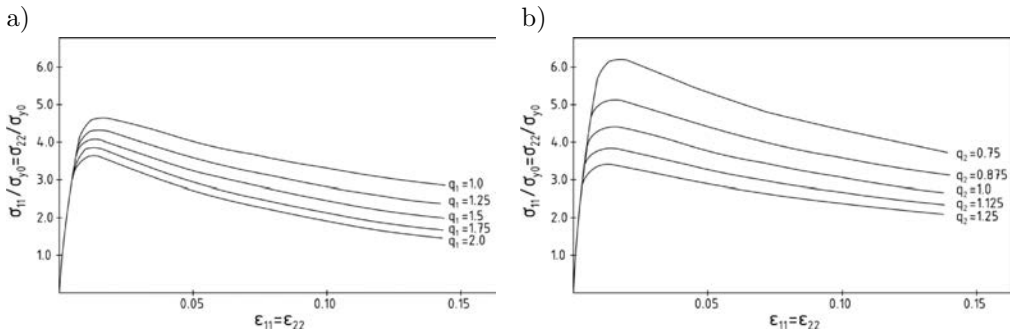


FIG. 5. Influence of TVERGAARD'S parameters q_1 and q_2 on nonlinear response of GTN constitutive law at $\varepsilon_{22}/\varepsilon_{11} = 1.0$ for: a) $1.0 \leq q_1 \leq 2.0$; b) $0.75 \leq q_2 \leq 1.25$ [17].

The second TVERGAARD'S parameter q_2 have impact on the hydro-static component $\sigma_m = \sigma_{kk}/3$, being in relation to the first invariant of the stress state σ_{kk} . The yield limit is strongly reduced for high values of parameter q_2 , leading to the strong softening due to the void growth, revealing the annihilation of the strain hardening properties of the matrix material (Fig. 5b). The optimal value $q_2 = 1.0$ was suggested by TVERGAARD [18].

Summing up, typical and suggested values of TVERGAARD'S parameters q_i were established as $q_1 = 1.5$, $q_2 = 1.0$ and $q_3 = q_1^2 = 2.25$ for many metal materials, including steel, being treated as constant for many years. The results of studies of FALESKOG *et al.* [15] revealed, that TVERGAARD'S parameters are dependent on the elastic-plastic properties of the material, such as strain hardening exponent N and yield stress σ_0 to modulus of elasticity E ratio (Fig. 6).

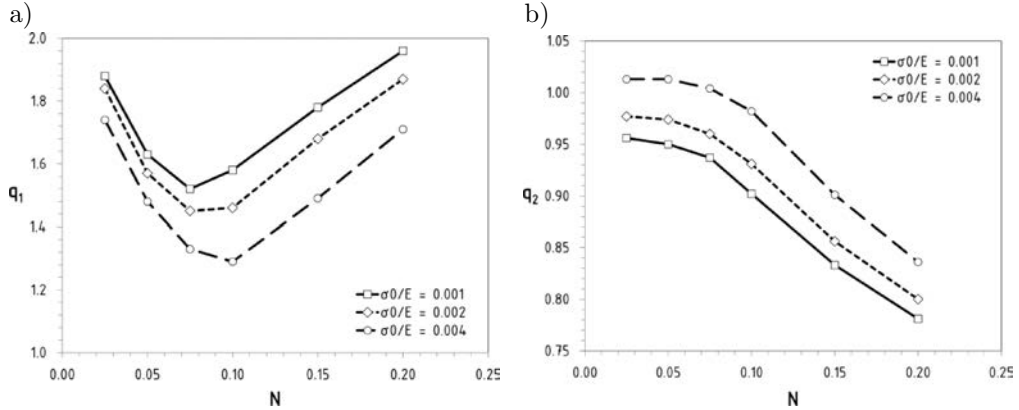


FIG. 6. Correlations q_1 (a) and q_2 (b) to strain hardening N , for different σ_0/E ratios [15].

An increase in the void volume fraction \dot{f} is defined by relationship:

$$(2.3) \quad \dot{f} = \dot{f}_{gr} + \dot{f}_{nucl} = (1 - f)\dot{\epsilon}^{pl} : \mathbf{I} + \frac{f_N}{s_N \sqrt{2\pi}} \exp \left[-\frac{1}{2} \left(\frac{\epsilon_{em}^{pl} - \epsilon_N}{s_N} \right)^2 \right] \cdot \dot{\epsilon}_{em}^{pl},$$

where: \dot{f}_{gr} – change due to growth of voids existing in the material, \dot{f}_{nucl} – change due to nucleation of new voids, f_N – volume fraction of nucleated voids, s_N – standard deviation of nucleation strain, $\dot{\epsilon}^{pl}$ – plastic strain rate tensor, \mathbf{I} – second-order unit tensor, ϵ_N – mean strain of the void nucleation, ϵ_{em}^{pl} – equivalent plastic strain in the matrix material, $\dot{\epsilon}_{em}^{pl}$ – equivalent plastic strain rate in the matrix material.

3. GTN MODEL PARAMETERS OF S235JR STEEL

3.1. Microstructural examinations

The first step of the material examinations was to obtain the images of the microstructure of S235JR steel [19]. The images were taken using the light metallographic microscope with magnification $\times 100 \div 1000$. The sections were cut of the material intended to the strength tests. After the sections were cut out, the specimens were digested and polished.

S235JR steel belongs to a group of low, mild carbon steel having a maximum carbon content of $C = 0.2\%$ and the maximum contents of elements: $Mn = 1.40\%$, $P = 0.035\%$, $S = 0.035\%$ and $N = 0.012\%$.

The observed microstructure was a ferritic-perlitic type (Fig. 7a). In longitudinal section the ferrite grain were equally axial, while pearlite grains were elongated by the material forming (rolling). The contribution of pearlite was es-

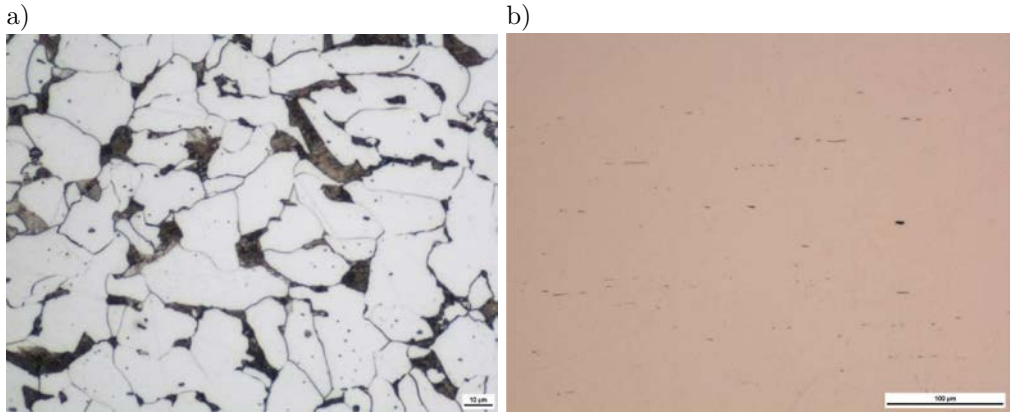


FIG. 7. Microstructure of S235JR steel: a) sample after digestion, b) sample after polishing [19].

estimated to be approximately 10–20%. As can be seen in Fig. 7b, there are a large number of non-metallic inclusions.

Observed non-metallic inclusions are mainly sulfides and brittle oxides. The sulphide inclusions were characterized by an elongated shape and their length reached up to 61.9 μm . These inclusions were irregularly distributed in the volume of material and formed the bands. The second type of non-metallic inclusions were brittle oxide inclusions. They have a shape close to rectangular and sometimes occurred with sulphide inclusions.

In order to fully characterize the tested material in terms of the observed non-metallic inclusions, the basic parameters of the stereological for inclusions were measured. The initial void volume fraction of the inclusions was estimated at a maximum level of 0.17% (for the central part of the cross section).

3.2. Strength tests and numerical simulations

In order to determine the strength parameters of S235JR steel the standard static tensile test was performed for specimens with a circular cross-section, according to [20]. The tests were performed using 322 MTS testing machine with capacity of 100 kN and a hydraulic drive with controlled increase of displacement (Fig. 8b).

The nominal diameter of the specimens was $d = 10$ mm, the length of the measuring base $l_0 = 50$ mm, and the primary cross-sectional area $S_0 = 78.5$ mm² (Fig. 8a). The number of the test was $n = 8$ specimens.

The average values of strength parameters for the significance level of 0.05 were obtained as follows: the yield stress $R_{0.2} = 318.3 \pm 2.59$ MPa with standard deviation $s = 3.73$ MPa, the tensile strength $R_m = 457.4 \pm 4.91$ MPa with

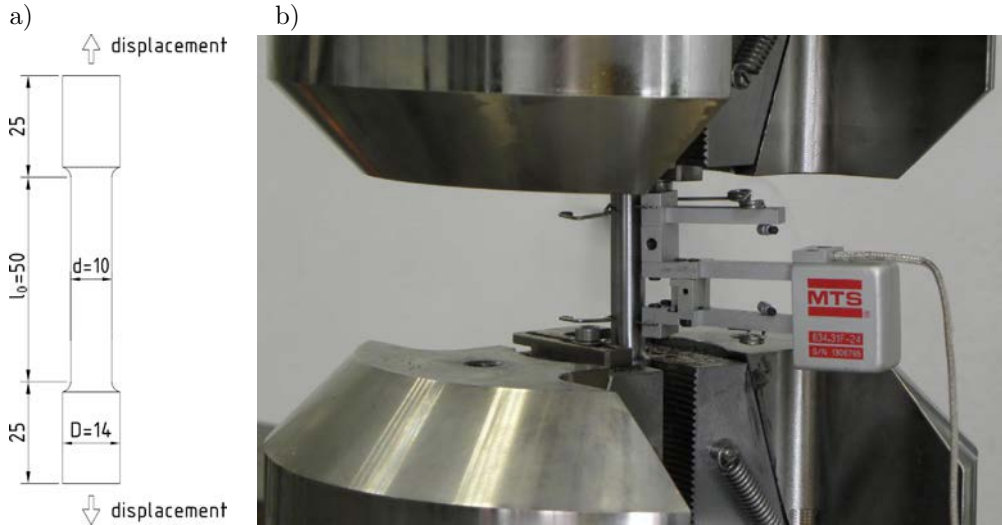


FIG. 8. Sample used in strength tensile tests of S235JR steel (a); sample subjected to tension (b).

standard deviation $s = 7.09$ MPa, and the percentage elongation $A_t = 33.3 \pm 1.47\%$ with standard deviation $s = 2.13\%$. The modulus of elasticity was $E = 205$ GPa and coefficient of transverse elasticity was $G = 80$ GPa. During the test the nominal normal stress σ and the longitudinal strain ε were determined as a function $\sigma(\varepsilon)$.

3.3. Determination of material parameters of GTN model

Material parameters of GTN model for S235JR steel were determined basing on the results of microstructural studies, strength parameters and numerical modeling of the standard tensile test and results obtained in previous studies [11–14].

The initial void volume fraction was determined during the microstructural examinations shown in Subsec. 3.1 as $f_0 = 0.0017 = 0.17\%$ [19].

The TVERGAARD'S parameters were determined according to results obtained by FALESKOG *et al.* [15] and established as $q_1 = 1.90$, $q_2 = 0.81$ and $q_3 = 3.61$ for the ratio $R_{0.2}/E = 0.00155$ with strain-hardening exponent $N = 0.183$.

Other parameters of the model for S235JR steel were assumed to fit final results (Fig. 19) and according to data obtained during tests carried out by the authors [11–14].

Numerical calculations were performed using a program based on finite element method Abaqus Explicit 6.10. The elements were modelled as an axially-symmetric, using standard CAX4R elements [21]. The model parameters were

determined based on the tensile curves $\sigma(\varepsilon)$ determined experimentally and fitted by numerical simulations. At each iteration step, the values of the GTN model parameters were changed within certain limits. The optimization criterion was the convergence of the $\sigma(\varepsilon)$ values obtained numerically and experimentally.

During the numerical simulation elastic-plastic properties of S235JR steel were described by approximating function as following:

$$(3.1) \quad \frac{\sigma}{\sigma_0} = \left(\frac{\sigma}{\sigma_0} + \frac{3G}{\sigma_0} \varepsilon_{em}^{pl} \right)^N,$$

where σ – stress, σ_0 – yield stress of the material, ε_{em}^{pl} – equivalent plastic strain in the matrix material, G – coefficient of transverse elasticity, N – strain-hardening exponent.

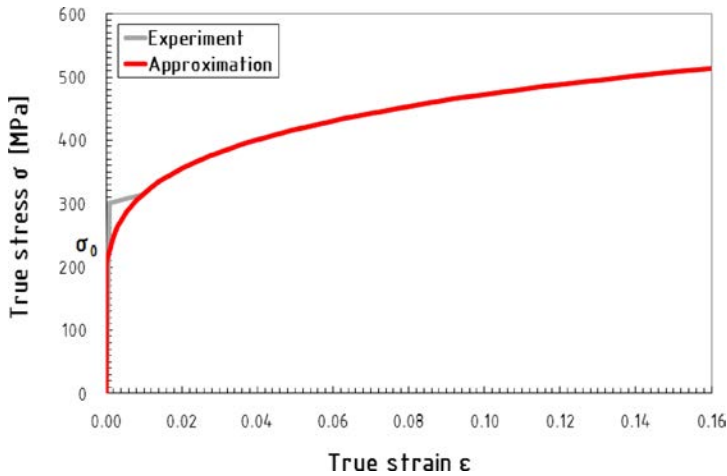


FIG. 9. Approximation of tensile curve $\sigma(\varepsilon)$ according to Eq. (3.1).

At the end:

- the critical value of volume fraction f_c , above which the nominal material strength decreased, was assumed as $f_c = 0.06$ (as suggested by RICHELTSEN and TVERGAARD [22], the critical value of the void volume fraction, f_c , is dependent on the initial void volume fraction f_0). It ranges from $f_c = 0.04$ at $f_0 = 0.0$ to $f_c = 0.12$ at $f_0 = 0.06$,
- the value of the void volume fraction corresponding to the complete loss of material strength f_F was assumed as $f_F = 0.667$ in order to analyse whole range of material deformations, especially at the failure range,
- other GTN material parameters were assumed as following: the volume fraction of the nucleated voids $f_N = 0.04$, the average nucleation (initiation) strain of inclusion-related voids $\varepsilon_N = 0.3$, and the standard deviation of the nucleation strain $s_N = 0.05$.

All parameters of GTN model for S235JR steel are summarized in Table 1, the parameters determined experimentally are marked with bold.

Table 1. Microstructural parameters of GTN model of S235JR steel.

f_0	f_c	f_F	q_1	q_2	q_3	ε_N	f_N	s_N
0.0017	0.06	0.667	1.90	0.81	3.61	0.30	0.04	0.05

4. ANALYSIS OF MICROVOIDS EVOLUTION IN S235JR STEEL

4.1. Strength tests of tensile elements under multi-axial stress state

As part of a wide research program [11–14] the tensile specimens with circular cross-sections for different notch radii ρ_0 (Fig. 10) were tested. It allowed to obtain the multi-axial stress state defined by stress triaxiality ranged from $\sigma_m/\sigma_e = 0.556$ up to $\sigma_m/\sigma_e = 1.345$, according to BRIDGMAN'S solution Eq. (1.1).

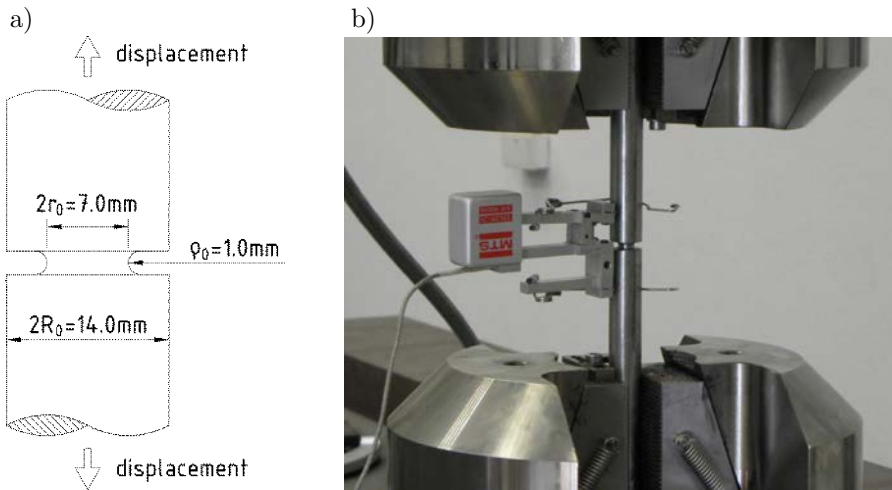


FIG. 10. Geometry (a) and view of ring-notched round specimen subjected to tension in multi-axial stress state (b).

Taking into account that observed during the studies [11–14] the effects were most intense for elements with a high stress triaxiality, for $\sigma_m/\sigma_e > 1$, detailed analysis was performed for elements with the highest value of stress triaxiality, i.e. $\sigma_m/\sigma_e = 1.345$.

The elements with diameters of $2R_0 = 14.0$ mm and $2r_0 = 7.0$ mm and the bottom of the notch radius $\rho_0 = 1.0$ mm were tested, which allowed to obtain a multi-axial state of stress corresponding to the value of stress triaxiality $\sigma_m/\sigma_e = 1.345$. The experimental examinations included tensile strength tests, during

which specimens were subjected to static tension. The quantities measured were force F and displacement of points distributed symmetrically along the specimen l , with the extensometer initial length being $l_{0s} = 32.56$ mm (Fig. 10).

4.2. Microstructural examinations of microvoids evolution

In this part of the research the microstructural images of fracture areas (Fig. 11) and microsections (Fig. 13) of samples subjected to strength tests were made. The sections were cut of the notched tensile specimens subjected to multi-axial stress state according to a scheme shown in Fig. 12. After the sections were cut out, the samples were digested.

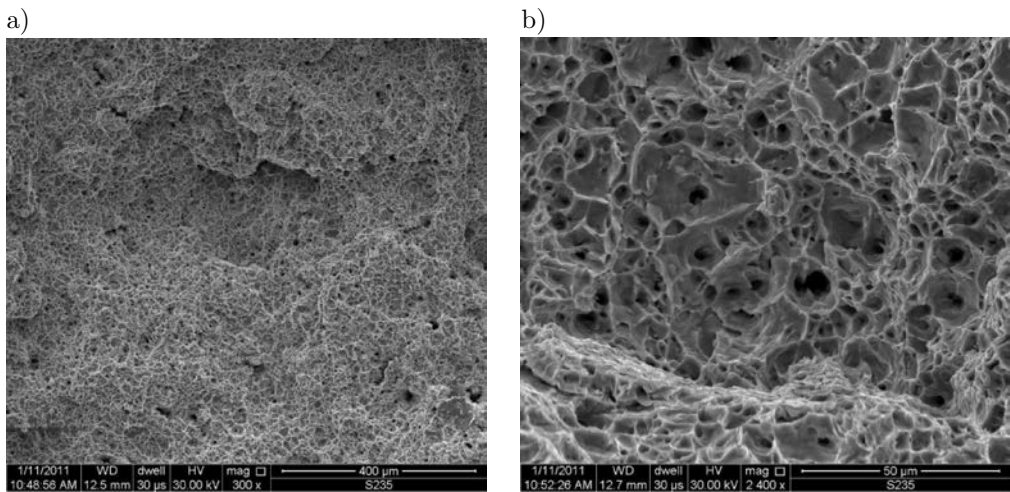


FIG. 11. The microstructure of fracture: a) magnification $\times 300$, b) magnification $\times 2400$.

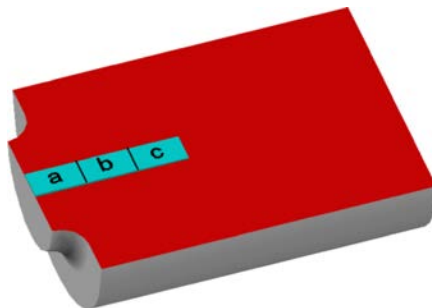


FIG. 12. Denotation of particular microsections (a), (b) and (c).

The scanning photography technique was applied, with using the scanning microscope JEOL JSM-5400 with maximum magnification of 200 000.

The numerous voids around the non-metallic inclusions (Fig. 11) were observed in the fracture area. The voids were formed by the separation of foreign

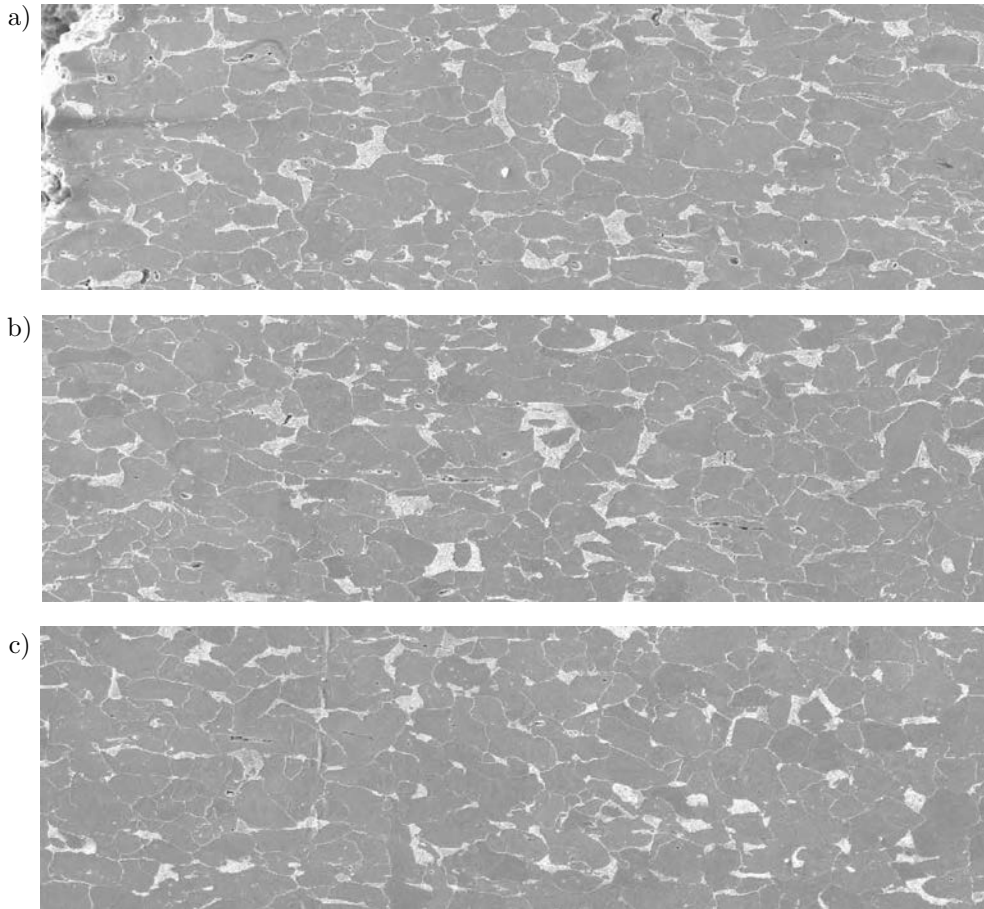


FIG. 13. The images of particular microsections (a), (b) and (c) according to Fig. 12.

phase particles (inclusions) from the matrix. The consequence of the process was the nucleation of voids at the inclusions and the growth and interconnection of the voids during further deformation. The intensity of the process of void nucleation and growth decreased as the distance from the fracture area increased. This was mainly due to changes in the stress state and a smaller deformation of the specimen.

In the region below the fracture area around the notch (Fig. 13c) some non-metallic inclusions were noticed also. They were underwent a slight deformation in comparison to the region of fracture area, consequently the process of void nucleation and growth did not occur in this region.

The phenomenon of void nucleation and growth was observed only in the area of strong plastic deformation, i.e. in the fracture area, which was confirmed by a numerical analysis discussed further in the paper.

4.3. Numerical simulation of microvoids evolution

In the next stage of the analysis the numerical calculations were carried out, in order to simulate the evolution of microvoids during the plasticity process of S235JR steel until the complete failure of the material.

The numerical calculations were performed using Abaqus version 6.10. The samples of circular cross section with a ring notch of radius $\rho_0 = 1.0$ mm used during the strength tests described previously, were modelled. The specimens were subjected to static tension at a controlled rate of displacement 4 mm/min, similarly as in the experiments. Samples were modelled as an axially symmetric, using the standard elements of the 4-nodal CAX4R [21]. Due to the symmetry of the problem, only quarter of the samples were modelled. The height of numerical models corresponded to half the length of the extensometer, i.e. 16.28 mm.

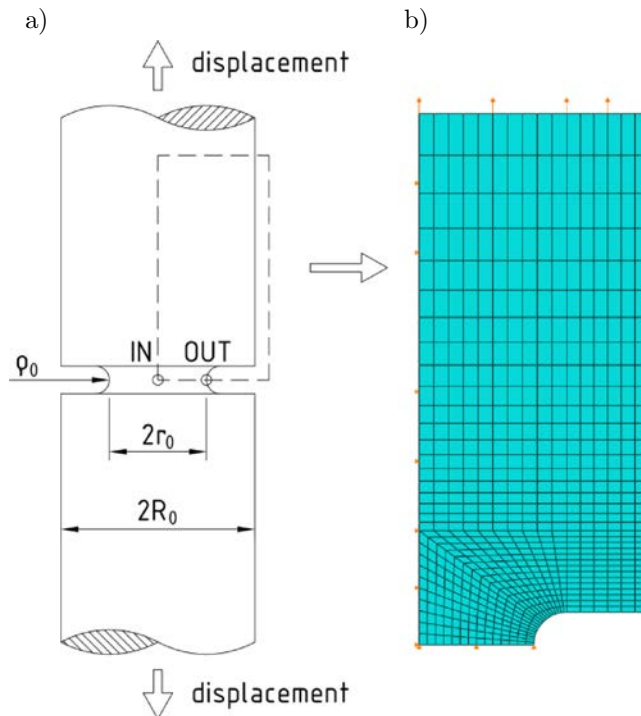


FIG. 14. Tested element (a); numerical model (b).

The modified Gurson-Tvergaard-Needleman (GTN) material model was used with a nonlinear dynamic analysis explicite.

During numerical simulations two approaches were applied:

- *GTN model*, a global approach,
- *Cell model*, a local approach.

4.3.1. *GTN Numerical Model.* The global approach was used assuming a model of a porous GTN material model for whole numerical model, as shown in Fig. 15. The GTN material parameters were assumed according to the values given in Subsec. 3.2 (Table 1). The results obtained using this approach are marked on charts as *GTN model*.

The mesh in the region close to the fracture plane, so-called *process zone*, was modelled with using finite elements of width equal to $250\ \mu\text{m}$, while the height of the finite elements was different, ranging from $50\ \mu\text{m}$ up to $350\ \mu\text{m}$, as it is shown in Fig. 15.

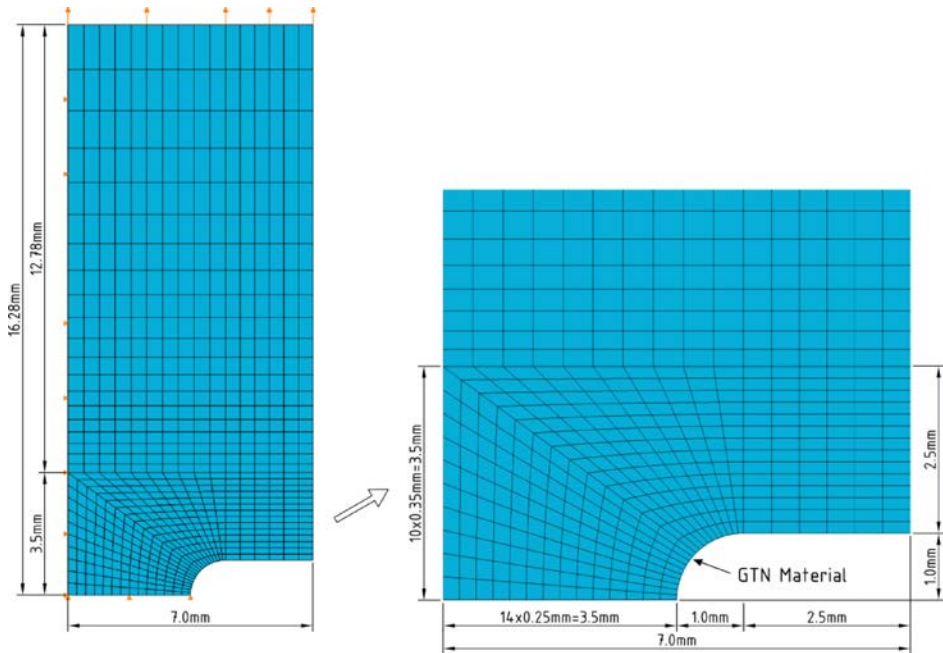


FIG. 15. *GTN* numerical model.

4.3.2. *Cell Numerical Model.* The second approach was based on observations of the formation and evolution of the microstructure of S235JR steel and the results of the analysis contained in [11–16, 23, 24]. As mentioned before, the failure of many metals is due to increased microdamage. This mechanism reveals the macroscopic, local, the so-called *process zone* of a thickness corresponding to one-, two distances between microdamages and it is characterised by considerable plastic deformations. Outside of this area, voids does not show significant growth, which reveals their minimal impact on the softening of the material and decrease its strength.

Numerical implementation of the above phenomena in numerical computation is based on the separation of the area directly adjacent to the crack plane

and using the material model takes into account the microdamage there, such as GTN model. For the rest of numerical model the elastic-plastic material with no damage of the microstructure is used (Fig. 16). The model of porous material is assumed locally to the area in which a significant increase of microvoids and the initiation of cracking is expected.

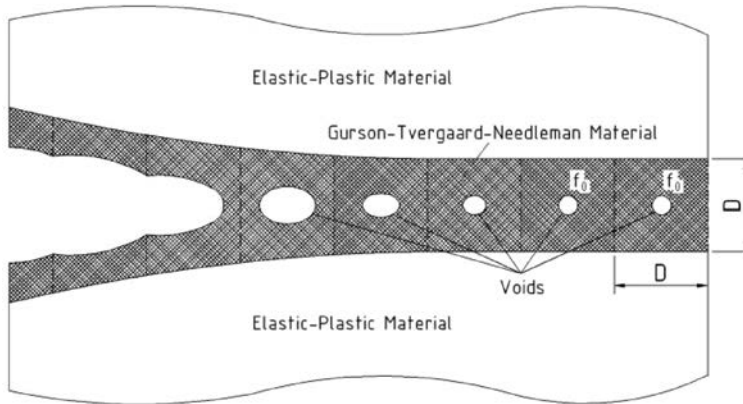


FIG. 16. Implementation of *Cell* method in numerical calculations (basing on Ref. [15]).

The basic issue is the assuming of an appropriate size of the *process zone*, so that the softening of the material to represent the physical processes occurring. Taking into account the results of analysis carried out for tensile elements [14], the thickness of the *process zone* was assumed based on the method proposed by HANCOCK and MACKENZIE [25]. The size of *process zone* defines the characteristic length l_c in the field of high stress and deformations. According to the assumptions of this method, the failure of the material occurs as a result of linking one or two cavities formed from colonies formed by the coalescence of micro-inclusions initiated on second-phase particles. Length l_c is identified with the size of the cavities and micro-colony and it is determined by analysis of the microstructure fractures.

Basing on the results of studies performed before [14] the size of the *process zone* was defined as the average dimensions of an inclusion colony, i.e. characteristic length l_c , and determined during the microstructural examinations. The size of inclusion colony was identified as the average dimensions of the measured plateaus and valleys on the castellated fracture surface. During the measurements the CHAUVENET's criterion was applied and all a typical values were rejected. Twenty measurements were made. The size of *process zone* ranged from 140 to 370 μm , and the average value was determined as $D \approx 250 \mu\text{m}$ (Fig. 17).

The porous GTN material was assumed in numerical model for the layer adjacent to the plane of fracture (Fig. 18). Considering the symmetry of the problem, the thickness of the layer modelling *process zone* was assumed as 125 μm .

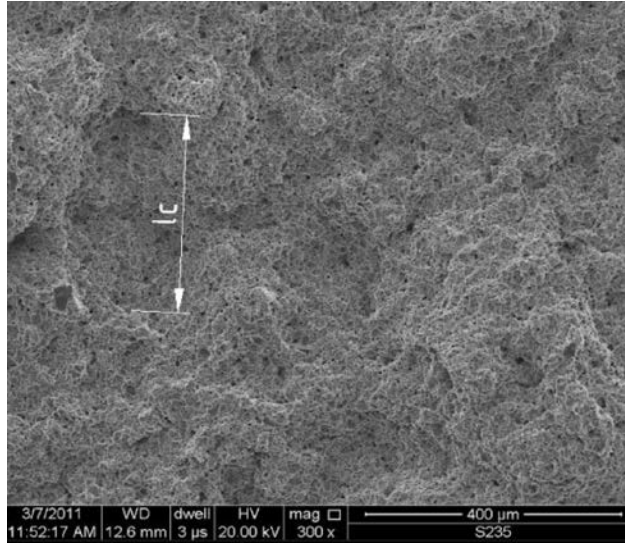


FIG. 17. Determination of dimensions of process zone identified as characteristic length l_c .

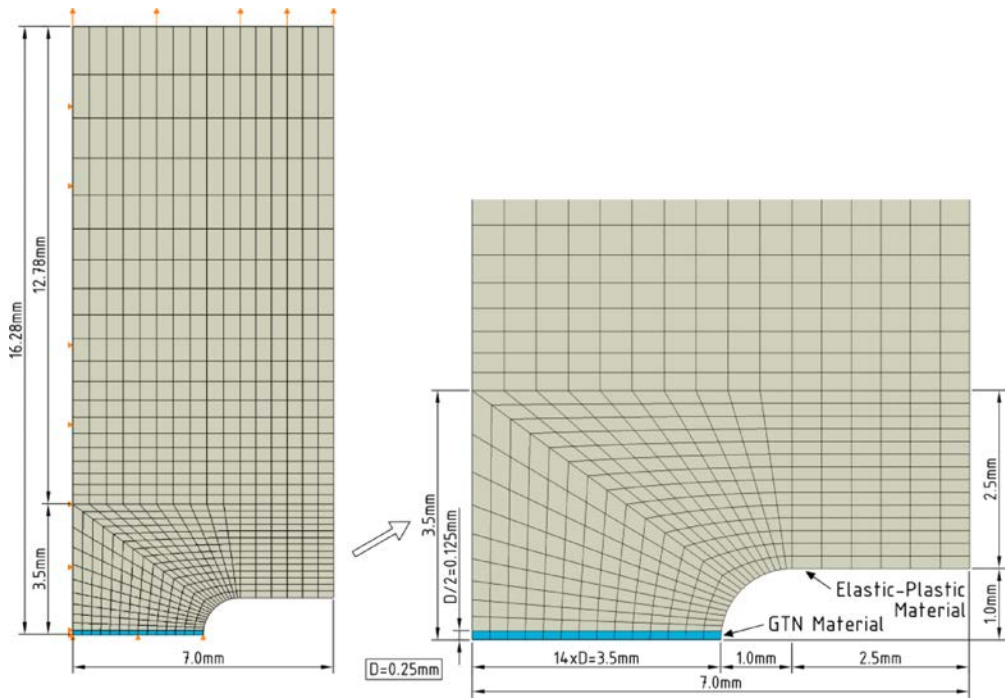


FIG. 18. Cell numerical model.

For the rest of the numerical model the elastic-plastic material was assumed basing on the approximating function (3.1). The results obtained using this approach are referred as *Cell model*.

4.3.3. *Result of numerical analysis.* Numerical simulation of microvoids evolution was based on an analysis of changes in the Void Volume Fraction (VVF) following in the plasticity process of S235JR steel. Based on the results of experimental studies and numerical simulations using *GTN* and *Cell models*, force-elongation curves $F(l)$ for the corresponding points based on extensometer were obtained. The Void Volume Fraction VVF curves as a function of elongation l for the center of elements at the point marked as IN and the bottom of the notch at the point labelled OUT (according to Fig. 14) were obtained.

As is clear from the force-elongation curves $F(l)$ for all analyzed elements the force F determined in numerical simulations are consistent with the results of experimental studies. For both used models, *GTN* and *Cell*, for the range from maximal force F up to the material failure the compatibility of the results obtained numerically and experimentally was noticed (Fig. 19).

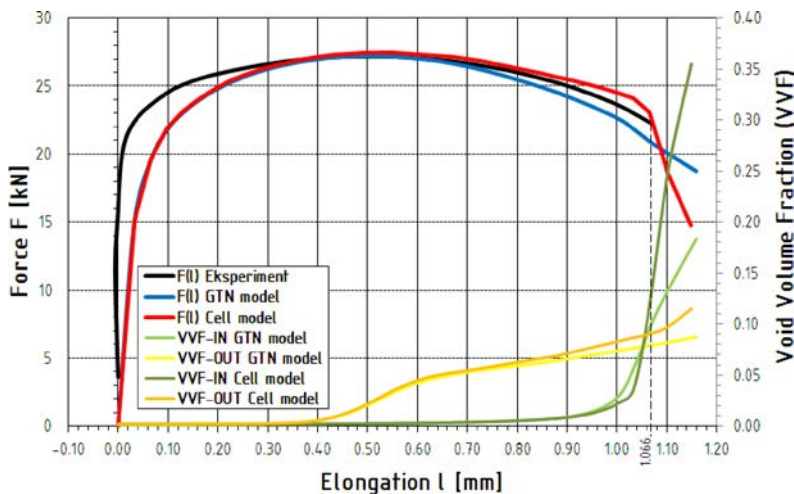


FIG. 19. Force F and Void Volume Fraction VVF versus elongation l curves for points IN and OUT.

Differences in the values of $F(l)$ reveals the end of their parts, when the maximum force is exceeded.

When using the *GTN model*, a slight *softening* phenomenon was observed, progressing in ever greater extent up to the failure. In the final phase of deformation, the noticeable changes in the slope of the curve $F(l)$ is noticed, but no sudden decrease of force is observed at the failure moment, which corresponds to the elongation reached a value of $l = 1.066$ mm. When *Cell model* was used, the opposite effect was observed, i.e. higher values of force F compared to the value determined during the experiments. At the moment of failure the curve $F(l)$ determined numerically falls rapidly, until the total loss of the load-bearing capacity of the element.

Analysing the process of microvoids evolution it should first be noted that in all the analysed elements in the initial stages of deformation, there was no nucleation and growth of voids (Fig. 19). The beginning of the process of nucleation and growth of the void volume fraction was observed just before the maximum force was achieved. The initial process of growth of voids was particularly intense in the outer parts, for the point labelled OUT. After the maximum force was achieved, the rate of growth of voids increases, which corresponds to the elongation $l \approx 0.90$ mm. At the moment just before the failure, for $l = 1.05$ mm, the beginning of the rapid growth of voids in the middle of the sample (in point IN) compared with the external part (in point OUT) was observed. In the further process of deformation the voids increased much more intensively and faster in the middle part of elements in relation to the outside part (Fig. 21–23, and 26–28). It can be concluded that in all analysed cases, the failure proceeded from inside to outside elements.

For both, the *GTN* and *Cell model*, the mechanism of nucleation and microvoids evolutions is similar (Fig. 20, 25). In the outer parts of the elements, the void nucleation occurs at the level of elongation $l \approx 0.40$ mm, and quickly stabilizes at $l \approx 0.65$ mm. A further evolution of voids is due to their growth. In the case of the inner part of the elements the process described above is similar, but occurs much later, for elongations $l \approx 0.95$ mm and $l \approx 1.05$ mm respectively. Similarly to the differences in the final force-elongation curves obtained using the *GTN* and *Cell models*, the differences in curves of Void Volume Fraction *VVF* were observed in the final phase of simulation, for $l > 1.05$ mm, for the phase corresponding to the material failure. The higher growth rate of *VVF*

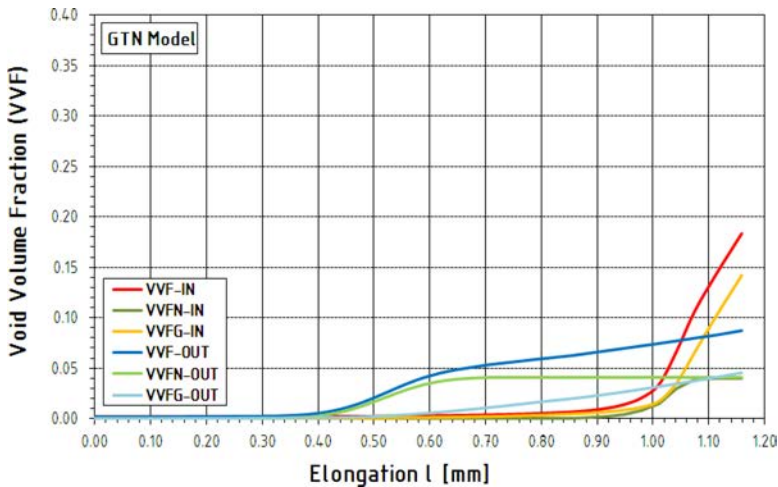


FIG. 20. Void Volume Fraction *VVF*, Void Volume Fraction due to Void Nucleation *VVFN* and Void Volume Fraction due to Void Growth *VVFG* versus elongation l curves for points IN and OUT, *GTN model*.

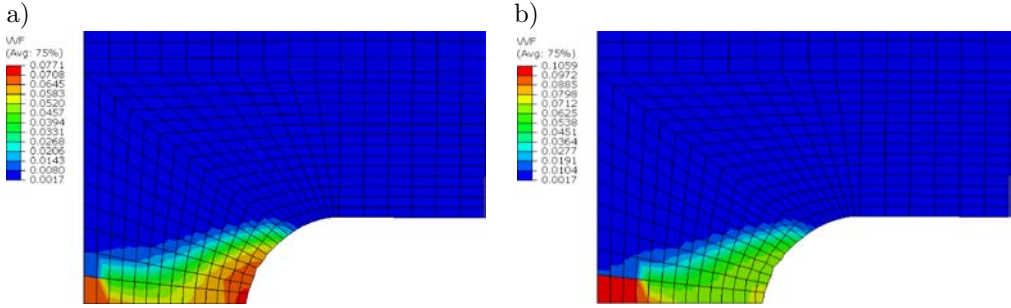


FIG. 21. Void Volume Fraction VVF maps, GTN model: a) $l = 1.04$ mm, b) $l = 1.07$ mm.

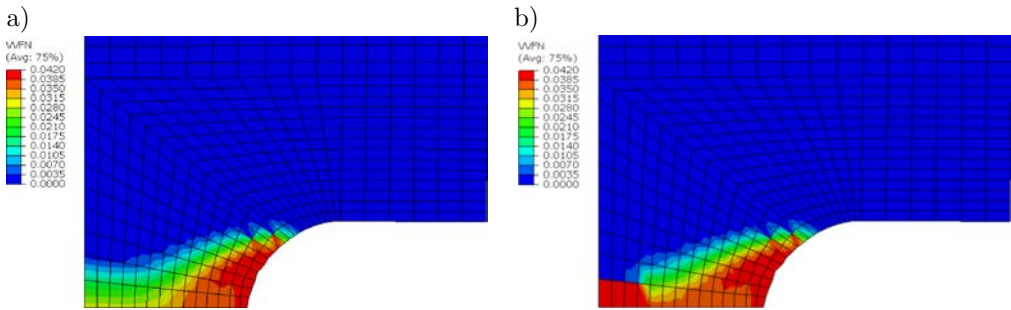


FIG. 22. Void Volume Fraction due to Void Nucleation $VVFN$, GTN model: a) $l = 1.04$ mm, b) $l = 1.07$ mm.

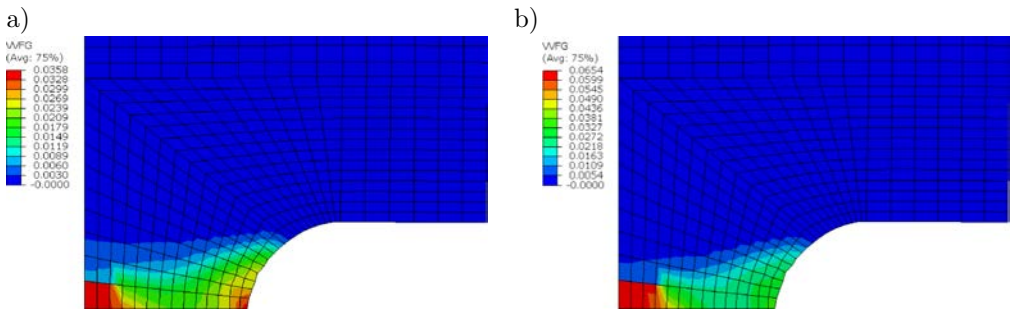


FIG. 23. Void Volume Fraction due to Void Growth $VVFg$, GTN model: a) $l = 1.04$ mm, b) $l = 1.07$ mm.

was observed using the *Cell model* in comparison to the *GTN model*. Critical values of Void Volume Fraction $VVF = 0.10$ and $VVF = 0.13$ at the material failure were noticed for $l = 1.066$ mm, respectively for the *GTN* and *Cell model* (Fig. 19, 20 and 25). In a further range of simulation increasingly higher values of VVF were observed when using *Cell model* compared to *GTN model*.

It can be seen clearly that the use of local softening of the material by using the *Cell model* has significant effects on the evolution of microdamage as

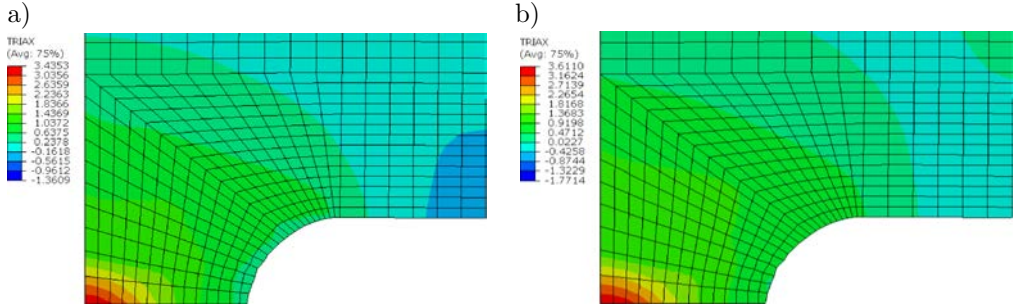


FIG. 24. Stress triaxiality maps σ_m/σ_e , *GTN model*: a) $l = 1.04$ mm, b) $l = 1.07$ mm.

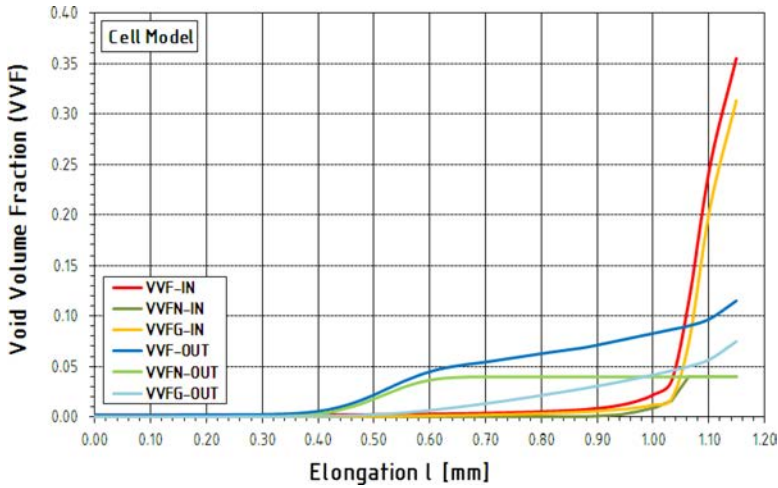


FIG. 25. Void Volume Fraction *VVF*, Void Volume Fraction due to Void Nucleation *VVFN* and Void Volume Fraction due to Void Growth *VVFG* versus elongation l curves for points IN and OUT, *Cell model*.

compared to the global approach, the *GTN model*. Assuming the porous material only in parts of an element leads on the one hand to the global strengthening, on the other hand, when the microvoids are growing, indicates a sudden drop in force, rapidly leading to the failure of the material.

Observed phenomena of evolution of microdamage described above are closely connected to changes in stress state around the bottom of the notch. When the load decreased, corresponding to the beginning of the material failure process, the increase of stress σ_m/σ_e was observed. These changes were less noticeable when using *GTN model*, where at the material failure the maximum value of σ_m/σ_e increased from of the value of $\sigma_m/\sigma_e = 3.44$ to $\sigma_m/\sigma_e = 3.61$ at the middle of element (Fig. 24). In the case of *Cell model* the above phenomena were more intense, because σ_m/σ_e increased almost twice, from $\sigma_m/\sigma_e = 2.12$ up to $\sigma_m/\sigma_e = 4.16$ (Fig. 29).

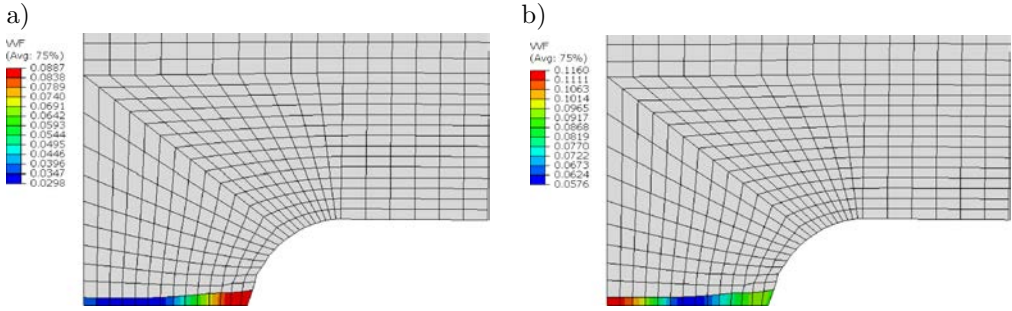


FIG. 26. Void Volume Fraction VVF maps, *Cell model*: a) $l = 1.06$ mm, b) $l = 1.10$ mm.

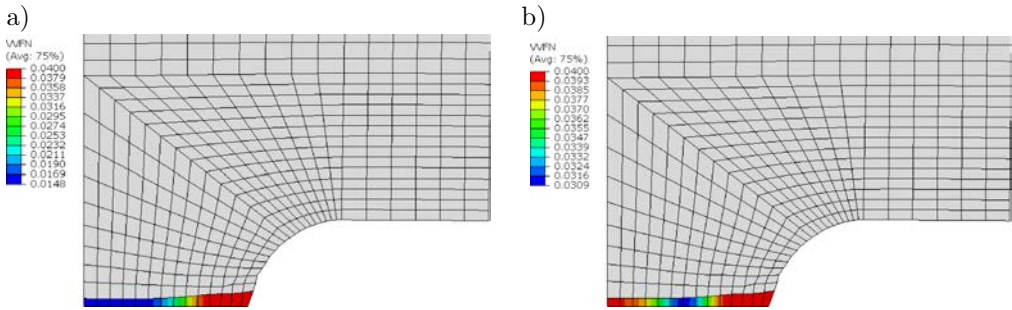


FIG. 27. Void Volume Fraction due to Void Nucleation VFN , *Cell model*: a) $l = 1.06$ mm, b) $l = 1.10$ mm.

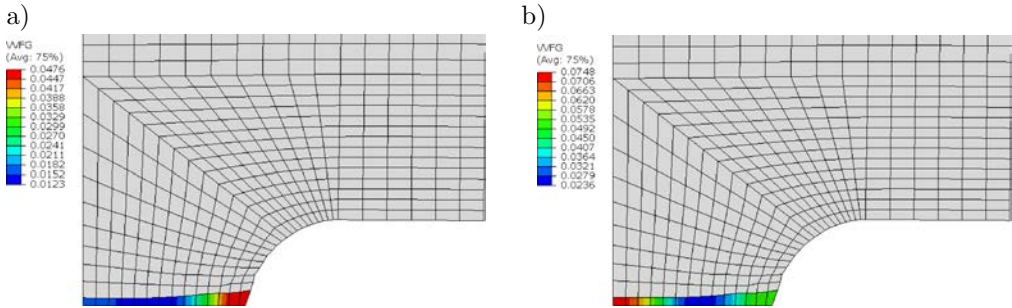


FIG. 28. Void Volume Fraction due to Void Growth VVG , *Cell model*: a) $l = 1.06$ mm, b) $l = 1.10$ mm.

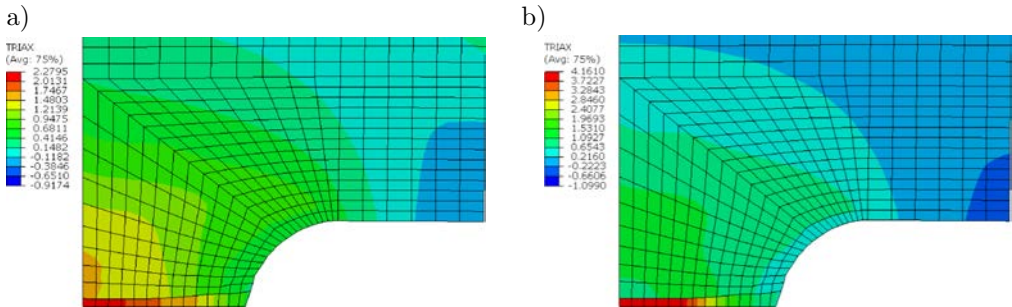


FIG. 29. Stress triaxiality maps σ_m/σ_e , *Cell model*: a) $l = 1.06$ mm, b) $l = 1.10$ mm.

Another characteristic phenomenon observed in all analysed elements was that the damage growth followed in a very small volume of material. Growth of voids included elements lying directly in the plane of the smallest cross section, near the bottom of the notch (Fig. 21–23). The same conclusion are drawn from both the microstructural studies and numerical simulations.

From the point of view of micro-simulation of the evolution of the material structure, using in numerical calculations the local approach gives qualitatively better results in comparison with the classical global approach. The assuming of the so-called *process zone*, however, requires determining in advance the places where one would expect nucleation and growth of microvoids, leading eventually to the failure. In very complicated cases, where it is difficult to one hundred percent certainty correctly identify the location and extent of *process zone*, the local approach could lead to errors, resulting in an underestimation or overestimation of the carrying capacity of the element. In such a situation it should be a two-step calculations applied, pre-specifying the damaged area, by using for example global *GTN model*. In the next stage of the calculation, with already defined *process zone*, it would be possible to assume a local approach, e.g. using *Cell* method.

5. CONCLUSIONS

The article presents the results of analysis of the microdamage evolution of S235JR steel under multi-axial stress state, based on the modified Gurson-Tvergaard-Needleman (GTN) model, taking into account the structure of the material.

To sum up the results of research it should be noted that:

- application of the modified GTN model taking into account the real parameters of the microstructure of steel S235JR made possible simulation of ductile failure,
- the tensile strength curves obtained by applying global *GTN model* and local *Cell model* were consistent with the experimental results,
- initial process of nucleation and growth of voids was particularly intense in the outer parts of elements; after the maximum force was reached the growth voids rate increased; at the moment when the force decreased suddenly, more intense growth of voids in the middle part in comparison to the outer part of elements was observed,
- the failure growth followed in a very small volume of material, covering the elements lying directly in the plane of the smallest cross section near the bottom of the notch; the same conclusion are drawn from both the microstructural studies and numerical simulations,

- application of a local softening of the material (*Cell model*) has significant effects on the evolution of microdamage as compared to the global approach (*GTN model*); the strengthening of the material is observed when the porous material is assumed only in parts of an element (*Cell model*); in such case a sudden drop in load, rapidly leading to the failure of the material is noticed due to the sudden microvoids growth,
- from the point of view of the micro-simulation of the voids evolution, the local approach applied during numerical simulations gives qualitatively better results in comparison to the classical global approach; the assuming of the so-called *process zone*, however, requires determining in advance the places where one would expect nucleation and growth of microvoids, leading eventually to the failure, which in many complex cases can lead to computational errors.

ACKNOWLEDGMENT

The research reported herein was conducted as part of Project R04 007 01 funded over the period 2006–2010 from education budget.

REFERENCES

1. BRIDGMAN P.W., *Studies in Large Plastic Flow and Fracture*, McGraw-Hill, New York, 1952.
2. TEIRLINCK D., ZOK F., EMBURY J.D., ASHBY M.F., *Fracture Mechanism Maps in Stress Space*, *Acta Metallurgica*, **36**, 5, 1213–1228, 1988.
3. GURSON A.L., *Continuum Theory of Ductile Rupture by Void Nucleation and Growth: Part I – Yield Criteria and Flow Rules for Porous Ductile Media*, *Journal of Engineering Materials and Technology*, *Transactions of the ASME*, **99**, 1, 2–15, 1977.
4. TVERGAARD V., *Influence of Voids on Shear Band Instabilities under Plane Strain Conditions*, *International Journal of Fracture*, **17**, 4, 389–407, 1981.
5. TVERGAARD V., NEEDLEMAN A., *Analysis of the Cup-Cone Fracture in a Round Tensile Bar*, *Acta Metallurgica*, **32**, 1, 157–169, 1984.
6. PN-EN 1993-1-10:2007 Eurocode 3: Design of Steel Structures – Part 1-10: Material Toughness and Through-thickness Properties.
7. SEDLACEK G., FELDMANN M., KÜHN B., TSCHICKARDT D., HÖHLER S., MÜLLER C., HENSEN W., STRANGHÖNER N., DAHL W., LANGENBERG P., MÜNSTERMANN S., BROZETTI J., RAOUL J., POPE R., BIJLAARD F., *Commentary and Worked Examples to EN 1993-1-10 “Material Toughness and Through-Thickness Properties” and Other Toughness Oriented Rules in EN 1993*, JRC Scientific and Technical Reports, European Commission Joint Research Centre, Luxembourg 2008.
8. TVERGAARD V., NEEDLEMAN A., *Effects of Nonlocal Damage in Porous Plastic Solids*, *International Journal of Solids and Structures*, **32**, 8/9, 1063–1077, 1995.

9. RAMASWAMY S., ARAVAS N., *Finite Element Implementation of Gradient Plasticity Models. Part II: Gradient-dependent Evolution Equations*, Computer Methods in Applied Mechanics and Engineering, **163**, 1–4, 33–53, 1998.
10. BORINO G., FAILLA B., PARRINELLO F., *A Symmetric Nonlocal Damage Theory*, International Journal of Solids and Structures, **40**, 13–14, 3621–3645, 2003.
11. KOSSAKOWSKI P., *The simulation of the plastic range for structural steels under multi-axial state of stress basing on the Gurson-Tvergaard-Needleman model* [in Polish: *Symulacja plastycznego zakresu pracy stali konstrukcyjnych w złożonym stanie naprężeń w oparciu o model Gursona-Tvergaard-Needlemana*], Przegląd Budowlany, **3**, 43–49, 2012.
12. KOSSAKOWSKI P., *An Analysis of the Load-Carrying Capacity of Elements Subjected to Complex Stress States with a Focus on the Microstructural Failure*, Archives of Civil and Mechanical Engineering, **10**, 2, 15–39, 2010.
13. KOSSAKOWSKI P.G., TRĄPWCZYŃSKI W., *Numerical simulation of S235JR steel failure with consideration of the influence of microstructural damages* [in Polish: *Numeryczna symulacja zniszczenia stali S235JR z uwzględnieniem wpływu uszkodzeń mikrostrukturalnych*], Przegląd Mechaniczny, **4**, 15–22, 2011.
14. KOSSAKOWSKI P.G., *Simulation of Ductile Fracture of S235JR Steel Using Computational Cells with Microstructurally-Based Length Scales*, Journal of Theoretical and Applied Mechanics, **50**, 2, 589–607, 2012.
15. FALESKOG J., GAO X., SHIH C.F., *Cell Model for Nonlinear Fracture Analysis – I. Micromechanics Calibration*, International Journal of Fracture, **89**, 4, 355–373, 1998.
16. GAO X., FALESKOG J., SHIH C.F., *Cell Model for Nonlinear Fracture Analysis – II. Fracture-Process Calibration and Verification*, International Journal of Fracture, **89**, 4, 375–398, 1998.
17. CORIGLIANO A., MARIANI S., ORSATTI B., *Identification of Gurson-Tvergaard Material Model Parameters Via Kalman Filtering Technique. I. Theory*, International Journal of Fracture, **104**, 4, 349–373, 2000.
18. TVERGAARD V., *Material Failure by Void Growth to Coalescence*, Advances in Applied Mechanics, **27**, 83–151, 1989.
19. The determination of the material structure (taken from the construction), comparative analysis with the parameters of the reference steel [in Polish: *Określenie struktury materiałów (pobranych z konstrukcji), analiza porównawcza z parametrami stali wzorcowej*], Technical report of the Project R04 007 01, Warsaw University of Technology, Warsaw 2008.
20. PN-EN 10002-1:2004 Metallic Materials – Tensile Testing – Part 1: Method of Test at Ambient Temperature.
21. Abaqus 6.10 Analysis User's Manual, Dassault Systèmes, Providence 2010.
22. RICHELSEN A.B., TVERGAARD V., *Dilatant Plasticity or Upper Bound Estimates for Porous Ductile Solids*, Acta Metallurgica et Materialia, **42**, 8, 2561–2577, 1994.
23. XIA L., SHIH C.F., *Ductile Crack Growth – I. A Numerical Study Using Computational Cells with Microstructurally-based Length Scales*, Journal of the Mechanics and Physics of Solids, **43**, 2, 233–259, 1995.

24. XIA L., SHIH C.F., *Ductile Crack Growth – II. Void Nucleation and Geometry Effects on Macroscopic Fracture Behavior*, Journal of the Mechanics and Physics of Solids, **43**, 12, 1953–1981, 1995.
25. HANCOCK J.W., MACKENZIE A.C., *On the Mechanisms of Ductile Failure in High-strength Steel Subjected to Multi-axial Stress-states*, Journal of Mechanics and Physics of Solids, **24**, 2-3, 147–160, 1976.

Received November 18, 2011; revised version October 1, 2012.

Controller Concept for a Highly Parallel Machine Tool

Christoph HABERSOHN, Friedrich BLEICHER

Vienna University of Technology
Institute for Production Engineering and Laser Technology
Landstraßer Hauptstraße 152, 1030 Wien, Austria
e-mail: habersohn@ift.at

Modern high performance cutting processes force high demands on new machine tool concepts with enhanced mechanical stability and better dynamic behavior. In the development of innovative machine tool concepts the main focus is still set on the design of mechanical structures with parallel kinematics. The new machining center “X-Cut” consists of a double scissor kinematic structure with a degree of parallelism of two, incorporating four drives for the XY -plane movement. Thus, the arrangement of four interlinked axes leads to an over-determined kinematic structure. Due to the complex behavior of the kinematic structure a new method in NC-controller design and parameterization is needed, including enhanced compensation and preloading algorithms.

Key words: machine tools, kinematic structure, parallel kinematics, control design, modeling, simulation.

1. INTRODUCTION

For more than 15 years, machine tools based on parallel kinematics have become more important in manufacturing and handling applications. In fact, the machine tool industry has great expectations in the development of this type of machine structure; especially with respect to criteria such as stiffness, acceleration, accuracy, and the advantage of realizing similar assembly parts. Regarding the number of similar mechanical components that have to be assembled, a remarkable effect on the economic efficiency in building up machine tools has been anticipated. Experience resulting from the practical application of parallel kinematics settled because the development of various machine tools fell short of expectations due to disadvantages coming along with the non-linear behaviour of the mechanical structure in the overall workspace envelope. Many prototypes of machine tool concepts offer static stiffness in one preferred axis of more than 100 N/ μm . The values of stiffness in the axes perpendicular to

the orientation of the struts drop down to very low levels of rarely more than $10 \text{ N}/\mu\text{m}$ [1, 2].

High performance cutting processes puts a high demand on the concept of new machine tools with improved mechanical stability and better dynamic behaviour. As a result of this, the main focus is set on the design of machine tool structures with parallel kinematics. The first types of machine tools based on parallel kinematics were built with a degree of parallelism of one, e.g. Quickstep and Quickstep Neon [3]. This implies that there are as many drives in the machine as there are degrees-of-freedom offered for the tool and the Tool Centre Point (TCP) respectively [2].

In order to overcome restrictions in mechanics due to non-linear behaviour, a new approach has been found with a highly parallel design representing a kinematic structure offering a degree of parallelism of two, called “X-Cut” [4, 5]. The main kinematic structure offers two degrees of freedom of motion, and hence it allows in-plane movements. This kind of movement can already be performed by a scissor-type of kinematic structure, e.g. the DynaM, as presented in [6]. In order to get preloads into all kinematic transmission elements the scissor kinematic has to be doubled, thus the “V”-shape of the structure design becomes an “X”-shape, and gives the name to the invention. Due to the over-determined kinematic structure, it is possible to influence the preloading of all kinematic transmission elements during machining and feed motion. Furthermore, the basic stiffness of the entire structure can be improved. Applying a preload also affects the structure’s damping characteristics whereby vibrations, which are introduced into the structure by reaction forces of acceleration and deceleration due to positioning motion of the main spindle as well as time variant processing forces, fade away much faster [4].

As a main focus of research, this innovative machine tool concept affords a new type of control algorithm because, in addition to the standard NC-controlled motion, it is necessary to integrate in the NC-control a strategy and control-functionality to handle and optimize the pretensioning forces. Hence, adaptive compensation methods have to be implemented with respect to motion and processing demands [7–11].

2. HARDWARE

The following figure illustrates the machine tool concept “X-Cut”, with a 2D-overdetermined kinematic structure highlighted in the colour red. The third degree of motion is allocated in the work-piece slide. The control unit and the drives were provided by the Austrian control system vendor, Bernecker & Rainer [5].

To realize a minimum CPU cycle time of $800 \mu\text{s}$, an APC 620 is used with a PP480 CNC panel in terminal mode as a HMI. The positioning of servo drives is



FIG. 1. Machine tool concept X-Cut.

controlled by five ACOPOSmulti and a 30 kW spindle by an ACOPOS. These servo motor controllers have a cyclic bus time of 400 μ s. In addition to the internal absolute encoder of the drives, each axis has a Heidenhain glass linear scale mounted at the carriage to gain increased position accuracy [12].

3. SOFTWARE

The machine tool NC-control is based on the Generic Motion Control software of Bernecker & Rainer. The system is configured with a virtual Cartesian coordinate system which is coupled with the real axis by an inverse transformation. The real TCP position is calculated by the virtual axis using a direct transformation of the physical axis. Regarding the software structure in this way, all positioning movements are defined by the Cartesian axes system and the physical axes follow the set points. The motion path itself is generated by the positioning requests directly to the virtual axes or by the NC kernel “ARNC0”

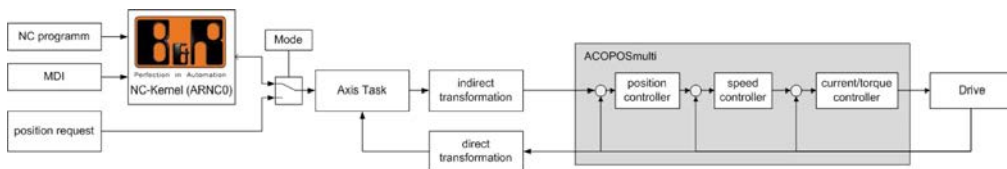


FIG. 2. Indirect and direct transformation.

which interprets G-code based on DIN 66025 from a NC-file or the input of the MDI. In any case, the position request is updated every 800 μ s [12].

The ACOPOSmulti works with a three-layer controller architecture. In addition to the main positioning PI-controller, a secondary speed-controller and a third torque controller is subordinated. Each controller can be adjusted separately by the proportional band, the integral time and an offset, which can be altered at runtime with the active axis control.

3.1. Direct transformation

The direct transformation calculates the X -, Y -, and Z -position of the TCP in the workspace envelope using the real axis position. This is necessary for the control task to interpret position requests in an accurate way and send the real position to the HMI and the ARNC0. In fact, only the X - and the Y -positions have to be calculated, whereas the virtual Z -axis is defined by the position measure of the axis Q_5 in the physical system.

For the calculation of the TCP-position, only the positions of two axes are necessary. Thus in the first version of implementation, axes one and two were used (see Fig. 3). To get a more symmetric situation an arrangement of op-

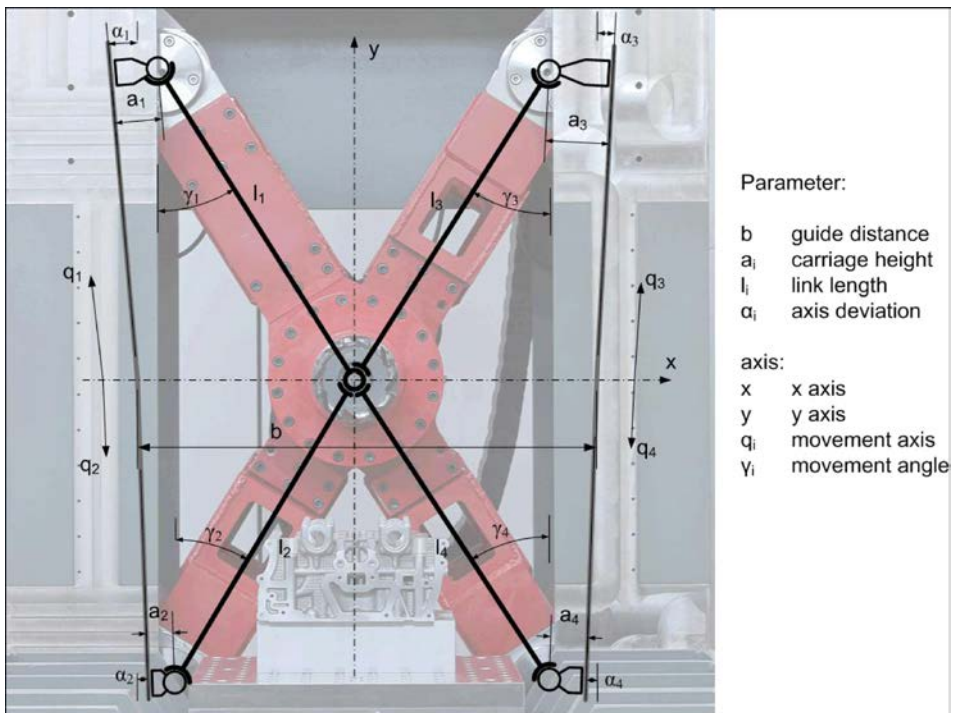


FIG. 3. Machine tool structure of X-Cut and kinematic parameters.

posing axes has been used in a second version by taking axes one and three in the position control loop. The following equations represent the direct coordinate system transformation, where C_1 and C_2 are calculated as two constants representing the geometrical dimensions as described in Fig. 3.

$$C_1 = b + q_1 \sin(\alpha_1) - a_1 \cos(\alpha_1) - a_3 \cos(\alpha_3) + q_3 \sin(\alpha_3),$$

$$C_2 = q_1 \cos(\alpha_1) + a_1 \sin(\alpha_1) - a_3 \sin(\alpha_3) - q_3 \cos(\alpha_3),$$

$$\beta = \arcsin\left(\frac{l_1^2 - l_3^2 + C_1^2 + C_2^2}{2l_1\sqrt{C_1^2 + C_2^2}}\right) - \arctan\left(\frac{C_2}{C_1}\right),$$

$$x = -\frac{b}{2} - q_1 \sin(\alpha_1) + a_1 \cos(\alpha_1) + l_1 \sin(\beta + \alpha_1),$$

$$y = q_1 \cos(\alpha_1) + a_1 \sin(\alpha_1) - l_1 \cos(\beta + \alpha_1),$$

$$z = q_5.$$

3.2. Indirect transformation

An indirect transformation is used to calculate the positional set-points of the real axes $Q1-Q5$ based on the X -, Y -, and Z -positions. The indirect transformation is very important to realize a closed loop position control in the NC-controller. The following equations describe the determination for each axis.

Axis $Q1$:

$$x = -\frac{b}{2} - q_1 \sin(\alpha_1) + a_1 \cos(\alpha_1) + l_1 \sin(\gamma_1),$$

$$y = q_1 \cos(\alpha_1) + a_1 \sin(\alpha_1) - l_1 \cos(\gamma_1),$$

with

$$R = x + \frac{b}{2} - a_1 \cos(\alpha_1),$$

$$S = y - a_1 \sin(\alpha_1),$$

$$q_1 = S \cos(\alpha_1) - R \sin(\alpha_1) + \sqrt{(S \cos(\alpha_1) - R \sin(\alpha_1))^2 + (l_1^2 - R^2 - S^2)}.$$

Axis $Q2$:

$$x = -\frac{b}{2} + q_2 \sin(\alpha_2) + a_2 \cos(\alpha_2) + l_2 \sin(\gamma_2),$$

$$y = -q_2 \cos(\alpha_2) + a_2 \sin(\alpha_2) + l_2 \cos(\gamma_2),$$

with

$$R = x + \frac{b}{2} - a_2 \cos(\alpha_2),$$

$$S = y - a_2 \sin(\alpha_2),$$

$$q_2 = -S \cos(\alpha_2) + R \sin(\alpha_2) + \sqrt{(S \cos(\alpha_2) - R \sin(\alpha_2))^2 + (l_2^2 - R^2 - S^2)}.$$

Axis Q3:

$$x = \frac{b}{2} + q_3 \sin(\alpha_3) - a_3 \cos(\alpha_3) - l_3 \sin(\gamma_3),$$

$$y = q_3 \cos(\alpha_3) + a_3 \sin(\alpha_3) - l_3 \cos(\gamma_3),$$

with

$$R = -x + \frac{b}{2} - a_3 \cos(\alpha_3),$$

$$S = y - a_3 \sin(\alpha_3),$$

$$q_3 = S \cos(\alpha_3) - R \sin(\alpha_3) + \sqrt{(S \cos(\alpha_3) - R \sin(\alpha_3))^2 + (l_3^2 - R^2 - S^2)}.$$

Axis Q4:

$$x = \frac{b}{2} - q_4 \sin(\alpha_4) - a_4 \cos(\alpha_4) - l_4 \sin(\gamma_4),$$

$$y = -q_4 \cos(\alpha_4) + a_4 \sin(\alpha_4) + l_4 \cos(\gamma_4),$$

with

$$R = -x + \frac{b}{2} - a_4 \cos(\alpha_4),$$

$$S = y - a_4 \sin(\alpha_4),$$

$$q_1 = -S \cos(\alpha_4) + R \sin(\alpha_4) + \sqrt{(S \cos(\alpha_4) - R \sin(\alpha_4))^2 + (l_4^2 - R^2 - S^2)}.$$

The indirect transformation of the Z -axis is realized in a serial arrangement concerning the design of mechanical structure. Hence, the transformation can be calculated easily, and is equal to the position measure on the physical axis.

Axis Q5:

$$q_5 = z.$$

3.3. Parameter identification

To enhance the accuracy of the transformation, the real geometrical dimensions of the machine tool structure were determined by comparison of theoretically calculated and actually given position of the TCP by the use of redundant measurement devices. To minimize complexity, the carriage height is set to the theoretical value of the construction. Thereby the parameters: link length, guide distance and movement angle were determined, as well as the deviation in the X-axis of the not parameterised system.

4. CONTROLLER STRATEGIES

Regarding the concepts of position controller, two types of controller strategies can be distinguished.

4.1. Control system with four position controlled axes

In this arrangement four axes of the parallel kinematics structure are in a positioning control loop, called 4P-controller, as illustrated in Fig. 4. This type of strategy imposes a higher demand on the machine calibration because even a small position inaccuracy leads to high forces in the structure and in the drives. Due to an inaccuracy in the determination of real geometry, deviations between the real and the ideal kinematics arise. Thus, no power reserve exists for move-

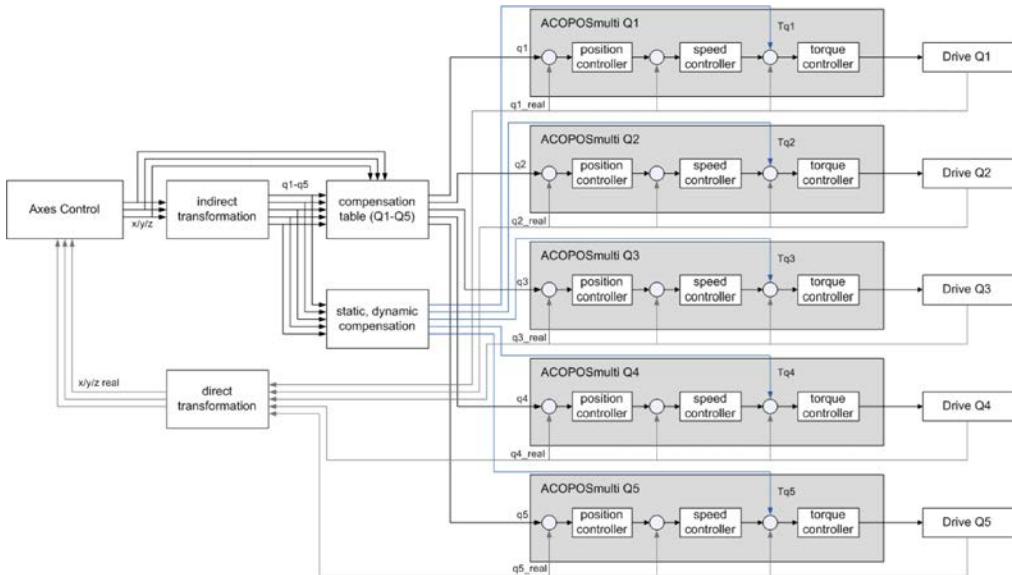


FIG. 4. Control strategy using four position controlling loops in the kinematics structure.

ment in the case of imprecise compensation. By high speed movements especially, even minor inaccuracies in the mechanical system generate huge torques in the drives and lead to overcharge of the drives.

An advantage is that all drives indicate the positioning movement and therefore the maximum torque of all drives can be used for the acceleration. Additionally the indicated forces of the cutting process are carried by all axes which enhance the machine stiffness behaviour.

4.2. Control system with two position and two force controlled axes

A second type of control strategy is based on the use of two axes, which are in position control loops, and two other axes, which are driven by a force control loop (see Fig. 5). Thus, the positioning of the TCP is done by two of the four axes and the other two axes tense the kinematic with a predefined force. The advantage of this system is focussing on the effect that geometrical inaccuracies are widely eliminated in the influence on the closed loop motion control.

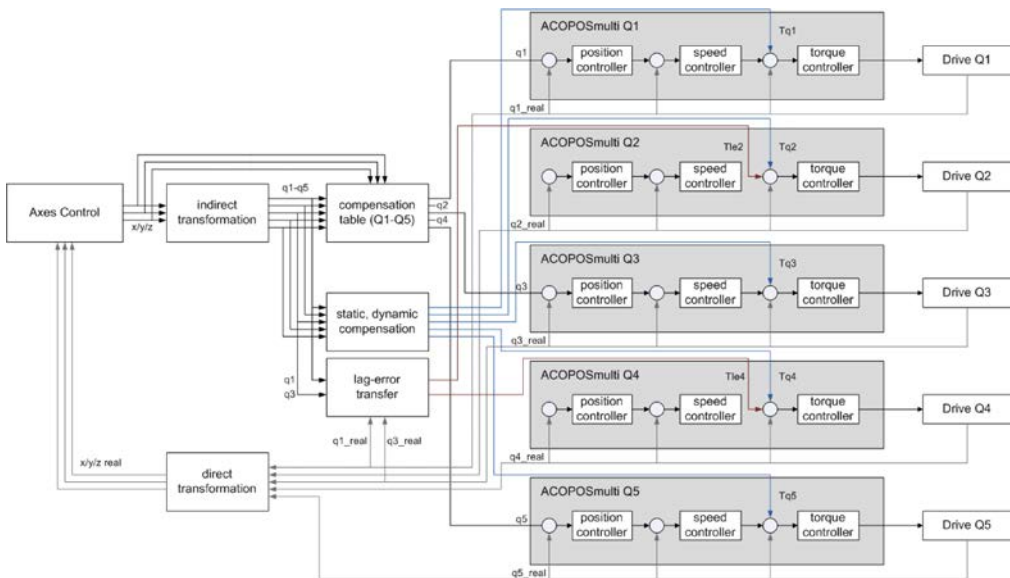


FIG. 5. Control strategy using two position controlling and two force controlling loops.

On the other hand, the force driven struts are not able to carry unknown external process forces, which lead to higher positioning inaccuracies as shown by the 4P controller strategy. Furthermore, the preloading forces had to be adjusted with respect to the movement, which generates higher demands on the control unit.

5. COMPENSATION

To fulfil today’s machining demands on positioning accuracies different compensation algorithms are implemented in the machine control.

5.1. Axis inaccuracies

In order to implement compensation functionality in the NC-controller the deviations of the real positioning motions to the reference values has been measured. Every 50 mm in square of the *XY*-working plane the deviations of the axes position in comparison to the calculated positions were measured by a mechanical 3D-measuring device. Based on these correction values a linear planar interpolation depending on the *X*- and *Y*-position is calculated for each axis and charged to the calculated position values (see Fig. 6).

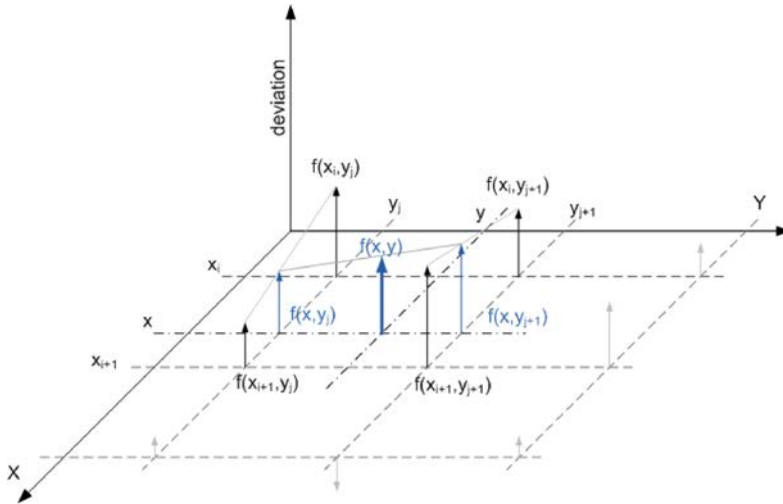


FIG. 6. Compensation of position inaccuracies.

The planar linear interpolation can be calculated in two steps.

$$f(x_i, y_j) \quad \text{with discrete} \quad x_0 - x_n, \quad y_0 - y_n.$$

Linear interpolation:

$$f(x, y_j) = f_{i,j} + \frac{f_{i+1,j} - f_{i,j}}{x_{i+1} - x_i}(x - x_i),$$

$$f(x, y_{j+1}) = f_{i,j+1} + \frac{f_{i+1,j+1} - f_{i,j+1}}{x_{i+1} - x_i}(x - x_i).$$

Linear interpolation in the X- and Y-axes:

$$f(x, y) = f(x, y_j) + \frac{f(x, y_{j+1}) - f(x, y_j)}{y_{j+1} - y_j}(y - y_j).$$

5.2. Static and dynamic compensation

The compensation is based on Newton's axioms. To minimize the computing time the masses of each slide and the rods are modelled as rigid bodies with the masses represented by the centre of gravity and mass of inertia. Furthermore, the axis deviation angle of geometric specification is set to zero.

To solve over-determination, the rod system is divided into two substructures. One system is built up of links $Q1$ and $Q2$, and the other of links $Q3$ and $Q4$. The systems are connected by a definable horizontal force. Thus, the forces in the carriages are set to values that the system on the right side presses with a defined horizontal force against the system on the left side. In a second step, gravity, acceleration, and friction forces are added. Based on these results the spindle torque of the NC-drives is calculated. The following figure illustrates the force system.

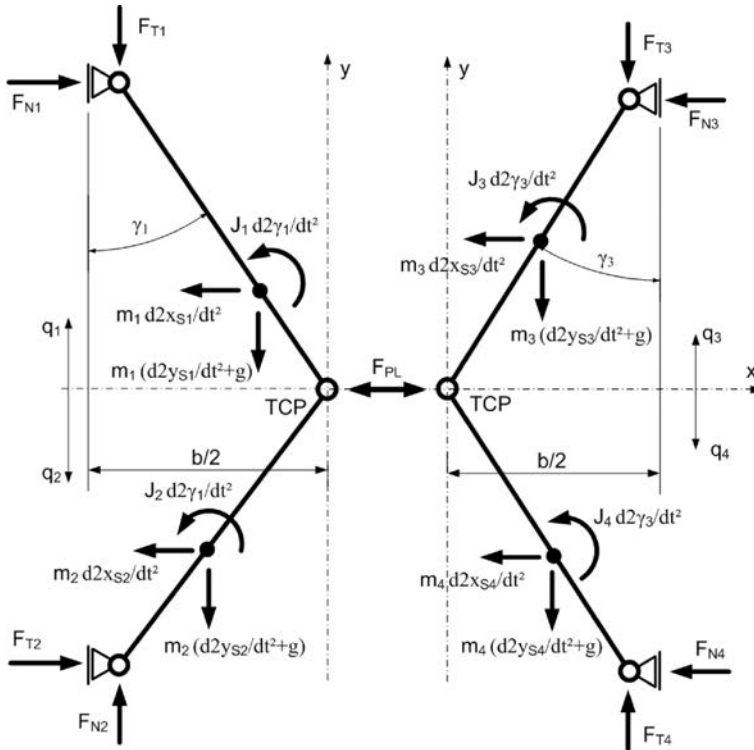


FIG. 7. Parameters for calculation of static and dynamic compensation.

Calculation of the sum of torques in TCP concerning rod $Q1$:

$$J_1\ddot{\varphi}_1 - m_1\ddot{x}_{S1}(l_1 - l_{S1}) \cos(\varphi_1) - m_1(\ddot{y}_{S1} - g)(l_1 - l_{S1}) \sin(\varphi_1) \\ + F_{T1}l_1 \sin(\varphi_1) + F_{N1}l_1 \cos(\varphi_1) = 0,$$

$$C_1 = J_1\ddot{\varphi}_1 - m_1\ddot{x}_{S1}(l_1 - l_{S1}) \cos(\varphi_1) - m_1(\ddot{y}_{S1} - g)(l_1 - l_{S1}) \sin(\varphi_1),$$

$$F_{N1} = -C_1 \frac{1}{l_1 \cos(\varphi_1)} - F_{T1} \frac{\sin(\varphi_1)}{\cos(\varphi_1)}.$$

Calculation of the sum of torques in TCP concerning rod $Q2$:

$$J_2\ddot{\varphi}_2 - m_2\ddot{x}_{S2}(l_2 - l_{S2}) \cos(\varphi_2) + m_2(\ddot{y}_{S2} - g)(l_2 - l_{S2}) \sin(\varphi_2) \\ - F_{T2}l_2 \sin(\varphi_2) + F_{N2}l_2 \cos(\varphi_2) = 0,$$

$$C_2 = J_2\ddot{\varphi}_2 - m_2\ddot{x}_{S2}(l_2 - l_{S2}) \cos(\varphi_2) + m_2(\ddot{y}_{S2} - g)(l_2 - l_{S2}) \sin(\varphi_2),$$

$$F_{N2} = -C_2 \frac{1}{l_2 \cos(\varphi_2)} + F_{T2} \frac{\sin(\varphi_2)}{\cos(\varphi_2)}.$$

Force addition of rod $Q1$ and $Q2$:

$$F_{PL} + m_1\ddot{x}_{S1} + m_2\ddot{x}_{S2} - F_{N1} - F_{N2} = 0,$$

$$F_{T2} = \left(F_{PL} + m_1\ddot{x}_{S1} + m_2\ddot{x}_{S2} + C_1 \frac{1}{l_1 \cos(\varphi_1)} + F_{T1} \frac{\sin(\varphi_1)}{\cos(\varphi_1)} \right) \frac{\cos(\varphi_2)}{\sin(\varphi_2)} \\ + C_2 \frac{1}{l_2 \sin(\varphi_2)}.$$

Force addition in the Y -direction of rods $Q1$ and $Q2$:

$$m_1(\ddot{y}_S - g) + m_2(\ddot{y}_{S2} - g) - F_{T1} - F_{T2} = 0,$$

$$F_{T1} \left(1 + \frac{\tan(\varphi_1)}{\tan(\varphi_2)} \right) = m_1(\ddot{y}_{S1} - g) + m_2(\ddot{y}_{S2} - g) \\ - \left(F_{PL} + m_1\ddot{x}_{S1} + m_2\ddot{x}_{S2} + C_1 \frac{1}{l_1 \cos(\varphi_1)} \right) \frac{\cos(\varphi_2)}{\sin(\varphi_2)} + C_2 \frac{1}{l_2 \sin(\varphi_2)} = 0.$$

Resulting force in the slide system of rod $Q3$:

$$J_3\ddot{\varphi}_3 - m_3\ddot{x}_{S3}(l_3 - l_{S3}) \cos(\varphi_3) - m_3(\ddot{y}_{S3} - g)(l_3 - l_{S3}) \sin(\varphi_3) \\ + F_{T3}l_3 \sin(\varphi_3) + F_{N3}l_3 \cos(\varphi_3) = 0,$$

$$C_3 = J_3\ddot{\varphi}_3 + m_3\ddot{x}_{S3}(l_3 - l_{S3}) \cos(\varphi_3) - m_3(\ddot{y}_{S3} - g)(l_3 - l_{S3}) \sin(\varphi_3),$$

$$F_{N3} = -C_3 \frac{1}{l_3 \cos(\varphi_3)} - F_{T3} \frac{\sin(\varphi_3)}{\cos(\varphi_3)}.$$

Resulting force in the slide system of rod $Q4$

$$J_4\ddot{\varphi}_4 + m_4\ddot{x}_{S4}(l_4 - l_{S4}) \cos(\varphi_4) + m_3(\ddot{y}_{S4} - g)(l_4 - l_{S4}) \sin(\varphi_4) - F_{T4}l_4 \sin(\varphi_4) + F_{N4}l_4 \cos(\varphi_4) = 0,$$

$$C_4 = J_4\ddot{\varphi}_4 + m_4\ddot{x}_{S4}(l_4 - l_{S4}) \cos(\varphi_4) + m_3(\ddot{y}_{S4} - g)(l_4 - l_{S4}) \sin(\varphi_4),$$

$$F_{N4} = -C_4 \frac{1}{l_4 \cos(\varphi_4)} + F_{T4} \frac{\sin(\varphi_4)}{\cos(\varphi_4)}.$$

Force addition in the X -direction of rods $Q3$ and $Q4$:

$$F_V - m_3\ddot{x}_{S3} - m_4\ddot{x}_{S4} - F_{N3} - F_{N4} = 0,$$

$$F_{T4} = \left(F_V - m_3\ddot{x}_{S3} - m_4\ddot{x}_{S4} + C_3 \frac{1}{l_3 \cos(\varphi_3)} + F_{T3} \frac{\sin(\varphi_3)}{\cos(\varphi_3)} \right) \frac{\cos(\varphi_4)}{\sin(\varphi_4)} + C_4 \frac{1}{l_4 \sin(\varphi_4)}.$$

Force addition in the Y -direction of rods $Q3$ and $Q4$:

$$m_3(\ddot{y}_{S3} - g) + m_4(\ddot{y}_{S4} - g) - F_{T3} - F_{T4} = 0,$$

$$F_{T3} \left(1 + \frac{\tan(\varphi_3)}{\tan(\varphi_4)} \right) = m_3 \left(\ddot{y}_{S3} - g + \frac{\ddot{x}_{S3}}{\tan(\varphi_4)} \right) + m_4 \left(\ddot{y}_{S4} - g + \frac{\ddot{x}_{S4}}{\tan(\varphi_4)} \right) - \frac{F_V}{\tan(\varphi_4)} - \frac{C_3}{l_3 \cos(\varphi_3) \tan(\varphi_4)} - \frac{C_4}{l_4 \sin(\varphi_4)}.$$

Consideration of the friction in the carriage:

$$F_{ri} = F_{Ni} \mu_r \cdot \text{sign}(\dot{q}_i).$$

Consideration of the inertial force of the carriage:

$$F_{ai} = m_{C_i} \ddot{q}_i.$$

Calculation of the torque at the drives:

$$T_i = (F_{Ti} + F_{ri} + F_{ai}) \frac{h_i}{2\pi\eta_G\eta_S}.$$

5.3. Lag error transfer

To indicate at the force controlled axis a position control, the lag error of the position controlled axis is transferred to the force controlled axis; thus inaccuracies in the geometry are eliminated. As shown in the following figure the transferred lag error can be considered as an input of a P-controller for an additional torque to the axis.

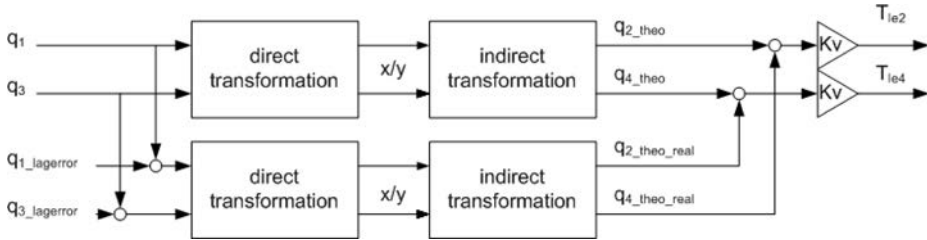


FIG. 8. Lag error transfer.

As a main disadvantage of this method can be observed that the calculation task act as a dead time element with the cyclic time between the input and the calculated output.

6. RESULTS OF EXPERIMENTS

The tests on the real machine were performed by realizing a circular path around the X- and Y-origin with a diameter of 300 mm. The focus of the investigation was to enhance the dynamics of the machine tool (see Fig. 9).

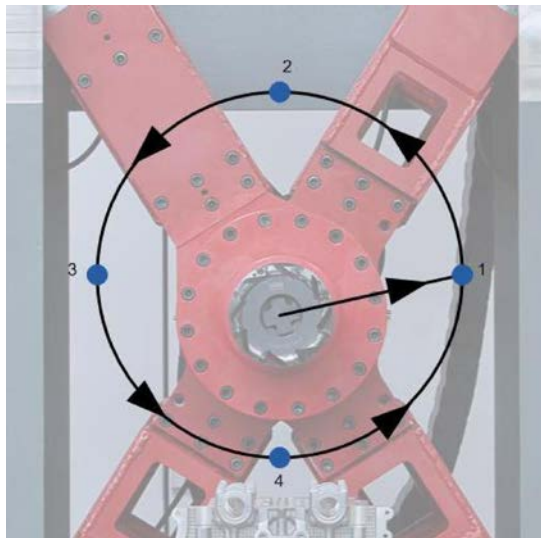


FIG. 9. Test program on the prototype machine.

6.1. Test of control strategy with lag error transfer

In performing tests, in order to investigate the lag error transfer, the axes $Q1$ and $Q2$ were position controlled and the axes $Q3$ and $Q4$ force controlled. The preloading torque was calculated by static compensation as well as the lag error transfer. The constant Kv is the proportional gain with a dimension of $\text{Nm}/\mu\text{m}$.

As presented in Fig. 10 the axis $Q1$ oscillates at the extended position of axes $Q1$ and $Q2$. The lag error transfer prevents this oscillation but causes higher torques on the other drives. Therefore this kind of additional torque eliminates the drive reserves for higher acceleration and movement speed. It is not possible to realize a feed rate of 60 m/min.

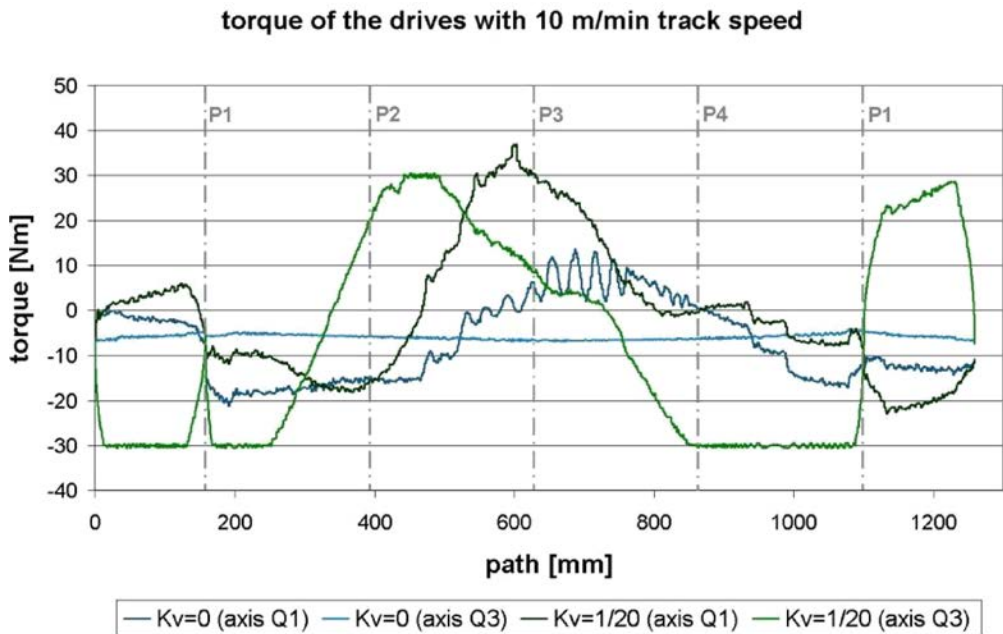


FIG. 10. Torque of the drives with lag error transfer.

6.2. Control Strategy with static and dynamic compensation

To minimize the extended position of the position controlled axis, the axis $Q2$ was replaced by axis $Q3$. Hence it was possible to increase the speed up to 45 m/min.

Figures 11 and 12 show the results of torque measurement of drive $Q1$ and the measured lag error in the XY -plane. At higher path speed the torques and the lag error increase, whereas the oscillation of the values decreases.

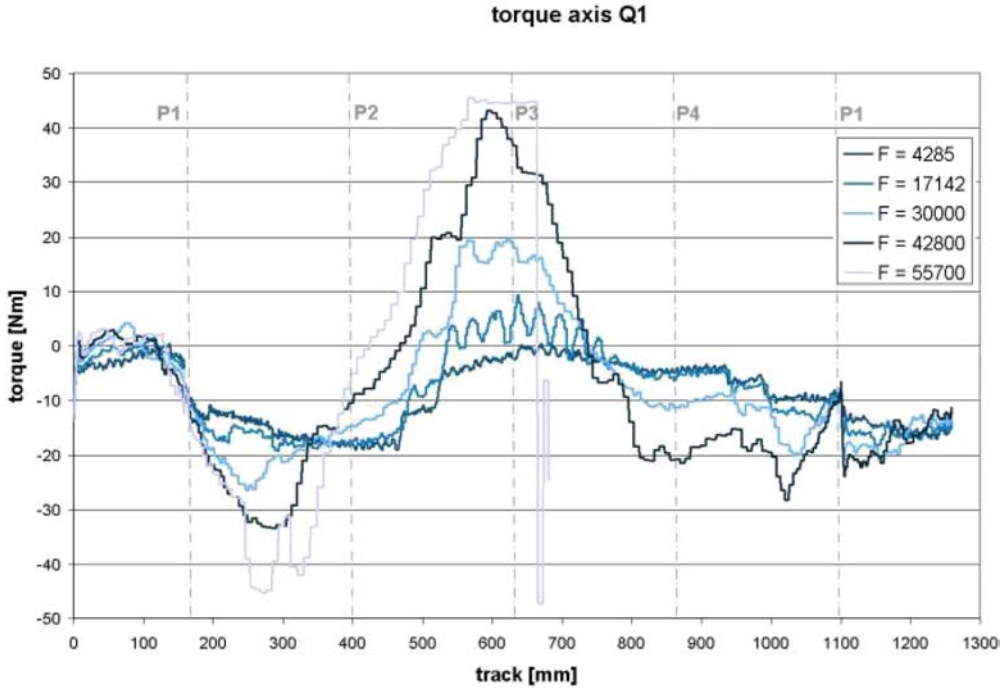


FIG. 11. Torque values measured on axis Q1 with different feeding rate.

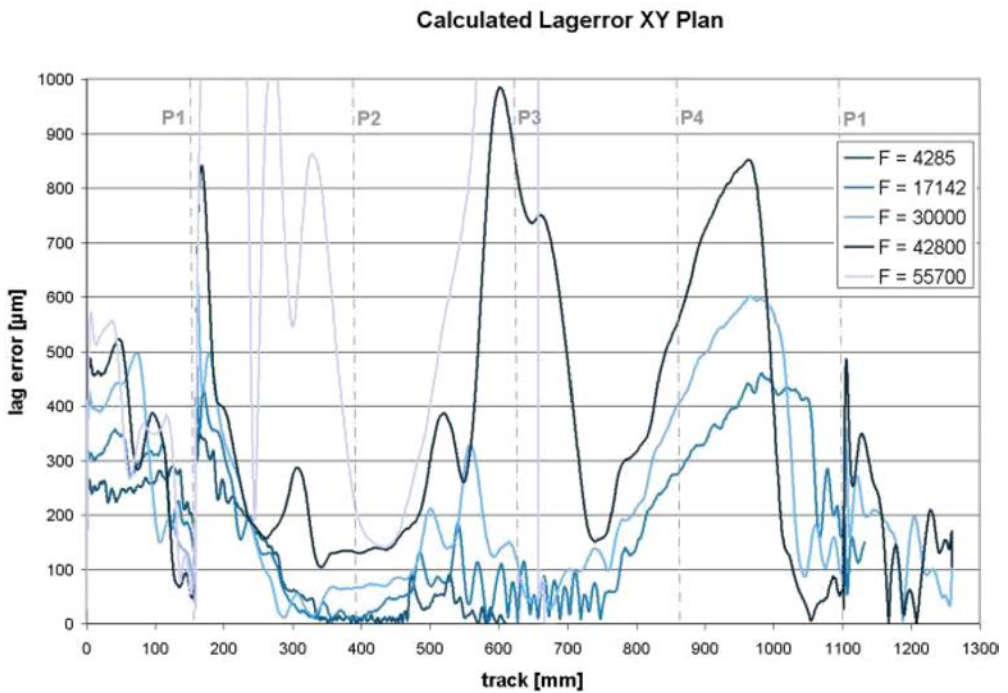


FIG. 12. Measurement results of lag error in the XY-plane with different feeding rate.

6.3. Control strategy comparison

In these tests different strategies focussed on the control implementation of a single axis have been investigated; though as a first step, the 4P-control concept was changed to a 3P1F-control concept. It can be demonstrated that this change in control strategy provides a reduction of the overcharge in the drives due to inaccuracies of the structure.

In Fig. 13 and Fig. 14 it is illustrated that the control concept using three position controlled axes cause at the feed rate of 20 m/min the highest values of measured torques and lag errors.

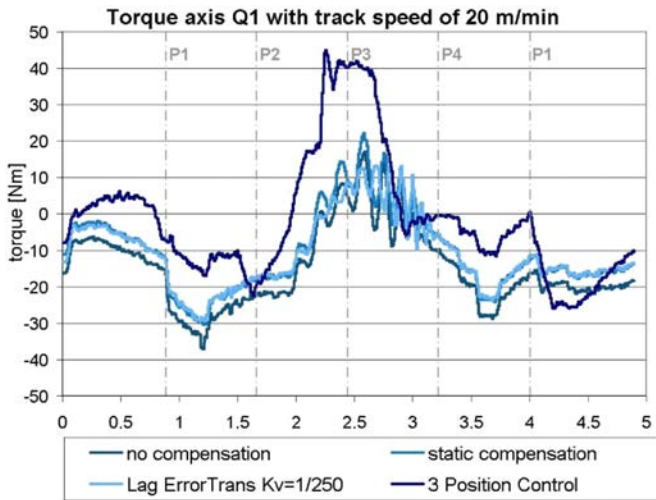


FIG. 13. Measured torque of axis Q1 with different strategies.

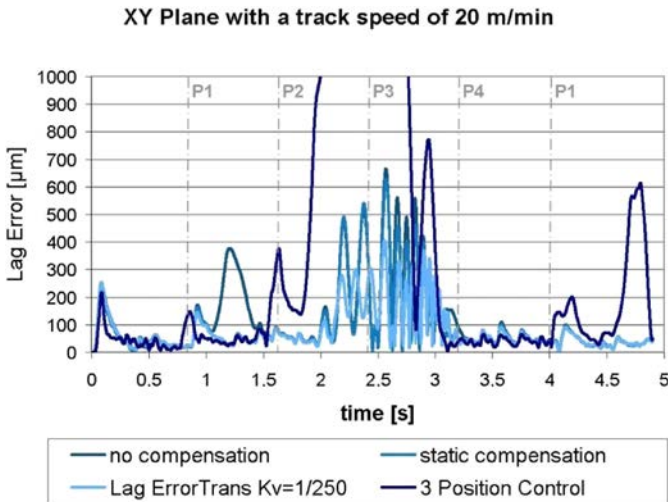


FIG. 14. Measured lag error in the XY-plane with different strategies.

7. CONCLUSIONS

The development of a machine tool with a highly parallel kinematics structure comes along with the need of new concepts for compensation of geometrical as well as static and dynamic deviations. Different strategies for compensation and their influence on the position control behavior were investigated. In general the charge of each drive can be reduced by the predefined torques, and thereby higher feed rates and acceleration are possible. Applying a controller strategy using two drives with position control and two drives with force control, oscillations are generated around the extended positions of the driven axes. This effect could be eliminated by a switch of the position dependent axes from one side-pair of struts to the other. The requirement of this change is dependent on the X - and Y -position of the TCP and on which pair of axes is closer to the point of singularity. Using a control strategy with four position controlled axes, nearly oscillation-free motion is possible. The generated drive torques come along with higher values to compensate the restraining forces in the structure. With enhanced predefined torque algorithms it will be possible to distribute the charge uniformly to all axes and increase the maximum feed rate, acceleration, and accuracy.

REFERENCES

1. NEUGEBAUER R., STOLL A., KIRCHNER J., IHLENFELDT S., *Gestaltung, Bewertung und Einsatzerfahrungen von Parallelkinematiken* [in:] FTK 2000, Stuttgarter Impulse, Technologien für die Zukunft, Stuttgart: Springer-Verlag, p. 316–333, 2000.
2. NEUGEBAUER R., *Parallelkinematische Maschinen*, Springer-Verlag Berlin Heidelberg, ISBN 978-3-5402-9939-4, 2006.
3. BLEICHER F., *Parallelkinematische Werkzeugmaschinen*, Neuer wissenschaftlicher Verlag Wien, ISBN 978-3-7083-0118-1, 2003.
4. BLEICHER F., *Optimizing a Three-Axes Machine-Tool with Parallel Kinematic Structure*, [in:] Parallel Kinematics Seminar Chemnitz: “Development Methods and Application Experience of Parallel Kinematics”, Verlag Wissenschaftliche Scripten Zwickau, Zwickau, p. 883–890, 2002.
5. MIKATS T., PUSCHITZ F., BLEICHER F., *New Machine Tool Concept ‘X-Cut’*, http://www.brautomation.com/files_br_com/Mikats09_New_Machine_Tool_Concept_X-Cut.pdf, 2009.
6. RWTH Aachen, WZL, Presentation site, “HüllerHille – DynaM”, <http://www.wzl.rwth-aachen.de/de/71b57339ef7396f0c1257792002a55b6.htm>, 2011.
7. BEYER L., *Genauigkeitssteigerung von Industrierobotern*, Insbesondere mit Parallelkinematik, Hamburg: Shaker Verlag, 2004.

8. KRÜGER P., *Innovative Steuerungsalgorithmen für Parallelkinematiken*, [in:] Fortschritt-Bericht VDI, Innovative Werkzeugmaschinen mit Parallelkinematik, Düsseldorf: VDI Verlag GmbH, p. 23–42, 2002.
9. GARBER T., LEHNER W.-D., *Antriebsregelungen bei Parallelkinematiken*, [in:] Fortschritt-Bericht VDI, Innovative Werkzeugmaschinen mit Parallelkinematik, Düsseldorf: VDI Verlag GmbH, p. 43–58, 2002.
10. HEISEL U., MAIER W., *DFG SPP 1099 – Production Machines with Parallel Kinematics*, [in:] The 5th Chemnitz Parallel Seminar, Parallel Kinematic Machines in Research and Practice, Zwickau: Verlag Wissenschaftliche Scripten, p. 13–39, 2006.
11. BRECHER C., OSTERMANN T., FRIEDRICH D.A., *Control Concept for PKM Considering the Mechanical Coupling between Actuators*, [in:] The 5th Chemnitz Parallel Seminar, Parallel Kinematic Machines in Research and Practice, Zwickau: Verlag Wissenschaftliche Scripten, p. 413–442, 2006.
12. Bernecker + Rainer Industrie-Elektronik Ges.m.b.H, B&R Product Catalog, Eggelsberg: Bernecker + Rainer Industrie-Elektronik Ges.m.b.H., 2011.

Received April 16, 2012; revised version September 28, 2012.

Selection of Shaped Charge Liner Material with the Use of Electromagnetic Expanding Ring Technique

Jacek JANISZEWSKI

Military University of Technology
Department of Mechatronics and Aviation
gen. Sylwestra Kaliskiego 2, 00-908 Warszawa, Poland
e-mail: jacek.janiszewski@wat.edu.pl

The present work deals with an experimental study on various sorts of copper was carried out with the use of an electromagnetic launching ring technique in order to select the material with a desirable property for performance of a shaped charged jet. The obtained results proved that the copper with the smallest grain size revealed the highest ductility under electromagnetic expanding ring loading conditions. The performed observations seem also to suggest that the electromagnetic expanding ring test may be applied as a tool for a choice of liner materials.

Key words: electromagnetic ring test, metals ductility, high strain rate deformation, shaped charge liner materials.

1. INTRODUCTION

The knowledge of correlation between a mechanical liner material property and behaviour of a shaped charged jet is remarkably important for designing high-performance HEAT projectiles. The penetration capability of these projectiles depends mainly on density of a liner material ρ_j and the maximum length of the jet L . The value of the theoretical possible penetration depth P can be determined applying the following simple equation:

$$(1.1) \quad P = L \sqrt{\frac{\rho_j}{\rho_t}},$$

where by ρ_t denotes the target material density [1].

The maximum length of the jet is theoretically determined by the velocity difference of jet tip $v_{j \max}$ and cut-off velocity $v_{j \min}$, and jet fragmentation time t_f (Fig. 1), however, both $v_{j \max}$ and t_f are limited by other parameters. The maximum jet tip velocity $v_{j \max}$ is limited by a factor of the bulk-sound velocity of the liner material, whereas jet fragmentation time t_f is restricted by ductility of the liner material.

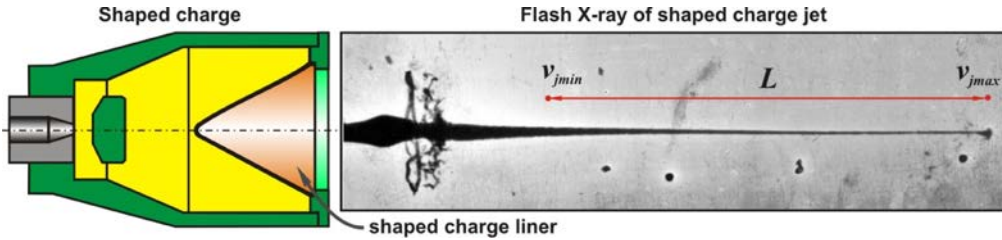


FIG. 1. Typical shaped charge configuration and rentgenogram of shaped charge jet.

The liner material ductility is critical owing to the penetration potential of shaped charges [2]. Therefore, the main purpose of the liner fabrication technology (besides achievement of required liner geometry) is the transformation of a metallurgical state of the starting liner material into the correct metallurgical characteristics of the final liner material, which is characterized by the high ductility properties under high-strain-rate loading conditions. The above-mentioned transformation of metallurgical properties of liner material is, however, not a straightforward procedure, since a lot of various requirements have to be met in order to guarantee the high ductility behaviour of the shaped charge jets.

The problem of assessment of the manufactured liner materials with respect to penetration property of shaped charges is also complex due to the fact that many different factors are possible to significantly affect the ductility and fragmentation of jets [1]. Nevertheless, many investigators attempt to formulate a simple method of assessment of some liner materials on the basis of the results obtained with the use of standard material tests. For example, LICHTENBERGER [3] found that, in the case of copper and nickel, the choice of liner material with a low temperature of recrystallization determined using standard hardness measuring guarantees high ductility of a jet. It is a very useful method constituting also a criterion of liner material selection for these types of metals. Unfortunately, for a number of other liner materials, such as, e.g. molybdenum, tantalum or tungsten, Lichtenberger's criterion is not valid. Therefore, various other experimental techniques for materials testing, especially the ones performed at high rates of strain, are commonly used. The split Hopkinson pressure bar is most frequently applied in this type of research [4, 5], however, an expanding ring test is particularly appropriate for the studies of materials ductility [6, 7].

The expanding ring test involves sudden radial acceleration of a ring due to detonation of an explosive charge or electromagnetic loading. The ring rapidly becomes a free-flying body expanding radially and decelerating owing to its own internal circumferential stresses. Measuring the radial displacement $r(t)$ or velocity history $v(t)$ of the ring specimen for the inertial stage of expansion results in the fact that circumferential stress σ_θ and true strain ε_θ for the ring

material are possible to be determined at the imposed strain rate using the following relationships:

$$(1.2) \quad \sigma_{\theta} = -\rho r \frac{\partial^2 r}{\partial t^2},$$

$$(1.3) \quad \varepsilon_{\theta} = \int_{r_0}^r \frac{dr}{r} = \ln \frac{r}{r_0},$$

$$(1.4) \quad \dot{\varepsilon}_{\theta} = \frac{v_r}{r},$$

where ρ – density of ring sample material, r_0 and r – initial and current radius of ring specimen, respectively, v_r – current expansion velocity.

During conducting the research on liners materials, the electromagnetic ring test was originally applied by GOURDIN [8] who suggested that the strain at fracture of specimen rings could be another liner material characteristic, which describes the breakup behaviour of a shaped charge jet. In accordance with the above suggestion, JANISZEWSKI and WŁODARCZYK [9] made also a successful attempt to select liner material built of a copper and its sinters. In this case, however, the dynamic loading of a ring sample resulted from the explosion of a cylindrical explosive charge, on which a ring was directly placed (Fig. 2a). Identification of dynamic properties of tested materials (ductility and fragmentation) desired with regard to the high penetration of shaped charges was performed on the basis of the radiographs taken using the X-ray impulse technique (Fig. 2b).

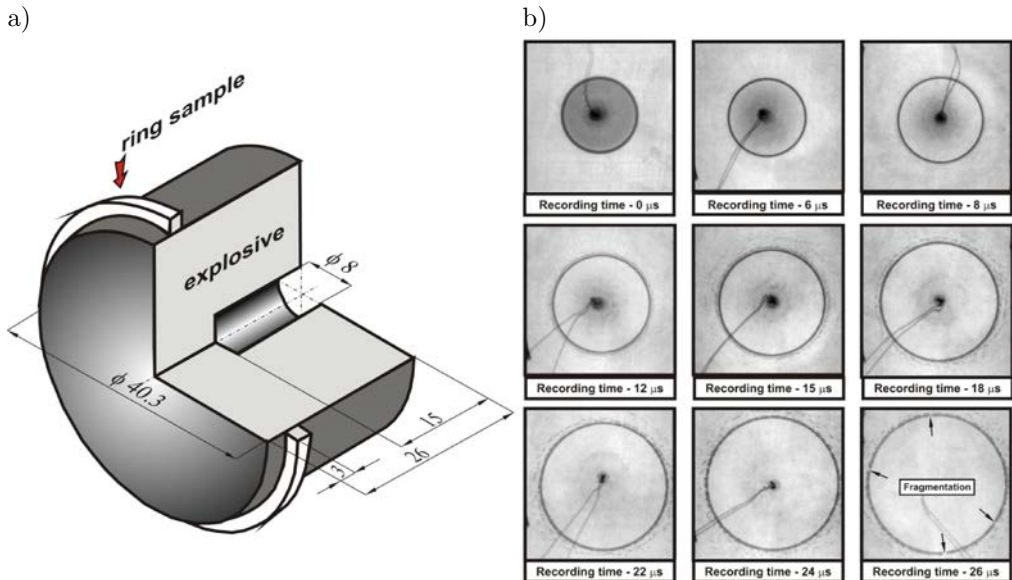


FIG. 2. Scheme of the experimental set-up driving explosively the ring sample (a) and radiographs of explosively expanding rings made of copper sinter (b) [9].

Application of a ring experiment in the liner materials studies results from the fact that the elementary advantage of the ring experiment is that a ring specimen has no boundaries in the primary stress direction and can be stretched uniformly without stress wave effects. Thus, the expanding ring test guarantees model conditions of dynamic experiments. Moreover, with the use of this technique, it is possible not only to achieve strain rates comparable to those occurring in stretching shaped charge jet but also ring specimens can be easily manufactured directly from as-formed liners.

Therefore, it was decided to use the electromagnetic launch ring technique in performing experimental studies for three various sorts of copper in order to identify their ductility properties desired with regard to the high penetration of shaped charges.

The paper is organized as follows: Section 2 is devoted to characterization of material properties of three different sorts of copper specimens and the description of the experimental techniques applied to determine ductility parameters for the tested coppers. The results of the performed experimental tests on ductility of the coppers tested under electromagnetic expansion conditions is described in Sec. 3, whereas the major conclusions of the present work are summarized in Sec. 4.

2. EXPERIMENTAL PROCEDURE

The experimental investigations were carried out on three sorts of copper, i.e. cold-rolled copper Cu-ETP, the annealed at 500°C for 1 hour Cu-ETP copper and the high-purity OFHC copper. In order to provide base-line material properties, the quasi-static material response of selected coppers was characterized in a standard tensile test, hardness measurement and a metallographic study. Material samples for the tensile strength test and electromagnetic ring experiments were machined from the same bar of a 40 mm diameter. The exception is OFHC copper which was prepared from the bar of a 60 mm diameter. The ring samples for electromagnetic expansion were machined to be close to the dimensions used by other investigators [6, 13]. The internal diameter of rings was 31.2 mm, while the cross-sectional area of the rings was 1 mm × 1 mm. In the present investigation, five ring experiments for each sort of a copper specimen were carried out under the given loading conditions. The results presented below are, therefore, the average values from the performed tests. The engineer properties of the studied coppers are collected in Table 1.

In turn, high-strain-rate experiments for the tested coppers were carried out with the use of an electromagnetic ring expansion technique originally proposed by NIORDSON [10]. In accordance with it, a ring specimen made of the tested material is placed concentrically over a mandrel containing a wire coil (Fig. 3).

Table 1. Quasi-static mechanical properties of tested coppers.

Metals	Ultimate tensile strength [MPa]	Yield strength [MPa]	True strain e_f [-]	Uniform strain e_u [-]	Hardness HV1	Grain size [μm]
Cold-rolledCu-ETP	263	239	0.27	0.15	90	25–120
Annealed Cu-ETP	221	77	0.49	0.36	65	20–80
OFHC copper	223	67	0.50	0.33	56	60–180

At the beginning of the experiment, a capacitor bank is charged to high voltage and next rapidly discharged through the wire solenoid and, as a result, the magnetic field is produced around the coil. Simultaneously, this magnetic field induces oppositely directed current in the metal ring specimen which generates the magnetic field as well. As a result of interaction between the magnetic fields originated from the coil and the ring currents, a uniform radial body forces are created. These applied for a very short time forces accelerate the ring specimen to high velocity and next they vanish when the solenoid current drops to a low value. Since that time the ring continues the expansion only by its inertia. If the inertia forces are large enough, the ring is possible to fracture into several small fragments.

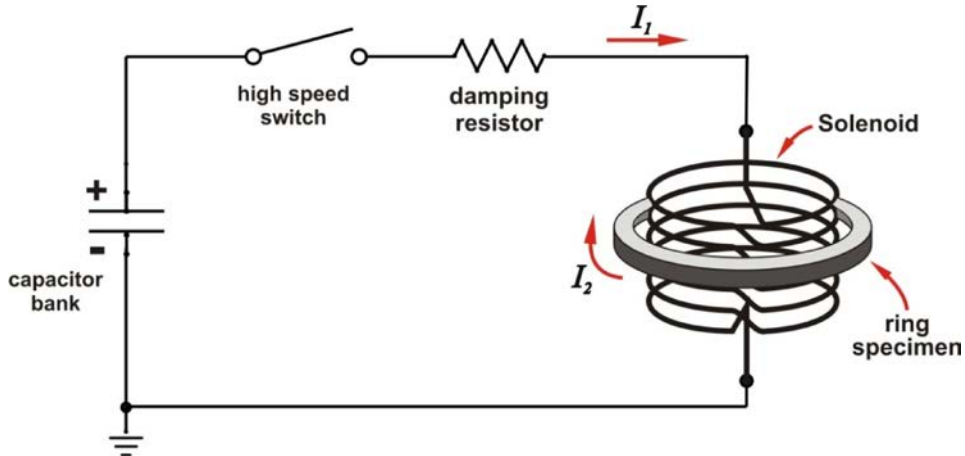


FIG. 3. Schematic diagram of the arrangement for electromagnetic ring expansion.

The above presented idea of radial ring expansion was exploited in the laboratory apparatus developed at Military University of Technology (Fig. 4) [11]. The apparatus consists of three main components: a pulse power system, a loading assembly, and a charging system. Previous experimental studies on copper rings indicate that launching properties of the developed apparatus allowed

rapid acceleration of rings in 35 μs to maximum velocity equal to approximately 300 m/s for 0.91 kJ discharge energy.

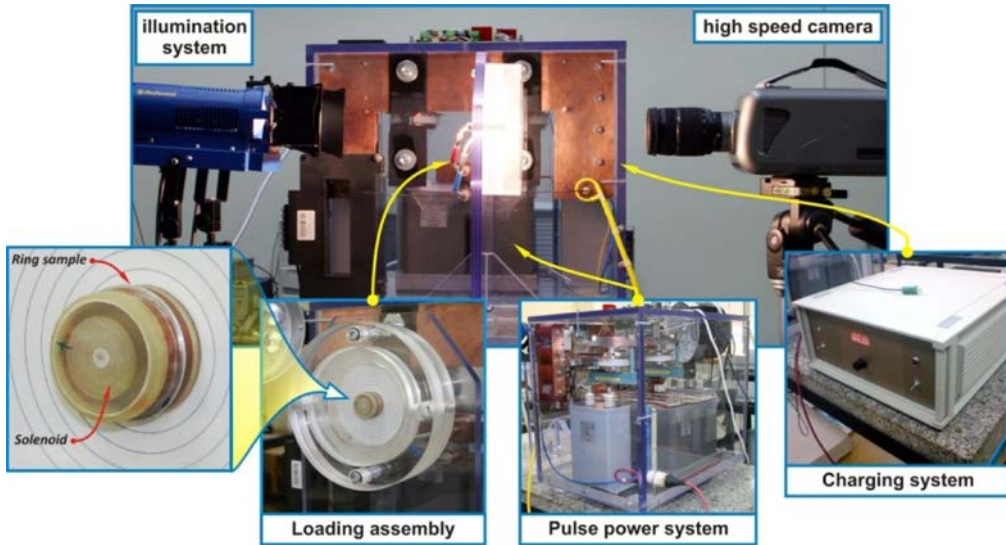


FIG. 4. View of the arrangement for electromagnetic ring experiment.

The displacement of the ring during the expansion process was recorded with a high-speed camera, whereas the ring velocity history was calculated from the high-speed images using the TEMA Automotive software (Fig. 5) [12].

In order to obtain good quality images and to ensure satisfactory measuring accuracy of the ring displacement with the use of an available equipment, first of all, a shadow method of optical observation was applied. This method consists in recording a ring shadow on a highlighted background which is illuminated by Dedocool lighting system (a left side of Fig. 4) allowing concentration of an intense amount of light over a small area. Moreover, the observation field of a high-speed camera was limited to a small area in which there was visible only a moving ring segment and two scaled points (Fig. 5b). Owing to these endeavors and application of the Tema Automotive software, the high measuring accuracy (uncertainty of ± 0.01 mm for the results presented here) and the reliable data concerning the ring expansion history could be obtained.

The expanding ring experiments were performed at similar loading conditions, i.e. maximum expansion velocities involved a range from 171 m/s to 195 m/s, what corresponds to an average strain rate of the order of $8 \times 10^3 \text{ s}^{-1}$. Experiments were carried out under room temperature conditions, i.e. 21°C , however, ring temperature during electromagnetic expansion was increasing in a range from approximately 21°C to 150°C [14].

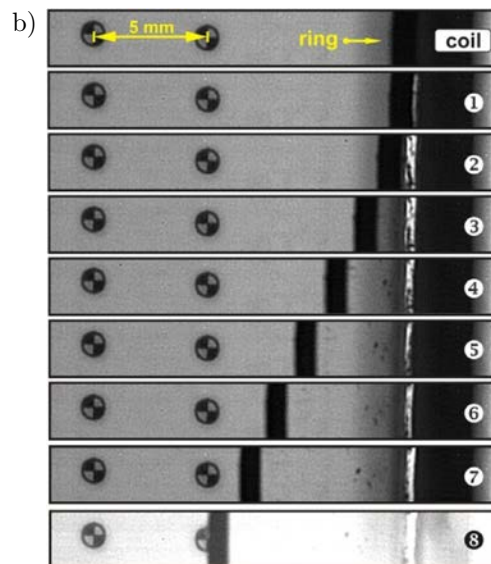
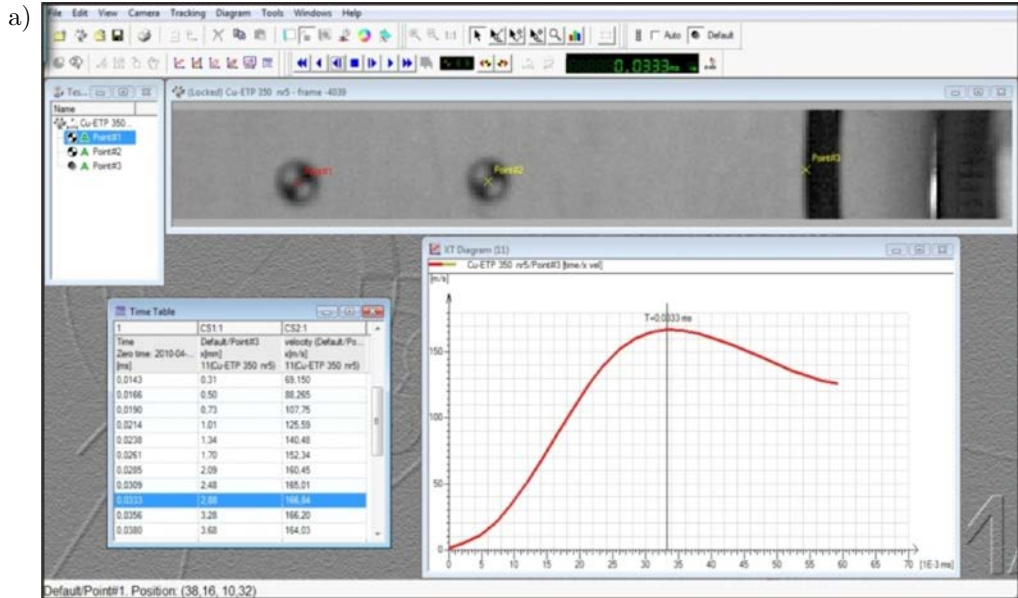


FIG. 5. The example of screen shot of graphical user interface presented video window with the moving ring segment and expansion velocity curve calculated with the use of TEMA Automotive software (a), and the sequence of images showing the observation area with the moving ring segment (b).

Ductility of the studied materials was expressed by uniform strain ε_u and strain at fracture ε_f . The final logarithmic ring strain at failure ε_f was determined on the basis of the data obtained from an optical measuring comparator

by direct measurement of lengths of the recovered fragments captured into the wax ring. On the other hand, uniformed strain ε_u was calculated on the basis of the measurements of cross-sectional dimensions of recovered ring fragments using the following formula:

$$(2.1) \quad \varepsilon_u = \frac{(A_0 - A)}{A},$$

where A_0 and A are the initial and deformed cross-sectional areas, respectively. It should be noted here that a cross-sectional area was determined in the uniform portion of fragments, that is, in the middle of the ring fragment or between neighbouring arrested necks.

3. RESULTS AND DISCUSSION

As it was mentioned earlier, dynamic experiments for all tested copper specimens were carried out for the same discharge energy equal to 0.48 kJ. Nevertheless, the achieved launching velocities were slightly different for each tested sorts of copper rings (Table 2). The highest maximum expansion velocities were reached for the rings made of high-purity OFHC copper, on the other hand, the rings manufactured from cold-rolled Cu-ETP copper were expanded at the lowest velocities. As a consequence, a strain rate also varied in the range from 7.6×10^3 to 9.0×10^3 , which was calculated for strain equal to 0.25 (it is a strain value which corresponds to ring deformation during the inertial stage of ring expansion).

Table 2. Average maximum velocities of expansion of rings made of different sorts of copper.

Ring material	Max. expansion velocity [m/s]	Standard deviation [m/s]	Strain rate for $\varepsilon_\theta = 0.25$ [s ⁻¹]
Cold-rolled Cu-ETP	171	1.9	7.6×10^3
Annealed Cu-ETP	180	2.2	8.2×10^3
High-purity OFHC copper	195	4.6	9.0×10^3

The above-mentioned differences in ring expansion velocities originate from various mechanical responses of the studied copper sorts, what is confirmed by the data presented in Table 3 (the second column from the left). The lowest expansion velocity was achieved for the copper which revealed the highest flow stress (cold-rolled Cu-ETP copper), whereas the highest ring expansion velocity was found for copper with the lowest flow stress value (OFHC copper).

Parameters characterizing ductility and fragmentation properties of the tested materials are collected in Table 3. These parameters allow for concluding gen-

Table 3. Dynamic properties parameters for different sorts of copper.

Ring material	Flow stress σ_θ for $\varepsilon_\theta = 0.25$ [MPa]	Strain at fracture ε_f [-]	Uniform strain ε_u [-]	Average ring fragments length (number) [mm] ([-])
Cold-rolled Cu-ETP	402	0.40	0.31	13.7 (11)
Annealed Cu-ETP	345	0.47	0.49	13.9 (11.5)
High-purity OFHC copper	335	0.43	0.32	14.8 (10.5)

erally that ductility of all copper specimens increases under an electromagnetic ring expansion condition in relation to the static one. Surprisingly, however, the dynamic ductility of OFHC copper is almost at the same level of ductility determined under quasi-static tensile conditions (compare values e_u and ε_u in Table 1 and Table 3). In turn, the highest increase in ductility was found for the cold-rolled ETP copper (increase of 106%), whereas the annealed ETP copper revealed the highest dynamic ductility (the highest values of ε_f and ε_u) in comparison to other sorts of copper.

The high ductility of the annealed ETP copper under ring test conditions is also confirmed by a shape of the recovered ring fragments (Fig. 6). The fragments from the annealed ETP copper rings were the most stretched and they included many small necks so-called arrested necks (Fig. 7). In the case of other copper samples, less number of the arrested necks was observed, especially for OFHC copper. For this type of copper, there was also found the lowest average number of fragments on one ring (10.5) despite of the highest expansion velocity, while an average ring fragments length was the longest and equal to 14.8 mm.

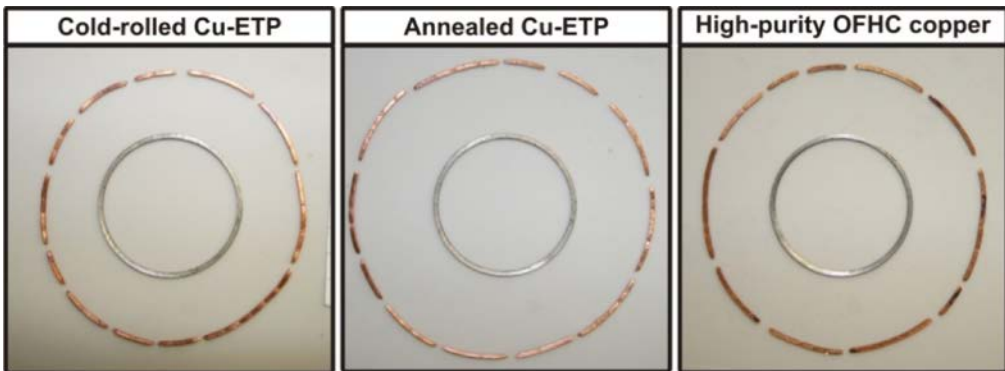


FIG. 6. View of recovered fragments generated from different sorts of copper rings.

The above-presented ductility behaviour of copper rings has been already reported in the literature [6, 15, 16]. Generally, it has been reported on the increase of ductility property of copper under high strain rate tensile conditions

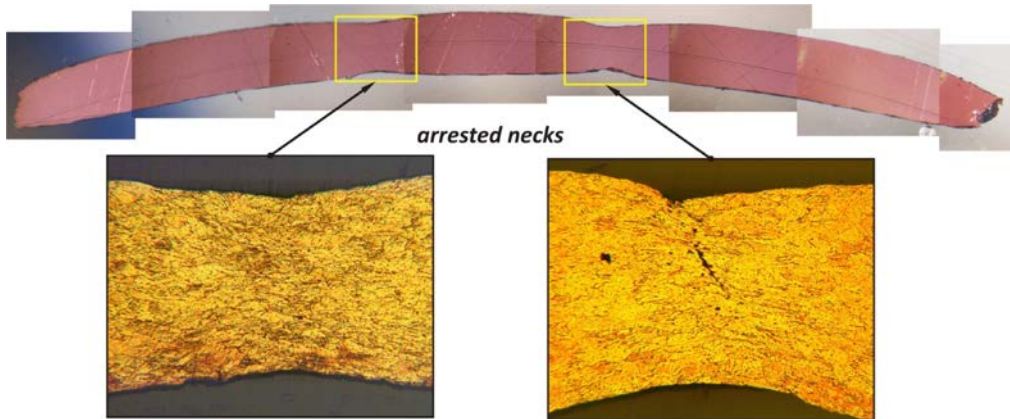


FIG. 7. View of the annealed copper ring fragment and the structures of the arrested necks arisen into ring fragment.

[15, 16] in comparison to the static testing test. There are also scientific reports [6] which present the experimental results demonstrating that the strain at the necking onset of copper rings was nearly equal to the quasi-static necking strain, that is, dynamic copper ductility was at the same level as the ductility determined under a quasi-static tensile test.

The various ductility behaviour of copper may arise from differences in the metallurgical state of the studied copper samples which could have, for example, different grains morphology or a different impurities level. The studied sorts of copper differ from each other in respect to both impurities contents (purity of Cu-ETP – 99.95%; OFHC – 99.99%) and a grains size (see Table 1). In the subject literature, the role of a grain size in ductility behaviour of metals has been especially emphasised [17, 18]. Similarly, the significant influence of a grain size of liner material on ductility of a shaped charge jet has been reported [1–3]. Generally, it was stated that with decreasing of a grain size of a copper liner, jet ductility was increased, and thus penetration of a jet was also improved. The results of the experiments performed with the use of an expanding ring technique confirmed the above-mentioned relation between a grain size of copper samples and their ductility under a high rate of strain since the highest ductility revealed the annealed copper Cu-ETP, which had got the smallest grain size (20–80 μm). Thus, it can be believed that the application of this sort of copper as the liner material ensures the high penetration capability of a shaped charge jet.

4. CONCLUSIONS

In the present work, the electromagnetic ring test was applied in order to select shaped charge liner material from among three sorts of copper. In ac-

cordance with the data presented in the literature [1–3, 8, 17, 18], the obtained results show that the copper with the smallest grain size (the annealed Cu-ETP) reveals the highest ductility under electromagnetic expanding ring loading conditions. Taking the above mentioned problems into consideration, it may be concluded that the observations carried out in the present work constitute another proof that the electromagnetic ring test is a good tool for the choice of liner materials.

REFERENCES

1. WALTERS W.P., ZUKAS J.A., *Fundamentals of shaped charges*, John Wiley and Sons, New York – Chichester – Brisbane – Toronto – Singapore, 1989.
2. LICHTENBERGER A., *Ductile behavior of some materials in the shaped charge jet*, [in:] Metallurgical and Materials Applications of Shock-Wave and High-Strain-Rate Phenomena, L.E. Murr, K.P. Staudhammer, M.A. Meyers [Eds.], Elsevier Science B.V., 1995.
3. LICHTENBERGER A., *Some criteria for choice of shaped charge copper liners*, 11th International Symposium on Ballistics, Brussels, Belgium, 1989.
4. CHEN W., SONG B., *Split Hopkinson (Kolsky) Bar: Design, Testing and Applications*, Springer, New York – Dordrecht – Heidelberg – London, 2010.
5. KLEPACZKO J., *Introduction to experimental techniques for materials testing at high strain rates*, Institute of Aviation Scientific Publications Group, Warszawa, 2007.
6. ZHANG H., RAVI-CHANDAR K., *On the dynamics of necking and fragmentation – I. Real-time and post-mortem observations in Al 6061-O*, Int. J. Fract., **142**, 183–217, 2006.
7. RUSINEK A., ZAERA R., *Finite element simulation of steel ring fragmentation under radial expansion*, International Journal of Impact Engineering, **34**, 2007.
8. GOURDIN W.H., *Correlation between the ultimate elongations of rapidly expanding rings and stretching metal jets*, [in:] Shock-Wave and High-Strain-Rate Phenomena, L.E. Murr, K.P. Staudhammer, M.A. Meyers [Eds.], Marcel Dekker, Inc., pp. 611–616, 1992.
9. JANISZEWSKI J., WŁODARCZYK E., *Static and dynamic ductility of copper and its sinters*, Journal of Technical Physics, **45**, 4, 263–274, 2004.
10. NIORDSON F.I., *A unit for testing Materials at High Strain Rates*, Experimental Mechanics, January, 1965.
11. JANISZEWSKI J., PICHOLA W., *Development of Electromagnetic Ring Expansion Apparatus for High-Strain-Rate Test*, Solid State Phenomena, **147-149**, 645–650, 2009.
12. <http://www.dedolight.com> (July 2012).
13. GOURDIN W.H., *Analysis and assessment of electromagnetic ring expansion as a high-strain-rate test*, J. Appl. Phys., **65**, 2, 411–422, 1989.
14. JANISZEWSKI J., PANOWICZ R., *Numerical analysis of electromagnetic expansion process for thin-walled copper ring* [in Polish], Electrical Review (Przegląd Elektrotechniczny), **88**, 7a, 270–276, 2012.
15. ALTYNOVA M., HU X., DAEHN G.S., *Increased ductility in high velocity electromagnetic ring expansion*, Metall Mater Trans A, **27A**, 1837–1844, 1996.

16. JANISZEWSKI J., *Ductility of selected metals under electromagnetic ring test loading conditions*, International Journal of Solids and Structures, **49**, 1001–1008, 2012.
17. CHOKSHI A.H., MAYERS M.A., *The prospects for superplasticity at high strain rates: preliminary considerations and an example*, Scripta Metallurgica et Materialia, **24**, 605–610, 1990.
18. REGAZZONI G., MONTHEILLET F., *High strain rate ductility in uniaxial tension: A review*, Journal de Physique, Colloque C5, suppl., **46**, 8, 435–443, 1985.

Received May 25, 2012; revised version November 27, 2012.

Influence of Failure Strain of Different Aluminium Alloys on Dynamic Problems

Marcos RODRIGUEZ-MILLÁN¹⁾, Álvaro VAZ-ROMERO¹⁾,
José Antonio RODRIGUEZ-MARTINEZ¹⁾, Alexis RUSINEK²⁾,
Ángel ARIAS¹⁾

¹⁾ *University Carlos III of Madrid*
Department of Continuum Mechanics and Structural Analysis
Avda. De la Universidad 30, 28911 Leganés, Madrid, Spain
e-mail: mrmillan@ing.uc3m.es

²⁾ *National Engineering School of Metz (ENIM)*
Laboratory of Mechanic, Biomechanic, Polymers and Structures (LaBPS)
1 route d'Ars Laquenexy, 57078 Metz Cedex 3, France

In this work an experimental-numerical methodology is devised for analyzing ductile fracture of two aluminum alloys under different values of stress triaxiality ($0.2 \leq \eta \leq 1.2$) and Lode parameter ($-1 \leq \mu \leq 0$). The experiments developed include combined loading (tension-torsion) tests on same NT specimen geometry for A 5754-H111 and AA 6082-T6. Numerical analysis shows that this type of specimen exhibits uniformity stable values of stress triaxiality and Lode parameter as plastic strain develops. Experimental results can be used to compare failure strain corresponding to different stress states. Moreover, to consider the influence of stress state in failure mechanics under impact loads, perforation tests of aluminum alloys have been developed in a range of impact velocity between $120 \leq v \leq 500$ m/s. The tests were carried out with three different shape projectiles: conical ($m = 29.4$ g) and two blunt ones ($m = 29.4$ g and $m = 1.1$ g). Results show the dependence on energy absorption with stress state and failure strain.

Key words: ductile failure, stress triaxiality, Lode parameter, aluminum, perforation.

1. INTRODUCTION

Aluminium alloys are used in numerous engineering fields like aeronautical, naval of automotive industry. A desirable requirement for an optimal design is mainly a high capacity for energy absorption in high loading rate events and a reducing of weight.

For a reliable prediction of the structural element behaviour and its energy absorption capacity until breakage, the numerical tools have to consider failure

criteria for the material. The simulation of such structures subjected to impact loads requires suitable constitutive laws capable of reproducing the material behaviour and representative failure models in the extreme conditions to which the component is subjected.

Pioneer works of MCCLINTOCK [1] and subsequently RICE and TRACEY [2] firstly introduced an important parameter, stress triaxiality η , which is defined as the ratio of hydrostatic pressure to Von Misses equivalent stress σ_e , Eq. (1.1).

$$(1.1) \quad \eta = \frac{\frac{1}{3}(\sigma_1 + \sigma_2 + \sigma_3)}{\sigma_e}.$$

A few years ago, several researchers [3, 4] have shown that the stress triaxiality alone is not sufficient to describe properly the behavior of the material at failure. Hence, the model developed by XUE and WIERZBICKI [5] considers the effect of the third stress invariant. The Lode parameter plays the role of third stress invariant, Eq. (1.2).

$$(1.2) \quad \mu = \frac{2\sigma_2 - \sigma_1 - \sigma_3}{\sigma_1 - \sigma_3}.$$

Recently, other fracture criterion has been proposed by STOUGHTON and YOON [6]. This criterion considers that fracture occurrence is predicted by the magnitude of maximum shear stress, although the influence of hydrostatic pressure is not considered in this one. In this regard, adequate damage models relate failure strain to stress triaxiality and Lode parameter. In general, calibration of these models has traditionally relied on specimens that exhibit high triaxiality and limited Lode parameter. This work presents a procedure that combines tension and torsion to achieve values of stress triaxiality ($0.2 \leq \eta \leq 1.2$) and Lode parameter in the following range: $-1 \leq \mu \leq 0$. The existence of different stress states and failure modes is characteristic of dynamic process like collision events or perforation processes. In order to consider the influence of triaxiality and Lode parameter in those processes, perforation tests have been carried out in this work. Different shapes of projectile that modify the failure mode have been used.

2. COMBINED TENSION (COMPRESSION)-TORSION TEST

2.1. Procedure

Experimental tests were performed on circumferentially double notched tube specimen [4], Fig. 1. Tests were carried out in an universal servo-hydraulic machine which was adapted for this investigation, Fig. 2. This machine allows getting axial and torsional maximum values of 25 kN and 900 Nm, respectively. Tests were registered by Axial/Torsional Extensometer and optical camera.

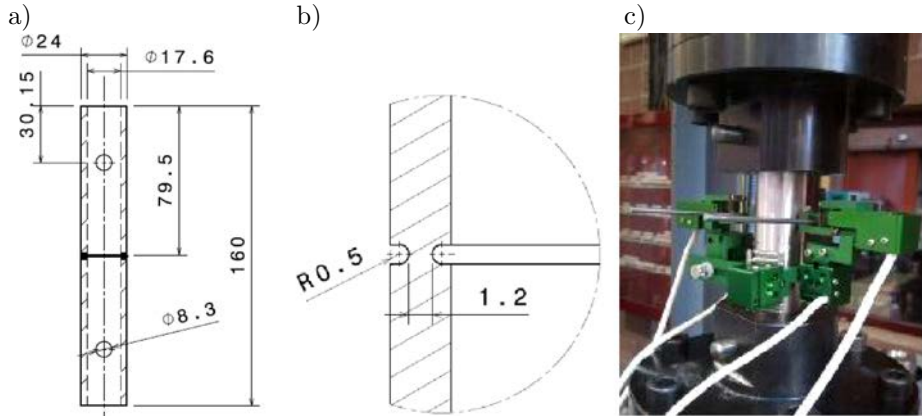


FIG. 1. a) Configuration of double notched tube specimen and b) zoom of the notch, c) Axial/Torsional Extensometer.

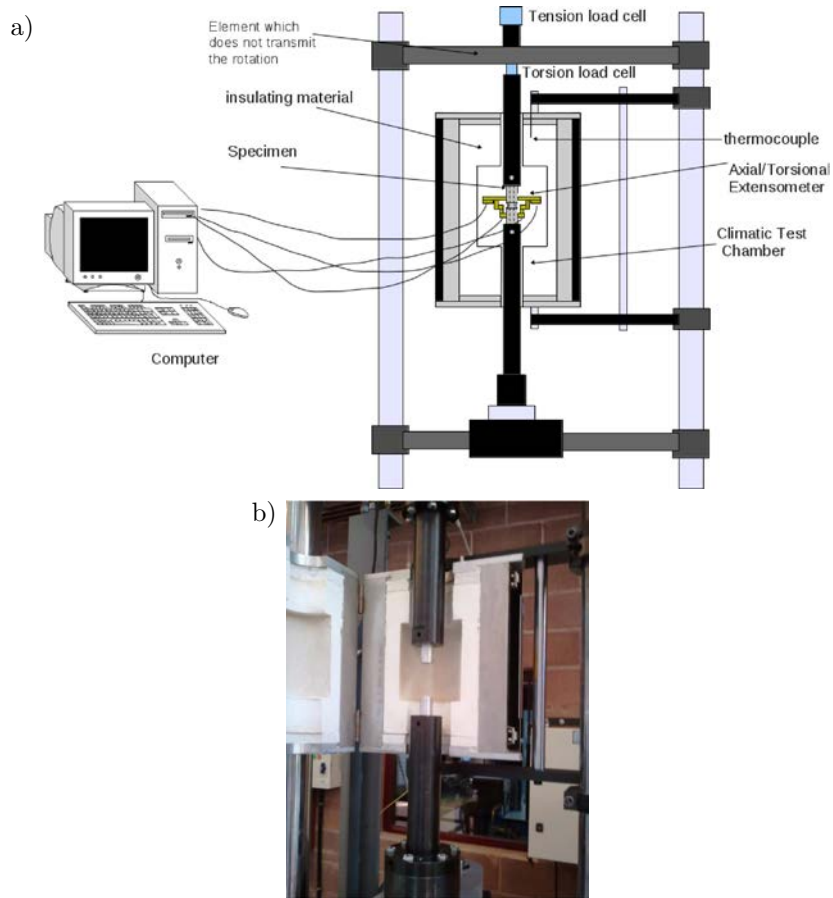


FIG. 2. a) Illustration of experimental machine, b) experimental universal servo-hydraulic machine.

The specimen is subjected to a combination of tensile and torsional loading using a load ratio parameter, κ , which is constant during the test, Eq. (2.1).

$$(2.1) \quad \kappa = \frac{\sigma_n}{\tau_n} = \frac{N \cdot r_m}{M},$$

where N is the axial force, M is the torsional moment and r_m is the value of radius to the centre of the notch.

A combined experimental-numerical methodology for analysing the influence of stress state in strain failure in the low to intermediate stress triaxiality regime has been implemented (Fig. 3). Main steps are:

- Procurement of load-displacement curves outside the notched zone by several experimental tests.
- Processing all tests using a two-dimensional (2D) model in finite element program ABAQUS, Figs. 4, 5.
- Determination and comparison the average effective strain. Experimental data results validate numerical simulations, Fig. 6.

Thus, stress and strain values calculated from simulations can be used to obtain the equivalent plastic failure strain and the stress triaxiality and Lode parameter.

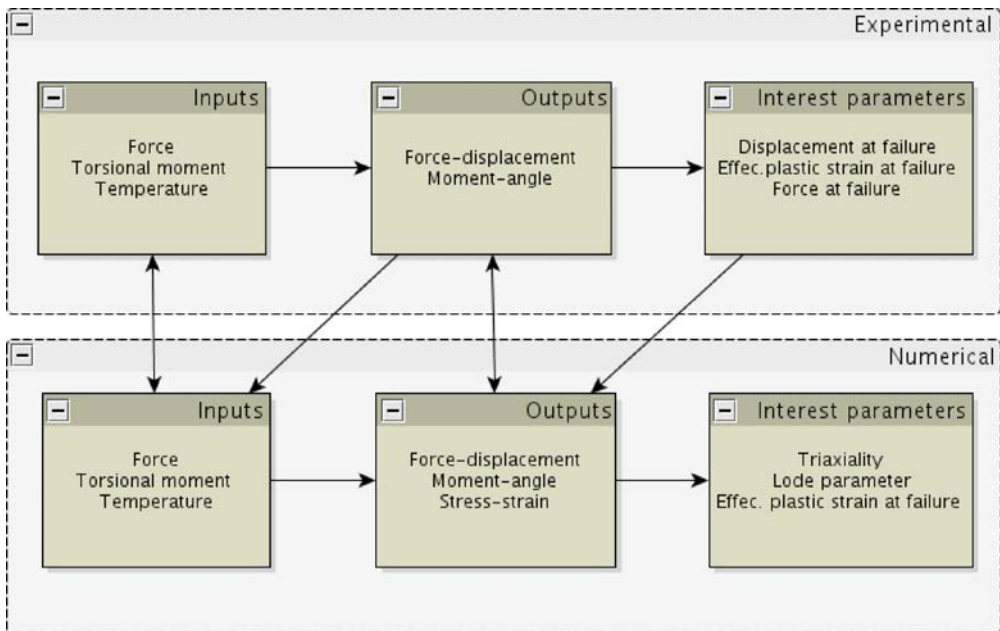


FIG. 3. Schematic methodology in order to perform combined tension-torsion tests.

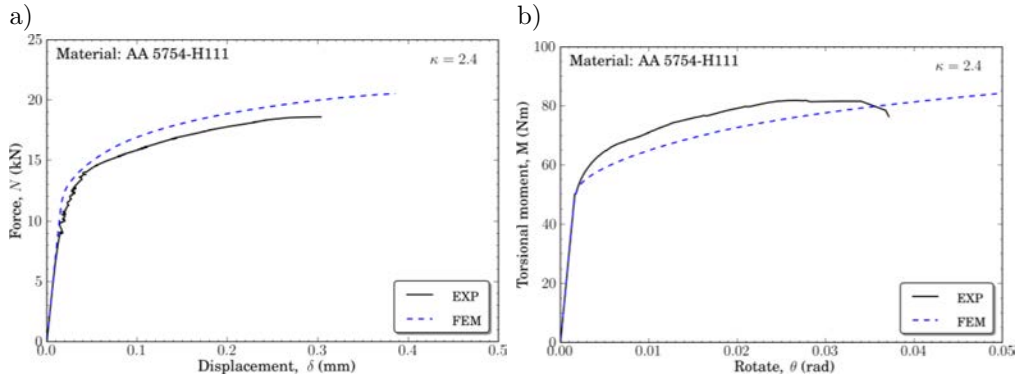


FIG. 4. Comparison between finite element simulations and experimental results for the aluminium 5754-H111 and $\kappa = 2.4$: a) axial force *versus* axial displacement, b) torsional moment *versus* angle rotation.

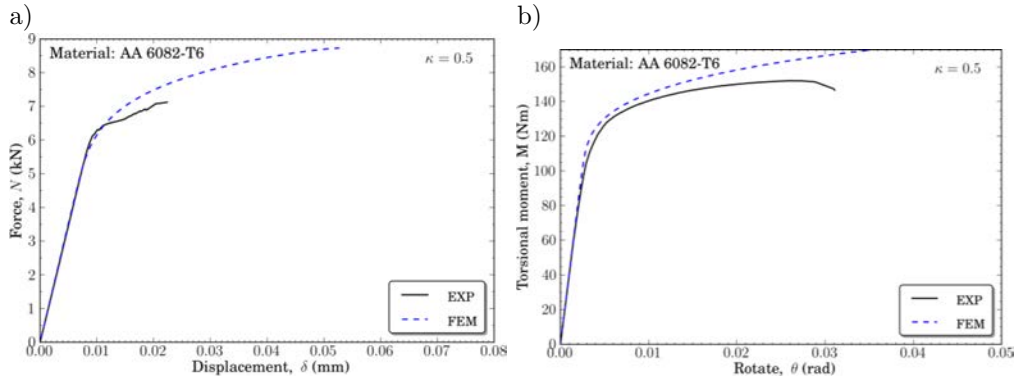


FIG. 5. Comparison between finite element simulations and experimental results for the aluminium 6082-T6 and $\kappa = 0.5$: a) axial force *versus* axial displacement, b) torsional moment *versus* angle rotation.

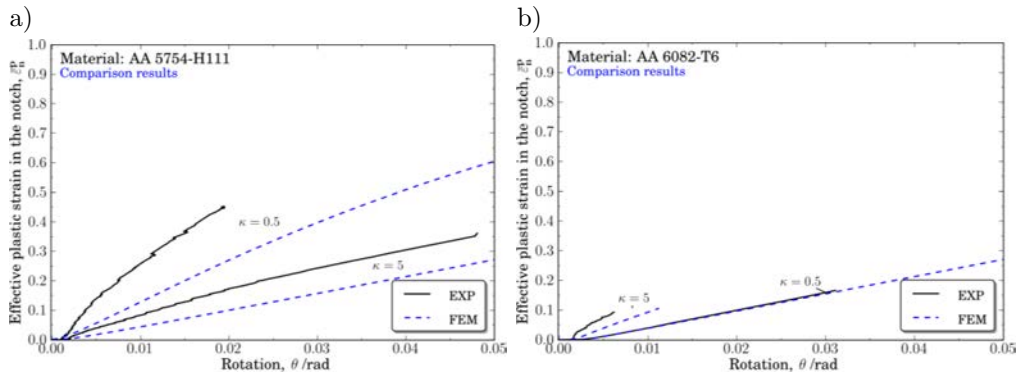


FIG. 6. Comparison between finite element simulations and experimental results. Effective plastic strain *versus* rotation for: a) the aluminium 5754-H111 and b) the aluminium 6082-T6.

3. RESULT ANALYSIS

From finite element simulations, the range in stress triaxiality is examined using the load ratio which varied from pure shear ($\kappa = 0$) to pure tension ($\kappa = \infty$). The maximum stress triaxiality value achievable is within the range $0.9 \leq \eta \leq 1.22$, Fig. 7a. The dependence of Lode parameter with respect to the stress triaxiality is illustrated in Fig. 7b. Data shows three distinct regions corresponding to different stress states: at low and high stress triaxiality, the stress state is approached to generalized shear ($\mu \rightarrow 0$) and between them the stress state is approached to generalized tension ($\mu \rightarrow -1$). The numerical analyses of the specimen show stable values of triaxiality and Lode parameter during the load history which is a desirable characteristic before failure, Fig. 7c.

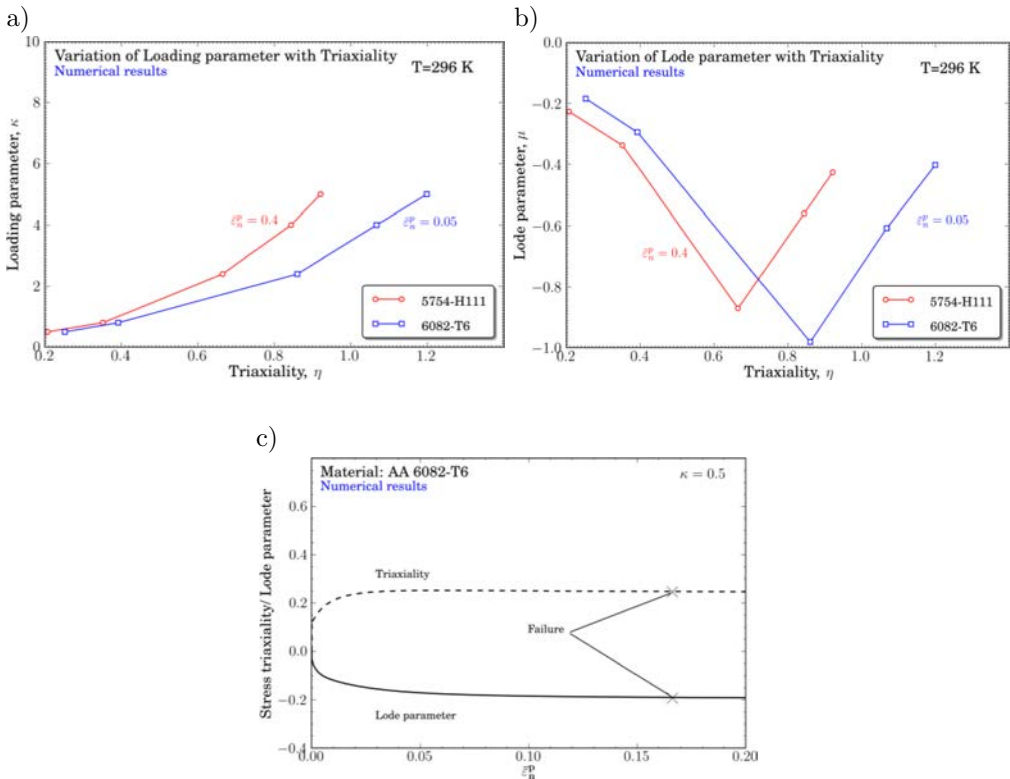


FIG. 7. a) Curve of Load parameter with stress triaxiality, b) comparison of Lode parameter and stress triaxiality over the range of applied loading conditions, c) evolution of stress triaxiality and Lode parameter in the centre of the notch.

The spatial variation of stress triaxiality, Lode parameter and the effective plastic strain is examined in Fig. 8b. The failure is marked by a sudden load

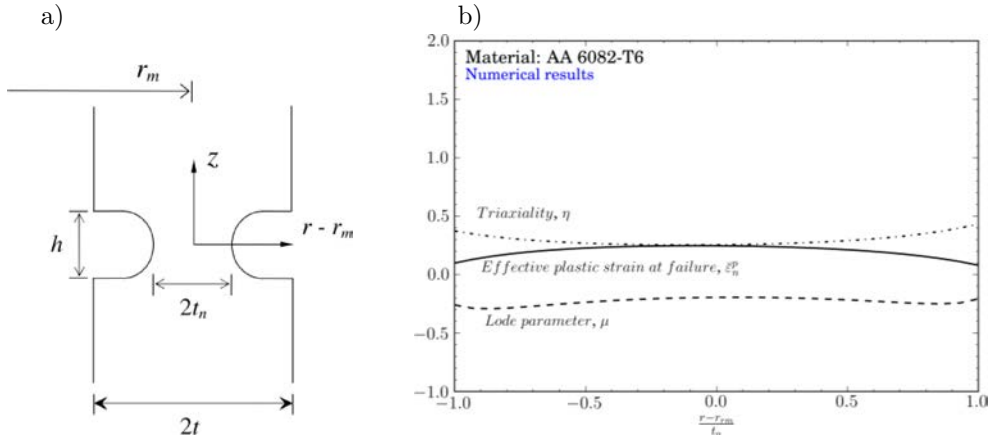


FIG. 8. Axisymmetric cut of notch (a) and b) through-thickness distribution of stress triaxiality, Lode parameter and effective plastic strain at the mid-section of the specimen.

drop which it is assumed in the centre portion of notch. In this regard, these parameters are explored in the symmetry plane ($z = 0$) according to Fig. 8a.

A comparison of effective plastic strain at failure *versus* stress triaxiality and Lode parameter between aluminium alloys AA 5754-H111 and AA 6082-T6 is shown in Table 1. Data show a dependence on failure strain and stress triaxiality, η , and Lode parameter, μ .

Table 1. Value of effective plastic strain at failure, stress triaxiality η , and Lode parameter, μ , for AA 5754-H111 and AA 6082-T6.

	AA 5754-H111		AA 6082-T6	
	$\kappa = 0.5$	$\kappa = 5$	$\kappa = 0.5$	$\kappa = 5$
$\bar{\epsilon}_p^f$	0.361	0.452	0.166	0.092
η	0.206	0.916	0.246	1.187
μ	-0.222	-0.405	-0.193	-0.377

To consider the influence of stress state in failure modes of dynamic processes, perforation tests have been performed.

4. PERFORATION PROCESS OF ALUMINIUM PLATES

An analysis of ductile failure mechanics has been developed on AA 5754-H111 and AA 6082-T6 plates using three different projectiles: one conical ($m_c = 29.4$ g) and two blunt ones ($m_{b1} = 29.4$ g and $m_{b2} = 1.1$ g). In total, 20 tests were performed.

Figure 9 shows energy absorbed by the plate as a function of the impact velocity. As is generally known, the projectile shape is an important param-

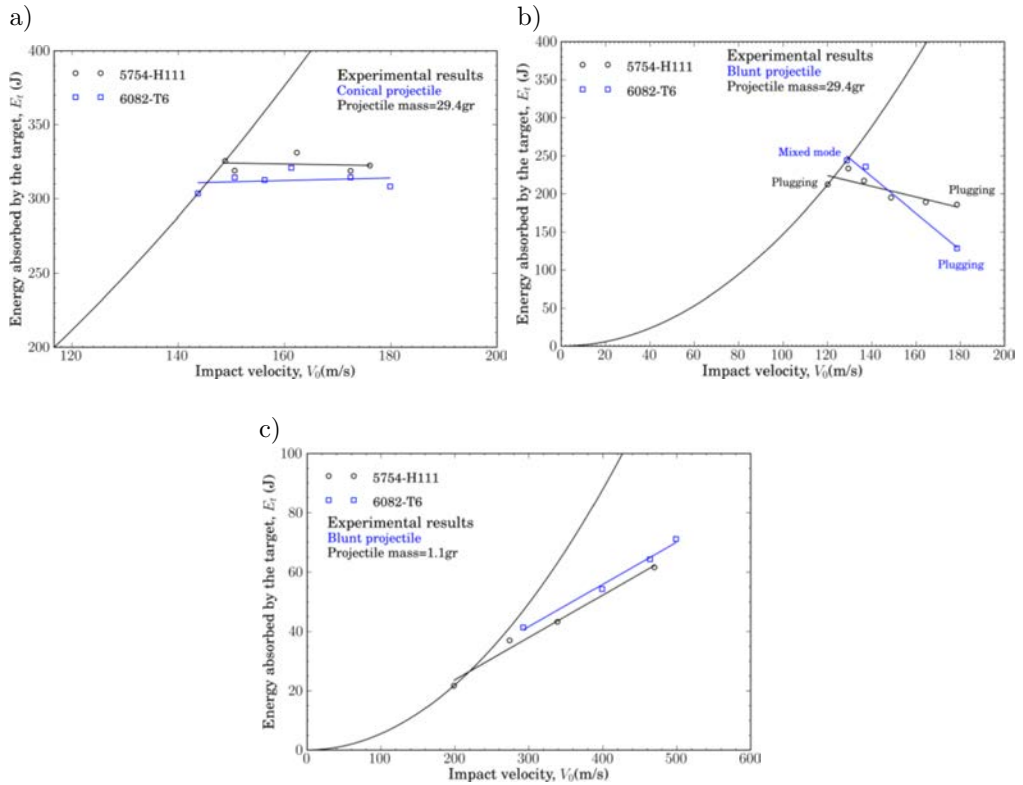


FIG. 9. Energy absorbed vs. impact velocity with a) conical ($m = 29.4$ g), b) blunt ($m = 29.4$ g) and c) blunt ($m = 1.1$ g) projectile

ter in the perforation behaviour of the plate. The experiments performed with same conical projectile and mass ($m = 29.4$ g) revealed that energy absorption is approximately constant, Fig. 9a. In this case, petalling failure mechanics is produced by high radial and circumferential tensile stress. As a result, the tests revealed that for both aluminium alloys the energy absorption capacity was similar. This result is coherent with failure strain value obtained for these materials, Table 2.

Table 2. Value of tensile and shear strain for AA 5754-H111 and AA 6082-T6.

	AA 5754-H111	AA 6082-T6
ε_f	0.172	0.170
γ_f	0.379	0.32

However, it can be observed a significant decreasing in energy absorption with the increase of impact velocity when a blunt projectile is used, Fig. 9b.

Moreover, the perforation mechanics was markedly different. Plugging failure is due to adiabatic shearing. AA 6082-T6 shows less energy absorption ($E_a = 120$ J) than AA 5754-H111 ($E_a = 200$ J), according to failure shear strain values in Table 2. This behaviour can be explained by the more sensibility of AA 6082-T6 to localize plastic deformation in conditions of low stress triaxiality and consequently the minor plastic work developed for plate explain of decreased absorption energy. Experimental data obtained (Table 1) show minor value of failure strain of AA 6082-T6 at low values of κ (*shear states*). Moreover, the impact experiments were carried out with another mass projectile and same blunt shape, in order to compare the energy absorption, Fig. 9c.

5. CONCLUSIONS AND REMARKS

In this work, a procedure for estimation of the effective plastic strain and characterization of stress state at failure has been developed. The methodology allows a control of stress triaxiality and Lode parameter by a fixed loading ratio. In addition, for considered aluminum alloys, the effect of stress state on failure strain and energy absorption has been evaluated on perforation tests.

REFERENCES

1. MCCLINTOCK F.A., *A Criterion for Ductile Fracture by the Growth of Holes*, Journal of Applied Mechanics, **35**, 363–371, 1968.
2. RICE J.R., TRACEY D.M., *On the Ductile Enlargement of Voids in Triaxial Stress Fields*, Journal of the Mechanics of Physical Solids, **17**, 201–217, 1969.
3. BAO Y., WIERZBICKI T., *On Fracture Locus in the Equivalent Strain and Stress Triaxiality Space*, International Journal of Mechanical Sciences, **46**, 81–98, 2004.
4. BARSOU M., FALESKOG J., *Rupture Mechanisms in Combined Tension and Shear – Experiments*, International Journal of Solids and Structures, **44**, 1768–1786, 2007.
5. XUE L., WIERZBICKI T., *Ductile fracture initiation and propagation modeling using damage plasticity theory*, Engineering Fracture Mechanics, **75**, 11, 3276–3293, 2008
6. STOUGHTON T.B., YOON J.W., *A new approach for failure criterion for sheet metals*, International Journal of Plasticity, **27**, 3, 440–459, 2011.

Received May 25, 2012; revised version October 9, 2012.

A Characterization of the Rivlin-Ericksen Viscoelastic Fluid in the Presence of a Magnetic Field and Rotation

Ajaib S. BANYAL

Department of Mathematics, Govt. College Nadaun, Hamirpur
(HP) India 177033
e-mail: ajaibbanyal@rediffmail.com

A layer of Rivlin-Ericksen viscoelastic fluid heated from below is considered in the presence of an uniform vertical magnetic field and rotation. Following the linearized stability theory and normal mode analysis, this paper mathematically establishes the condition for characterizing oscillatory motion, which may be neutral or unstable, for rigid boundaries at the top and bottom of the fluid. It is established that all non-decaying slow motions starting from rest, in the configurations, are necessarily non-oscillatory in the regime

$$\frac{T_A F}{\pi^2} + \frac{T_A}{\pi^4} + \frac{Q p_2}{\pi^2} \leq 1,$$

where T_A is the Taylor number, Q is the Chandrasekhar number, p_2 is the magnetic Prandtl number, and F is the viscoelasticity parameter. This result is important, since it holds for all wave numbers for rigid boundaries of infinite horizontal extension at the top and bottom of the fluid, and the exact solutions of the problem investigated in closed form are not obtainable.

Key words: thermal convection, Rivlin-Ericksen fluid, rotation, magnetic field PES, Rayleigh number, Chandrasekhar number, Taylor number.

MSC 2000 No.: 76A05, 76E06, 76E15, 76E07, 76U05.

NOTATIONS

- a – dimensionless wave number,
- F – viscoelasticity parameter,
- g – acceleration due to gravity [m/s^2],
- k – wave number [$1/\text{m}$],
- k_x, k_y – wave numbers in x - and y -directions [$1/\text{m}$],
- n – growth rate [$1/\text{s}$],
- Q – Chandrasekhar number,
- T_A – Taylor number,
- R – Rayleigh number,
- $\boldsymbol{\Omega}(0, 0, \Omega)$ – rotation vector having components $(0, 0, \Omega)$,
- $\mathbf{H}(h_x, h_y, h_z)$ – magnetic field having components (h_x, h_y, h_z) ,

- T – temperature [K],
 $\mathbf{q}(u, v, w)$ – components of velocity after perturbation,
 p_1 – thermal Prandtl number,
 p_2 – magnetic Prandtl number,
 α – coefficient of thermal expansion [1/K],
 β – uniform temperature gradient [K/m],
 Θ – perturbation in temperature [K],
 κ – thermal diffusivity [m^2/s],
 ν – kinematic viscosity [m^2/s],
 ν' – kinematic viscoelasticity [m^2/s],
 ∇, ∂, D – Del operator, Curly operator and Derivative with respect to z ($= d/dz$).

1. INTRODUCTION

The stability of a dynamical system is close to real life in the sense that the realization of a dynamical system depends upon its stability. Right from the conceptualization of turbulence, the instability of fluid flow is regarded as being at its root. The thermal instability of a fluid layer with maintained adverse temperature gradient by heating the underside, plays an important role in Geophysics, interiors of the Earth, Oceanography, and Atmospheric Physics; and has been investigated by several authors under different conditions (e.g., BÉNARD [1], RAYLEIGH [2], and JEFFREYS [3]). A detailed account of the theoretical and experimental study of the onset of Bénard Convection in Newtonian fluids, under various assumptions of hydrodynamics and hydromagnetics, has been given by CHANDRASEKHAR [4]. The use of Boussinesq's approximation has been made throughout, which states that density changes are disregarded in all terms in the equations of motion except the external force term. BHATIA and STEINER [5] have considered the affect of uniform rotation on the thermal instability of a viscoelastic (Maxwell) fluid and found that rotation has a destabilizing influence in contrast to the stabilizing affect on Newtonian fluids. The thermal instability of a Maxwell fluid in hydromagnetics has been studied by BHATIA and STEINER [6]. They found that the magnetic field stabilizes a viscoelastic (Maxwell) fluid, just as it stabilizes a Newtonian fluid. SHARMA [7] studied the thermal instability of a layer of viscoelastic (Oldroydian) fluid acted upon by a uniform rotation and found that rotation has a destabilizing as well as a stabilizing effect under certain conditions, in contrast to that of a Maxwell fluid where it has a destabilizing effect. In another study, SHARMA [8] has considered the stability of a layer of an electrically conducting OLDROYD fluid [9] in the presence of magnetic field and found that the magnetic field has a stabilizing influence.

There are many viscoelastic fluids that cannot be characterized by Maxwell's constitutive relations, nor by OLDROYD'S [9] constitutive relations. Two such

classes of fluids are Rivlin-Ericksen's and Walter's (model B') fluids. RIVLIN-ERICKSEN [10] has proposed a theoretical model for one such class of elastic-viscous fluids. SHARMA and KUMAR [11] have studied the affect of rotation on thermal instability in a Rivlin-Ericksen elastico-viscous fluid and found that rotation has a stabilizing effect and introduces oscillatory modes in the system. KUMAR *et al.* [12] considered the affect of rotation and magnetic field on a Rivlin-Ericksen viscoelastic fluid and found that rotation has a stabilizing effect, whereas the magnetic field has both stabilizing and destabilizing effects. A layer of such fluid heated from below or under the action of either a magnetic field or rotation, or both, may find applications in Geophysics, interior of the Earth, Oceanography, and Atmospheric Physics.

PELLOW and SOUTHWELL [13] proved the validity of the 'Principle of Exchange of Stability' (PES) for the classical Rayleigh-Bénard convection problem. BANERJEE *et al.* [14] gave a new scheme for combining the governing equations of thermohaline convection, which was shown to lead to bounds for the complex growth rate of arbitrary oscillatory perturbations, neutral or unstable, for all combinations of dynamically rigid or free boundaries. BANERJEE and BANERJEE [15] established a criterion for the characterization of non-oscillatory motions in hydrodynamics, which was further extended by GUPTA *et al.* [16]. However, no such result exists for non-Newtonian fluid configurations in general and for Rivlin-Ericksen viscoelastic fluid configurations in particular. BANYAL [17] have characterized the non-oscillatory motions in coupled-stress fluids.

Keeping in mind the importance of Rivlin-Ericksen viscoelastic fluids, this paper is an attempt to study a Rivlin-Ericksen viscoelastic fluid heated from below in the presence of a uniform vertical magnetic field and rotation. It is established that the onset of instability in a Rivlin-Ericksen viscoelastic fluid in the present configuration cannot manifest itself as oscillatory motion of growing amplitude if the Taylor number T_A , the Chandrasekhar number Q , the magnetic Prandtl number p_2 , and the viscoelasticity parameter F , together satisfy the inequality $\frac{T_A F}{\pi^2} + \frac{T_A}{\pi^4} + \frac{Q p_2}{\pi^2} \leq 1$. These results hold for all wave numbers with rigid boundaries of infinite horizontal extension at the top and bottom of the fluid.

2. FORMULATION OF THE PROBLEM AND PERTURBATION EQUATIONS

Consider an infinite, horizontal, incompressible, electrically conducting, Rivlin-Ericksen viscoelastic fluid layer of thickness d , heated from below such that the temperature and density on the bottom surface $z = 0$ are T_0 and ρ_0 , and on the upper surface $z = d$ are T_d and ρ_d respectively, and that a uniform adverse temperature gradient $\beta \left(= \left| \frac{dT}{dz} \right| \right)$ is maintained. The fluid is acted upon

by a uniform vertical rotation $\boldsymbol{\Omega}(0, 0, \Omega)$ and a uniform vertical magnetic field $\mathbf{H}(0, 0, H)$.

The equations of motion, continuity, heat conduction, and Maxwell's equations governing the flow of Rivlin-Ericksen viscoelastic fluid in the presence of magnetic field and rotation (RIVLIN and ERICKSEN [10]; CHANDRASEKHAR [4], and KUMAR *et al.* [12]) are:

$$(2.1) \quad \frac{\partial \mathbf{q}}{\partial t} + (\mathbf{q} \cdot \nabla) \mathbf{q} = -\nabla \left(\frac{p}{\rho_0} - \frac{1}{2} |\boldsymbol{\Omega} \times \mathbf{r}|^2 \right) + \mathbf{g} \left(1 + \frac{\delta \rho}{\rho_0} \right) \\ + \left(\nu + \nu' \frac{\partial}{\partial t} \right) \nabla^2 \mathbf{q} + \frac{\mu_e}{4\pi \rho_0} (\nabla \times \mathbf{H}) \times \mathbf{H} + 2(\mathbf{q} \times \boldsymbol{\Omega}),$$

$$(2.2) \quad \nabla \cdot \mathbf{q} = 0,$$

$$(2.3) \quad \frac{\partial T}{\partial t} + (\mathbf{q} \cdot \nabla) T = \kappa \nabla^2 T,$$

$$(2.4) \quad \nabla \cdot \mathbf{H} = 0,$$

$$(2.5) \quad \frac{\partial \mathbf{H}}{\partial t} = (\mathbf{H} \cdot \nabla) \mathbf{q} + \eta \nabla^2 \mathbf{H}.$$

The equation of state for the fluid is

$$(2.6) \quad \rho = \rho_0 [1 - \alpha(T - T_0)],$$

where ρ , p , T , ν , ν' , and $\mathbf{q}(u, v, w)$ denote the density, pressure, temperature, kinematic viscosity, kinematic viscoelasticity, and velocity of the fluid respectively. Furthermore, $\mathbf{r}(x, y, z)$ and the suffix zero refers to values at the reference level $z = 0$. Here, $\mathbf{g}(0, 0, -g)$ is the acceleration due to gravity and α is the coefficient of thermal expansion. In writing Eq. (2.1), we made use of the Boussinesq approximation, which states that variations of the density are ignored in all terms in the equation of motion, except the external force term. The magnetic permeability μ_e , thermal diffusivity κ , and electrical resistivity η , are all assumed to be constant.

The initial state is one in which the velocity, density, pressure, and temperature at any point in the fluid are, respectively, given by

$$(2.7) \quad \mathbf{q} = (0, 0, 0), \quad \rho = \rho(z), \quad p = p(z), \quad T = T(z).$$

Let us assume small perturbations around the basic solution and let $\delta \rho$, δp , θ , $\mathbf{q}(u, v, w)$, and $\mathbf{h} = (h_x, h_y, h_z)$ denote respectively perturbations in the density ρ , pressure p , temperature T , velocity $\mathbf{q}(0, 0, 0)$, and magnetic field

$\mathbf{H} = (0, 0, H)$. The change in density $\delta\rho$, caused mainly by the perturbation θ in temperature, is given by

$$(2.8) \quad \rho + \delta\rho = \rho_0 [1 - \alpha(T + \theta - T_0)] = \rho - \alpha\rho_0\theta, \quad \text{i.e.} \quad \delta\rho = -\alpha\rho_0\theta.$$

Then the linearized perturbation equations are:

$$(2.9) \quad \frac{\partial \mathbf{q}}{\partial t} = -\frac{1}{\rho_0} \nabla \delta p - \mathbf{g} \alpha \theta + \left(\nu + \nu' \frac{\partial}{\partial t} \right) \nabla^2 \mathbf{q} + \frac{\mu_e}{4\pi\rho_0} (\nabla \times \mathbf{h}) \times \mathbf{H} + 2(\mathbf{q} \times \boldsymbol{\Omega}),$$

$$(2.10) \quad \nabla \cdot \mathbf{q} = 0,$$

$$(2.11) \quad \frac{\partial \theta}{\partial t} = \beta w + \kappa \nabla^2 \theta,$$

$$(2.12) \quad \nabla \cdot \mathbf{h} = 0,$$

$$(2.13) \quad \frac{\partial \mathbf{h}}{\partial t} = (\mathbf{H} \cdot \nabla) \mathbf{q} + \eta \nabla^2 \mathbf{h}.$$

Within the framework of Boussinesq's approximation, Eqs. (2.9)–(2.13), become

$$(2.14) \quad \frac{\partial}{\partial t} \nabla^2 w = \left(\nu + \nu' \frac{\partial}{\partial t} \right) \nabla^4 w + \frac{\mu_e H}{4\pi\rho_0} \nabla^2 \left(\frac{\partial h_z}{\partial z} \right) + g\alpha \left(\frac{\partial^2 \theta}{\partial x^2} + \frac{\partial^2 \theta}{\partial y^2} \right) - 2\Omega \frac{\partial \varsigma}{\partial z},$$

$$(2.15) \quad \frac{\partial \varsigma}{\partial t} = \left(\nu + \nu' \frac{\partial}{\partial t} \right) \nabla^2 \varsigma + 2\Omega \frac{\partial w}{\partial z} - \frac{\mu_e H}{4\pi\rho_0} \frac{\partial \xi}{\partial z},$$

$$(2.16) \quad \frac{\partial \theta}{\partial t} = \beta w + \kappa \nabla^2 \theta,$$

$$(2.17) \quad \frac{\partial h_z}{\partial t} = H \frac{\partial w}{\partial z} + \eta \nabla^2 h_z,$$

$$(2.18) \quad \frac{\partial \xi}{\partial t} = H \frac{\partial \varsigma}{\partial z} + \eta \nabla^2 \xi,$$

where $\nabla^2 = \frac{\partial^2}{\partial x^2} + \frac{\partial^2}{\partial y^2} + \frac{\partial^2}{\partial z^2}$; and $\varsigma = \frac{\partial v}{\partial x} - \frac{\partial u}{\partial y}$ and $\xi = \frac{\partial h_y}{\partial x} - \frac{\partial h_x}{\partial y}$ denote the z -component of vorticity and current density respectively.

3. NORMAL MODE OF ANALYSIS

Analyzing the disturbances in normal modes, we assume that the perturbation quantities are of the form

$$(3.1) \quad [w, \theta, h_z, \varsigma, \xi] = [W(z), \Theta(z), K(z), Z(z), X(z)] \exp(ik_x x + ik_y y + nt),$$

where k_x, k_y are the wave numbers along the x - and y -directions respectively, $k = (k_x^2 + k_y^2)^{1/2}$, is the resultant wave number and n is the growth rate, which in general is a complex constant.

Using (3.1), Eqs. (2.14)–(2.18), in non-dimensional form, transform to:

$$(3.2) \quad (D^2 - a^2) [(1 + F\sigma)(D^2 - a^2) - \sigma] W = Ra^2 \Theta + T_A DZ - Q(D^2 - a^2) DK,$$

$$(3.3) \quad [(1 + F\sigma)(D^2 - a^2) - \sigma] Z = -DW - QDX,$$

$$(3.4) \quad (D^2 - a^2 - p_1 \sigma) \Theta = -W,$$

$$(3.5) \quad (D^2 - a^2 - p_2 \sigma) K = -DW,$$

$$(3.6) \quad (D^2 - a^2 - p_2 \sigma) X = -DZ,$$

where we have introduced the new coordinates $(x', y', z') = (x/d, y/d, z/d)$ in units of length d , and $D = d/dz'$. For convenience, the primes are dropped hereafter. We have substituted, $a = kd$, $\sigma = \frac{nd^2}{\nu}$, and $p_1 = \frac{\nu}{\kappa}$ is the thermal Prandtl number, $p_2 = \frac{\nu}{\eta}$ is the magnetic Prandtl number, $F = \frac{\nu'}{d^2}$ is the Rivlin-Ericksen kinematic viscoelasticity parameter, $R = \frac{g\alpha\beta d^4}{\kappa\nu}$ is the thermal Rayleigh number, $Q = \frac{\mu_e H^2 d^2}{4\pi\rho_0\nu\eta}$ is the Chandrasekhar number, and $T_A = \frac{4\Omega^2 d^4}{\nu^2}$ is the Taylor number. Also, we have substituted $W = W_{\oplus}$, $\Theta = \frac{\beta d^2}{\kappa} \Theta_{\oplus}$, $Z = \frac{2\Omega d}{\nu} Z_{\oplus}$, $K = \frac{Hd}{\eta} K_{\oplus}$, $X = \left(\frac{Hd}{\eta}\right) \left(\frac{2\Omega d}{\nu}\right) X_{\oplus}$, and $D_{\oplus} = dD$, and dropped (\oplus) for convenience.

We now consider the case where both the boundaries are rigid and perfectly conducting and are maintained at constant temperature. Then, the perturbations in the temperature are zero on the boundaries. The appropriate boundary conditions, with respect to which Eqs. (3.2)–(3.6) must possess a solution, are:

$$(3.7) \quad \begin{aligned} W = DW = 0, \quad \Theta = 0, \quad Z = 0, \quad K = 0, \quad DX = 0, \\ \text{at } z = 0 \quad \text{and } z = 1. \end{aligned}$$

The Eqs. (3.2)–(3.6), along with appropriate boundary conditions (3.7), constitute an eigenvalue problem for σ and we want to characterize σ_i , when $\sigma_r \geq 0$.

We first note that, since W and Z satisfy $W(0) = 0 = W(1)$, then $K(0) = 0 = K(1)$ and $Z(0) = 0 = Z(1)$ in addition to satisfying the governing equations; and hence we have from the Rayleigh-Ritz inequality (SCHULTZ [18]):

$$\begin{aligned}
 & \int_0^1 |DW|^2 dz \geq \pi^2 \int_0^1 |W|^2 dz, \\
 (3.8) \quad & \int_0^1 |DK|^2 dz \geq \pi^2 \int_0^1 |K|^2 dz, \\
 & \int_0^1 |DZ|^2 dz \geq \pi^2 \int_0^1 |Z|^2 dz.
 \end{aligned}$$

Furthermore, for $W(0) = 0 = W(1)$, $K(0) = 0 = K(1)$, and $Z(0) = 0 = Z(1)$, BANERJEE *et al.* [19] have shown that

$$\begin{aligned}
 & \int_0^1 |D^2W|^2 dz \geq \pi^2 \int_0^1 |DW|^2 dz, \\
 (3.9) \quad & \int_0^1 |D^2K|^2 dz \geq \pi^2 \int_0^1 |DK|^2 dz, \\
 & \int_0^1 |D^2Z|^2 dz \geq \pi^2 \int_0^1 |DZ|^2 dz.
 \end{aligned}$$

4. MATHEMATICAL ANALYSIS

We prove the following lemma:

LEMMA 1: *For any arbitrary oscillatory perturbation, neutral or unstable*

$$\int_0^1 \left\{ |DK|^2 + a^2 |K|^2 \right\} dz \leq \frac{1}{\pi^2} \int_0^1 |DW|^2 dz.$$

P r o o f. Multiplying Eq. (3.5) by K^* (the complex conjugate of K) and integrating by parts each term of the resulting equation on the left-hand side

an appropriate number of times, and making use of boundary conditions on K , namely $K(0) = 0 = K(1)$, it follows that:

$$\begin{aligned}
 (4.1) \quad & \int_0^1 \left\{ |DK|^2 + a^2 |K|^2 \right\} dz + \sigma_r p_2 \int_0^1 |K|^2 dz \\
 & = \text{Real part of } \left\{ \int_0^1 K^* DW dz \right\} \leq \left| \int_0^1 K^* DW dz \right| \leq \int_0^1 |K^* DW| dz \\
 & \leq \int_0^1 |K^*| |DW| dz \leq \int_0^1 |K| |DW| dz \\
 & \leq \left\{ \int_0^1 |K|^2 dz \right\}^{1/2} \left\{ \int_0^1 |DW|^2 dz \right\}^{1/2}
 \end{aligned}$$

(utilizing the Cauchy-Schwartz inequality).

This gives that:

$$(4.2) \quad \int_0^1 |DK|^2 dz \leq \left\{ \int_0^1 |K|^2 dz \right\}^{1/2} \left\{ \int_0^1 |DW|^2 dz \right\}^{1/2}.$$

The inequality (4.1), on utilizing the inequalities (3.8) and (4.2), gives:

$$(4.3) \quad \left\{ \int_0^1 |K|^2 dz \right\}^{1/2} \leq \frac{1}{\pi^2} \left\{ \int_0^1 |DW|^2 dz \right\}^{1/2}.$$

Since $\sigma_r \geq 0$ and $p_2 > 0$, and hence inequality (4.1), on utilizing (4.3) gives:

$$(4.4) \quad \int_0^1 \left(|DK|^2 + a^2 |K|^2 \right) dz \leq \frac{1}{\pi^2} \int_0^1 |DW|^2 dz.$$

This completes the proof of Lemma 1.

LEMMA 2: *For any arbitrary oscillatory perturbation, neutral or unstable*

$$\begin{aligned}
 & \int_0^1 |Z|^2 dz \leq \frac{1}{\pi^4} \int_0^1 |DW|^2 dz, \\
 & \int_0^1 \left(|DZ|^2 + a^2 |Z|^2 \right) dz \leq \frac{1}{\pi^2} \int_0^1 |DW|^2 dz.
 \end{aligned}$$

P r o o f. Multiplying Eq. (3.3) by Z^* (the complex conjugate of Z) and integrating by parts each term of the resulting equation on the left-hand side an appropriate number of times, on utilizing Eq. (3.6) and the appropriate boundary conditions (3.7), it follows that:

$$\begin{aligned}
 (4.5) \quad & (1 + F\sigma_r) \int_0^1 \left\{ |DZ|^2 + a^2 |Z|^2 \right\} dz + \sigma_r \int_0^1 |Z|^2 dz \\
 & + Q \int_0^1 \left\{ |DX|^2 + a^2 |X|^2 \right\} dz + Qp_2\sigma_r \int_0^1 |X|^2 dz \\
 & = \text{Real part of } \left\{ \int_0^1 DW^* Z dz \right\} \leq \left| \int_0^1 DW^* Z dz \right| \\
 & \leq \int_0^1 |DW^* Z| dz \leq \int_0^1 |DW^*| |Z| dz \\
 & = \int_0^1 |DW| |Z| dz \leq \left\{ \int_0^1 |Z|^2 dz \right\}^{1/2} \left\{ \int_0^1 |DW|^2 dz \right\}^{1/2}
 \end{aligned}$$

(utilizing the Cauchy-Schwartz inequality).

This gives that

$$(4.6) \quad \int_0^1 |DZ|^2 dz \leq \left\{ \int_0^1 |Z|^2 dz \right\}^{1/2} \left\{ \int_0^1 |DW|^2 dz \right\}^{1/2} .$$

Inequality (4.5) on utilizing inequalities (3.8) and (4.6), gives

$$(4.7) \quad \left\{ \int_0^1 |Z|^2 dz \right\}^{1/2} \leq \frac{1}{\pi^2} \left\{ \int_0^1 |DW|^2 dz \right\}^{1/2} .$$

Since $\sigma_r \geq 0$ and $p_2 > 0$, hence inequality (4.5) on utilizing (4.7), give

$$\begin{aligned}
 (4.8) \quad & \int_0^1 |Z|^2 dz \leq \frac{1}{\pi^4} \int_0^1 |DW|^2 dz, \\
 & \int_0^1 \left(|DZ|^2 + a^2 |Z|^2 \right) dz \leq \frac{1}{\pi^2} \int_0^1 |DW|^2 dz.
 \end{aligned}$$

This completes the proof of Lemma 2.

We now prove the following theorems:

THEOREM 1: *If $R > 0$, $F > 0$, $Q > 0$, $T_A > 0$, $p_1 > 0$, $p_2 > 0$, $\sigma_r \geq 0$, and $\sigma_i \neq 0$, then the necessary condition for the existence of a non-trivial solution (W, Θ, K, Z, X) of Eqs. (3.2)–(3.6), together with boundary conditions (3.7), is that*

$$\frac{T_A F}{\pi^2} + \frac{T_A}{\pi^4} + \frac{Q p_2}{\pi^2} > 1.$$

P r o o f. Multiplying Eq. (3.2) by W^* (the complex conjugate of W) throughout and integrating the resulting equation over the vertical range of z , we get

$$\begin{aligned} (4.9) \quad & (1 + F\sigma) \int_0^1 W^*(D^2 - a^2)^2 W \, dz - \sigma \int_0^1 W^*(D^2 - a^2) W \, dz \\ & = R a^2 \int_0^1 W^* \Theta \, dz + T_A \int_0^1 W^* D Z \, dz - Q \int_0^1 W^* D (D^2 - a^2) K \, dz. \end{aligned}$$

Taking the complex conjugate of both sides of Eq. (3.4), we get:

$$(4.10) \quad (D^2 - a^2 - p_1 \sigma^*) \Theta^* = -W^*.$$

Therefore, using (4.10), we get:

$$(4.11) \quad \int_0^1 W^* \Theta \, dz = - \int_0^1 \Theta (D^2 - a^2 - p_1 \sigma^*) \Theta^* \, dz.$$

Taking the complex conjugate of both sides of Eq. (3.3), we get:

$$(4.12) \quad (1 + F\sigma^*)(D^2 - a^2)Z^* - \sigma^* Z^* = -DW^* - QDX^*.$$

Therefore, using (4.12), we get:

$$\begin{aligned} (4.13) \quad & \int_0^1 W^* D Z \, dz = - \int_0^1 D W^* Z \, dz = (1 + F\sigma^*) \int_0^1 Z^* (D^2 - a^2) Z \, dz \\ & \quad - \sigma^* \int_0^1 Z^* Z \, dz + Q \int_0^1 Z D X^* \, dz. \end{aligned}$$

Now, integrating by parts, the third term on left-hand side and using Eq. (3.6) and the appropriate boundary condition (3.7), we get:

$$(4.14) \quad \int_0^1 W^* DZ dz = (1 + F\sigma^*) \int_0^1 Z^* (D^2 - a^2) Z dz - \sigma^* \int_0^1 Z^* Z dz + Q \int_0^1 X (D^2 - a^2 - p_2\sigma) X^* dz.$$

Taking the complex conjugate of both sides of Eq. (3.5), we get:

$$(4.15) \quad [D^2 - a^2 - p_2\sigma^*] K^* = -DW^*.$$

Therefore, Eq. (4.15) with the appropriate boundary condition (3.7), we get:

$$(4.16) \quad \int_0^1 W^* D(D^2 - a^2) K dz = - \int_0^1 DW^* (D^2 - a^2) K dz = \int_0^1 K (D^2 - a^2) (D^2 - a^2 - p_2\sigma^*) K^* dz.$$

Substituting (4.11), (4.14), and (4.16) into the right-hand side of Eq. (4.9), we get:

$$(4.17) \quad (1 + F\sigma) \int_0^1 W^* (D^2 - a^2)^2 W dz - \sigma \int_0^1 W^* (D^2 - a^2) W dz = -Ra^2 \int_0^1 \Theta (D^2 - a^2 - p_1\sigma^*) \Theta^* dz + T_A (1 + F\sigma^*) \int_0^1 Z (D^2 - a^2) Z^* dz - T_A \sigma^* \int_0^1 Z^* Z dz + T_A Q \int_0^1 X (D^2 - a^2 - p_2\sigma^*) X^* dz - Q \int_0^1 K^* (D^2 - a^2)^2 K dz - Q p_2 \sigma^* \int_0^1 K^* (D^2 - a^2) K dz.$$

Integrating the terms on both sides of Eq. (4.17) an appropriate number of times and making use of the appropriate boundary conditions (3.7), we get:

$$\begin{aligned}
(4.18) \quad & (1 + F\sigma) \int_0^1 \left\{ |D^2W|^2 + 2a^2 |DW|^2 + a^4 |W|^2 \right\} dz \\
& + \sigma \int_0^1 \left(|DW|^2 + a^2 |W|^2 \right) dz = Ra^2 \int_0^1 \left(|D\Theta|^2 + a^2 |\Theta|^2 \right) dz \\
& + Ra^2 p_1 \sigma^* \int_0^1 |\Theta|^2 dz - T_A(1 + F\sigma^*) \int_0^1 \left\{ |DZ|^2 + a^2 |Z|^2 \right\} dz \\
& - T_A \sigma^* \int_0^1 |Z|^2 dz - T_A Q \int_0^1 \left(|DX|^2 + a^2 |X|^2 \right) dz \\
& - T_A Q p_2 \sigma \int_0^1 |X|^2 dz - Q \int_0^1 \left(|D^2K|^2 + 2a^2 |DK|^2 + a^4 |K|^2 \right) dz \\
& - Q p_2 \sigma^* \int_0^1 \left(|DK|^2 + a^2 |K|^2 \right) dz.
\end{aligned}$$

Now, equating the imaginary parts on both sides of Eq. (4.18), and cancelling $\sigma_i (\neq 0)$ throughout from the imaginary part, we get:

$$\begin{aligned}
(4.19) \quad & F \int_0^1 \left\{ |D^2W|^2 + 2a^2 |DW|^2 + a^4 |W|^2 \right\} dz + \int_0^1 \left\{ |DW|^2 + a^2 |W|^2 \right\} dz \\
& = -Ra^2 p_1 \int_0^1 |\Theta|^2 dz + T_A F \int_0^1 \left\{ |DZ|^2 + a^2 |Z|^2 \right\} dz \\
& + T_A \int_0^1 |Z|^2 dz - T_A Q p_2 \int_0^1 |X|^2 dz + Q p_2 \int_0^1 \left\{ |DK|^2 + a^2 |K|^2 \right\} dz.
\end{aligned}$$

Now, for $R > 0$, $p_2 > 0$, $p_1 > 0$, $Q > 0$, and $T_A > 0$, and utilizing the inequalities (3.8), (3.9), (4.4), and (4.8), Eq. (4.19) gives,

$$(4.20) \quad \left[1 - \left(\frac{T_A F}{\pi^2} + \frac{T_A}{\pi^4} + \frac{Q p_2}{\pi^2} \right) \right] \int_0^1 |DW|^2 dz + I_1 < 0,$$

where

$$(4.21) \quad I_1 = F \int_0^1 \left\{ |D^2W|^2 + 2a^2 |DW|^2 + a^4 |W|^2 \right\} dz \\ + a^2 \int_0^1 |W|^2 dz + Ra^2 p_1 \int_0^1 |\Theta|^2 dz + T_A Q p_2 \int_0^1 |X|^2 dz,$$

is positive definite, and therefore, we must have that

$$(4.22) \quad \frac{T_A F}{\pi^2} + \frac{T_A}{\pi^4} + \frac{Q p_2}{\pi^2} > 1.$$

Hence, if

$$(4.23) \quad \sigma_r \geq 0 \quad \text{and} \quad \sigma_i \neq 0, \quad \text{then} \quad \frac{T_A F}{\pi^2} + \frac{T_A}{\pi^4} + \frac{Q p_2}{\pi^2} > 1.$$

That completes the proof of Theorem 1.

Presented otherwise, from the point of view of the existence of instability as a stationary convection, the above theorem can be put in the form as follows:

THEOREM 2: *The sufficient condition for the onset of instability as a non-oscillatory motions of non-growing amplitude in a Rivlin-Ericksen fluid heated from below, in the presence of uniform vertical magnetic field and rotation, is that, $\frac{T_A F}{\pi^2} + \frac{T_A}{\pi^4} + \frac{Q p_2}{\pi^2} \leq 1$, where T_A is the Taylor number, Q is the Chandrasekhar number, p_2 is the magnetic Prandtl number, and F is the viscoelasticity parameter when both the boundaries are rigid.*

OR:

The onset of instability in a Rivlin-Ericksen fluid heated from below in the presence of an uniform vertical magnetic field and rotation, cannot manifest itself as oscillatory motion of growing amplitude if the Taylor number T_A , the Chandrasekhar number Q , p_2 the magnetic Prandtl number, and the viscoelasticity parameter F , satisfy the inequality $\frac{T_A F}{\pi^2} + \frac{T_A}{\pi^4} + \frac{Q p_2}{\pi^2} \leq 1$ when both the bounding surfaces are rigid.

The sufficient condition for the validity of the PES can be expressed in the form:

THEOREM 3: *If $(W, \Theta, K, Z, X, \sigma)$, $\sigma = \sigma_r + i\sigma_i$, $\sigma_r \geq 0$ is a solution of Eqs. (2.15)–(3.1), with $R > 0$ and*

$$\frac{T_A F}{\pi^2} + \frac{T_A}{\pi^4} + \frac{Q p_2}{\pi^2} \leq 1,$$

then $\sigma_i = 0$. In particular, a sufficient condition for the validity of the ‘exchange principle’, i.e. $\sigma_r = 0 \Rightarrow \sigma_i = 0$, is that $\frac{T_A F}{\pi^2} + \frac{T_A}{\pi^4} + \frac{Q p_2}{\pi^2} \leq 1$.

In the context of the existence of instability in ‘oscillatory modes’ and of ‘over-stability’ in the present configuration, we can state the above theorem as follows:

THEOREM 4: *The necessary condition for the existence of instability in ‘oscillatory modes’ and that of ‘overstability’ in a Rivlin-Ericksen fluid heated from below in the presence of uniform vertical magnetic field and rotation, is that the Taylor number T_A , the Chandrasekhar number Q , p_2 the magnetic Prandtl number, and the viscoelasticity parameter F must satisfy the inequality $\frac{T_A F}{\pi^2} + \frac{T_A}{\pi^4} + \frac{Q p_2}{\pi^2} > 1$, when both the bounding surfaces are rigid.*

SPECIAL CASES: It follows from Theorem 1 that an arbitrary neutral or unstable mode is non-oscillatory in character and PES is valid for:

1. Thermal convection in a Rivlin-Ericksen fluid heated from below, i.e. when $Q = 0 = T_A$ (KUMAR *et al.* [12]).
2. Magneto-thermal convection in a Rivlin-Ericksen fluid heated from below ($T_A = 0$), if $\left(\frac{Q p_2}{\pi^2}\right) \leq 1$ (GUPTA *et al.* [16]).
3. Rotatory-thermal convection in a Rivlin-Ericksen fluid heated from below ($Q = 0$), if $\frac{T_A F}{\pi^2} + \frac{T_A}{\pi^4} \leq 1$.
4. When $F = 0$ we retrieve the result for a Newtonian fluid by GUPTA *et al.* [16] in the presence of a uniform vertical magnetic field and rotation; i.e., $\frac{T_A}{\pi^4} + \frac{Q p_2}{\pi^2} \leq 1$.

5. CONCLUSIONS

This theorem mathematically establishes that the onset of instability in a Rivlin-Ericksen fluid in the presence of uniform vertical magnetic field and rotation cannot manifest itself as oscillatory motion of growing amplitude if the Taylor number T_A , the Chandrasekhar number Q , p_2 the magnetic Prandtl number, and the viscoelasticity parameter F , satisfy the inequality $\frac{T_A F}{\pi^2} + \frac{T_A}{\pi^4} + \frac{Q p_2}{\pi^2} \leq 1$ when both the bounding surfaces are rigid.

The essential content of the theorem from the point of view of linear stability theory, is that for the configuration of coupled-stress fluid of infinite horizontal extension heated from below having rigid boundaries at the top and bottom of the fluid and in the presence of an uniform vertical magnetic field and rotation parallel to the force field of gravity, an arbitrary neutral or unstable modes of the system are definitely non-oscillatory in character if $\frac{T_A F}{\pi^2} + \frac{T_A}{\pi^4} + \frac{Q p_2}{\pi^2} \leq 1$, and in particular, if the PES is valid.

ACKNOWLEDGMENT

The author is highly thankful to the referees for their very constructive and valuable suggestions and useful technical comments which led to a significant improvement of this paper.

REFERENCES

1. BÉNARD H., *Les tourbillions cellulaires dans une nappe liquid*, Revue Générale des Sciences Pures et Appliquées, **11**, 1261–1271, 1309–1328, 1900.
2. RAYLEIGH L., *On convective currents in a horizontal layer of fluid when the higher temperature is on the underside*, Philosophical Magazine, **32**, 529–546, 1916.
3. JEFFREYS H., *The stability of a fluid layer heated from below*, Philosophical Magazine, **2**, 833–844, 1926.
4. CHANDRASEKHAR S., *Hydrodynamic and Hydromagnetic Stability*, Dover Publication, New York, 1981.
5. BHATIA P.K., STEINER J.M., *Convective instability in a rotating viscoelastic fluid layer*, Zeitschrift fur Angewandte Mathematik and Mechanik, **52**, 321–327, 1972.
6. BHATIA P.K., STEINER J.M., *Thermal Instability in a viscoelastic fluid layer in hydromagnetics*, Journal of Mathematical Analysis and Applications, **41**, 2, 271–283, 1973.
7. SHARMA R.C., *Thermal instability in a viscoelastic fluid in hydromagnetics*, Acta Physica Hungarica, **38**, 293–298, 1975.
8. SHARMA R.C., *Effect of rotation on thermal instability of a viscoelastic fluid*, Acta Physica Hungarica, **40**, 11–17, 1976.
9. OLDROYD J.G., *Non-Newtonian effects in steady motion of some idealized elastic-viscous liquids*, Proceedings of the Royal Society of London, **A245**, 278–297, 1958.
10. RIVLIN R.S., ERICKSEN J.L., *Stress deformation relations for isotropic materials*, J. Rat. Mech. Anal., **4**, 323, 1955.
11. SHARMA R.C., KUMAR P., *Effect of rotation on thermal instability in Rivlin-Ericksen elastic-viscous fluid*, Zeitschrift fur Naturforschung, **51a**, 821–824, 1996.
12. KUMAR P., MOHAN H., LAL R., *Effect of magnetic field on thermal instability of a rotating Rivlin-Ericksen viscoelastic fluid*, Int. J. of Maths. Math. Scs., **2006**, 1–10.
13. PELLOW A., SOUTHWELL R.V., *On the maintained convective motion in a fluid heated from below*, Proc. Roy. Soc. London A, **176**, 312–43, 1940.
14. BANERJEE M.B., KATOCH D.C., DUBE G.S., BANERJEE K., *Bounds for growth rate of perturbation in thermohaline convection*, Proc. R. Soc. A, **378**, 301–304, 1981.
15. BANERJEE M.B., BANERJEE B., *A characterization of non-oscillatory motions in magneto-hydrodynamics*, Ind. J. Pure & Appl Maths., **15**, 4, 377–382, 1984.
16. GUPTA J.R., SOOD S.K., BHARDWAJ U.D., *On the characterization of nonoscillatory motions in rotatory hydromagnetic thermohaline convection*, Indian J. Pure Appl. Math., **17**, 1, 100–107, 1986.

17. BANYAL A.S, *The necessary condition for the onset of stationary convection in couple-stress fluid*, Int. J. of Fluid Mech. Research, **38**, 5, 450–457, 2011.
18. SCHULTZ M.H., *Spline Analysis*, Prentice Hall, Englewood Cliffs, New Jersey, 1973.
19. BANERJEE M.B., GUPTA J.R., PRAKASH J., *On thermohaline convection of Veronis type*, J. Math. Anal. Appl., **179**, 327–334, 1992.

Received June 24, 2012; revised version September 12, 2012.

From the Editorial Board

Our Reviewers

The Editorial Committee wishes to express many thanks and appreciation to all the referees, listed below, for their valuable opinions concerning papers submitted to the Engineering Transactions in 2012:

A. Glema	J. P. Okrajni
J. Janiszewski	P. Perzyna
T. Jankowiak	H. Petryk
L. Jarecki	R. Pęcherski
B. Kaźmierczak	K. Pietrzak
K. Kowalczyk–Gajewska	J. Rojek
Z. L. Kowalewski	A. Rusinek
A. A. Kwiecień	W. Sumelka
T. Lekszycki	T. Szolc
W. Moćko	A. Winnicki
Z. Nowak	S. Wolny

Received reviews for articles published in 2012 year.

DIRECTIONS FOR THE AUTHORS

The periodical *ENGINEERING TRANSACTIONS (ROZPRAWY INŻYNIERSKIE)* presents original papers which should not be published elsewhere.

As a rule, the volume of a paper should not exceed 40 000 typographic signs. The following directions are particularly important:

1. **The paper submitted for publication should be written in English.**
2. The title of the paper should be as short as possible. The text should be preceded by a brief introduction; it is also desirable that a list of notations used in the paper should be given.
3. Short papers should be divided into section and subsection, long papers into sections, subsections and points. Each section, subsection or point must bear a title.
4. The formula number consists of two figures: the first represents the section number and the other the formula number in that section. Thus the division into subsections does not influence the numbering of formulae. Only such formulae should be numbered to which the author refers throughout the paper. This also applies to the resulting formulae. The formula number should be written on the left-hand side of the formula; round brackets are necessary to avoid any misunderstanding. For instance, if the author refers to the third formula of the set (2.1), a subscript should be added to denote the formula, viz. (2.1)₃.
5. All the notations should be written very distinctly. Special care must be taken to distinguish between small and capital letters as precisely as possible. Semi-bold type must be underlined in black pencil. Explanations should be given on the margin of the manuscript in case of special type face.
6. Vectors are to be denoted by semi-bold type, transforms of the corresponding functions by tildes symbols. Trigonometric functions are denoted by sin, cos, tan and cot, inverse functions – by arc sin, arc cos, arc tan and arc cot; hyperbolic functions are denoted by sh, ch, th and cth, inverse functions – by Arsh, Arch, Arth and Arcth.
7. The figures in square brackets denote reference titles. Items appearing in the reference list should include the initials of the first name of the author and his surname, also the full of the paper (in the language of the original paper); moreover:
 - a) In the case of books, the publisher's name, the place and year of publication should be given, e.g., 5. ZIEMBA S., *Vibration analysis*, PWN, Warszawa 1970;
 - b) In the case of a periodical, the full title of the periodical, consecutive volume number, current issue number, pp. from ... to ..., year of publication should be mentioned; the annual volume number must be marked in semi-bold type as to distinguish it from the current issue number, e.g., 6. SOKOŁOWSKI M., *A thermoelastic problem for a strip with discontinuous boundary conditions*, Arch. Mech., **13**, 3, 337–354, 1961.
8. The authors should enclose a summary of the paper. The volume of the summary is to be about 100 words, also key words are requested.
9. The preferable format for the source file is TeX or LaTeX while MS Word is also acceptable. Separate files for the figures should be provided in one of the following formats: EPS or PostScript (preferable), PDF, TIFF, JPEG, BMP, of at least 300 DPI resolution. The figures should be in principle in gray-scale and only if necessary the color will be accepted.

Upon receipt of the paper, the Editorial Office forwards it to the reviewer. His opinion is the basis for the Editorial Committee to determine whether the paper can be accepted for publication or not.

Once the paper is printed, the issue of Engineering Transactions free of charge is sent to the author. Also the PDF file of the paper is forwarded by the e-mail to the authors.

Editorial Committee
ENGINEERING TRANSACTIONS